

The High Temperature Oxidation of Refractory Metals and Carbides in Molecular and Atomic Oxygen

A Dissertation

Presented to

The Faculty of the School of Engineering and Applied Sciences at
The University of Virginia

In partial fulfilment of the requirements for the degree of
Doctor of Philosophy

By Connor Stephens

March 31, 2025

APPROVAL SHEET

This
Dissertation
is submitted in partial fulfillment of the requirements
for the degree of
Doctor of Philosophy

Author: Connor Stephens

This Dissertation has been read and approved by the examining committee:

Advisor: Elizabeth Opila

Advisor:

Committee Member: Jon Ihlefeld

Committee Member: Prasanna Balachandran

Committee Member: Chloe Dedic

Committee Member: Lavina Backman

Committee Member:

Committee Member:

Accepted for the School of Engineering and Applied Science:



Jennifer L. West, School of Engineering and Applied Science

May 2025

Abstract

Leading-edge components on hypersonic vehicles, such as nose caps and wing tips, will experience temperatures greater than 2000°C in highly oxidizing environments. Additionally, shockwaves and high temperatures created during high Mach flight cause molecular oxygen to dissociate into atomic oxygen (AO). Component materials must be able to withstand these extremely oxidizing conditions while also maintaining their mechanical properties. State-of-the-art thermal protection systems are often Si-based due to the excellent protective capabilities of SiO₂ scales against high temperature oxidation. However, these material systems are limited to temperatures less than ~1723°C because of active oxidation to form SiO(g) and SiO₂ melting. Therefore, new materials systems are needed that are oxidation resistant and stable at higher temperatures than Si-based materials.

The transition metals, M, and metal carbides, MC (M = Zr, Hf, Ta) form oxides which have melting points greater than 1723°C. The carbides are considered candidate materials for leading-edge hypersonic components because they have high melting temperatures (>3000°C). However, they are often expensive and challenging to manufacture. The metals, on the other hand, are much more cost-effective and simpler to manufacture, but have significantly lower melting temperatures. Both the metals and carbides have poor oxidation resistance at high temperatures and the mechanisms which drive oxidation are not well understood. Despite the significant body of work regarding the oxidation of these materials, the role of carbon in the oxidation process has not been well documented. It is generally believed that carbides oxidize more rapidly than metals because the CO(g) generated during oxidation creates a porous oxide network which allows rapid oxygen ingress to the underlying material. However, there have been no direct comparisons between the

oxidation behavior of the metals and carbides in identical experimental conditions which would isolate the role of carbon on the oxidation kinetics and mechanisms.

Additionally, the presence of AO in a high temperature oxidizing environment could significantly affect oxidation rates by lowering the energy barrier required for oxygen to react with materials. However, few studies have been conducted which focus on the effects of AO on oxidation. Primarily, this is due to the prohibitively expensive operating costs of the facilities traditionally used to generate AO in high temperatures, such as arc-jets and plasmatrone, which can cost upwards of \$150K/day. These technologies also do not allow for the separation of AO effects from high temperature, pressure, or flow velocity. A new technique is needed to isolate the effects of AO on oxidation at high temperatures.

This work has three primary objectives: 1) conduct identical oxidation experiments of transition metals, M, and metal carbides, MC (M = Zr, Hf, Ta), which isolate the effects of carbon on oxidation and allow for kinetic and mechanistic comparisons to be drawn; 2) construct a new resistive heating system for ultra-high temperature oxidation experiments that is equipped with a DC microplasma for generating AO which can be used to isolate AO's effects on oxidation; and 3) conduct oxidation experiments of the same materials in Objective 1 in ordinary molecular oxygen and in AO-containing environments to determine the effects, if any, of AO on oxidation kinetics and mechanisms.

In Objective 1, it was observed that the transition metals investigated all undergo breakaway oxidation caused by cracking in the grown oxides. This breakaway transition from a solid-state diffusion-limited oxidation mechanism to a gas-phase diffusion mechanism leads to a much higher oxidation rate post-breakaway. In general, the carbides form a porous oxide and do not experience breakaway oxidation. Despite the porous oxide, the recession rate of the carbides

is slower than the post-breakaway recession rate of the metals; therefore, the carbides are the preferred material for longer-term oxidation resistance. The effects of carbon on the oxidation mechanism are determined to be: 1) reduction in oxygen solubility in the underlying material, 2) CO(g) formation creates a porous oxide, driving gas-phase diffusion but preventing significant cracking in the oxide, and 3) increasing the melting point and stiffness of the underlying material.

In Objective 2, a microplasma resistive heating system (MRHS) was constructed capable of dissociating oxygen with up to 40% efficiency and reaching sample temperatures up to 2400°C. In Objective 3, this new MRHS was used to evaluate the oxidation of the same transition metals and carbides from Objective 1. It was found that atomic oxygen drives more rapid oxidation when oxygen transport is governed by gas-phase diffusion. Oxidation rates are unchanged in situations where solid-state diffusion is the rate-limiting mechanism. Additionally, the increased reactivity of atomic oxygen can affect the microstructure and morphology of the grown oxides by changing layer thicknesses, enhancing grain boundary oxidation, and embrittling the underlying material.

Acknowledgements

This work is the culmination of efforts from many, many more people than just myself, all of whom I am sincerely grateful for. Firstly, this would not have been possible without the guidance of my advisor, Dr. Elizabeth Opila. Thank you for your patience and support, believing in my abilities when I did not, and for giving me the opportunity to share our findings around the globe.

This work would similarly not have been possible without the funding support from the Air Force Office of Scientific Research (AFOSR grant no. FA9550-21-1-0102) and the AFOSR Defense University Research Instrumentation Program (DURIP grant no. FA9550-21-1-0274). Additional funding was provided by the Virginia Space Grant Consortium (VSGC) Graduate Student Fellowship Program.

I would also like to thank all of the people who generously contributed time and resources to this project: Dr. Mike Gordon at the University of California, Santa Barbara, provided invaluable discussion and direction on microplasma construction; Dr. Chloe Dedic and Ryan Thompson provided generous support and guidance regarding microplasma characterization; Steve DiPietro and Exothermics, Inc. generously provided the refractory metals used in this study; Dr. Elaine Zhou at North Carolina State University provided the fantastic time-of-flight secondary ion mass spectroscopy (TOF-SIMS) data; Stefan Steigerwald and Alex Dmitriev at The Pyrometer Co. provided a great deal of insight and information into temperature measurement aspects of this work; Dr. Lavina Backman provided excellent groundwork and advice for oxidation experiments using the resistive heating system; Dr. Helge Heinrich with the University of Virginia (UVA) Nanoscale Materials Characterization Facility (NMCF) provided support conducting focused ion beam (FIB) lift outs, transmission electron microscopy (TEM), and selected area electron

diffraction (SAED) characterization; Tanner Fitzgerald provided all of the machining work for many of the components of the microplasma resistive heating system (MRHS). This work is built on the contributions from all of you and I am sincerely grateful.

Additional thanks to: Jerry Weaver, Peter Chege, Ig Jakovac, Sherri Sullivan, Tonya Reynolds, Jamia Nixon, and Bryana Amador for helping with all the logistical sides of research; Shannon Donaldson for helping me think through and troubleshoot every aspect of the MRHS construction and characterization; Michael Richwine, Alex Uy, Christopher Recuperero, and Spence Hartman for your hard work and enthusiasm for learning; Dr. Mackenzie Ridley and Dr. Kaitlyn Detwiler, for helping me find my footing when starting my Ph.D. during the COVID-19 pandemic; and the entire Opila research group at UVA, each member of which has provided some support this project, big or small.

Finally, I want to thank my friends, my family, and my wife, Megan. Thank you for the relentless encouragement, sacrifice, and love you have given me over the last five years. More than anything, you have inspired me to run this race to completion in the face of many challenges and obstacles. I will never be able to express the gratitude I have for each one of you. This achievement is as much yours as it is mine.

Table of Contents

Introduction.....	1
Material Selection.....	4
Review of the Literature.....	8
a. Oxidation of Zr and ZrC.....	8
b. Oxidation of Hf and HfC.....	11
c. Oxidation of Ta and TaC.....	15
Part 1: The Role of Carbon in the High Temperature Oxidation of Transition Metals and Carbides.....	19
a. Oxidation Method.....	19
b. Oxidation of Ta vs TaC.....	22
i. Experimental Method.....	22
ii. Results.....	24
iii. Discussion.....	32
iv. Conclusions.....	37
c. Oxidation of Zr vs ZrC.....	39
i. Experimental Method.....	39
ii. Results.....	39
iii. Discussion.....	49
iv. Conclusions.....	57
d. Oxidation of Hf vs HfC.....	59
i. Experimental Method.....	59
ii. Results.....	59
iii. Discussion.....	65
iv. Conclusions.....	70
e. Part 1 Conclusions.....	70
f. Future Work.....	73
Part 2: Construction of a Novel Microplasma Resistive Heating System.....	75
a. Background.....	75
b. Construction Outline.....	77
c. Results.....	79
i. Construction of the RHS.....	79
ii. Oxidation Validation.....	80
iii. Oxygen Dissociation Confirmation and Quantification.....	81
d. Part 2 Conclusions.....	83

e.	Future Work	83
Part 3:	The Effects of Atomic Oxygen on the High Temperature Oxidation of Transition Metals and Carbides	85
a.	Background	85
b.	Experimental Methods	88
c.	Oxidation of Ta in MO Only and MO+AO.....	89
i.	Results.....	89
ii.	Discussion.....	92
d.	Oxidation of TaC in MO Only and MO+AO.....	93
i.	Results.....	93
ii.	Discussion.....	96
e.	Oxidation of Zr in MO Only and MO+AO.....	97
i.	Results.....	97
ii.	Discussion.....	100
f.	Oxidation of ZrC in MO Only and MO+AO	104
i.	Results.....	104
ii.	Discussion.....	106
g.	Oxidation of Hf in MO Only and MO+AO	110
i.	Results.....	110
ii.	Discussion.....	112
h.	Oxidation of HfC in MO Only and MO+AO.....	114
i.	Results.....	114
ii.	Discussion.....	116
i.	Part 3 Conclusions	119
j.	Future Work	120
Overall Impact		122
Status of Publications.....		124
Appendix A: Additional Micrographs.....		125
Appendix B: Ti and TiC.....		147
Appendix C: Unsuccessful Experiments		151
Bibliography		152

Introduction

Ultra-high temperature ceramics (UHTCs) are a class of materials which have extraordinarily high melting points ($T_M > 3000^\circ\text{C}$) and are being developed for use in wide variety of extreme applications requiring high temperature stability, including hypersonic leading edges [1], [2], [3]. Early transition metal carbides MC (where M belongs to group IV, V, or VI) are examples of such UHTCs. In addition to their exceptional melting points, the unique mixture of covalent, ionic, and metallic bonding also gives these materials a high hot hardness, strength, and thermal and electrical conductivity [4], [5]. However, these extreme properties make transition metal carbides very challenging to manufacture and can significantly increase the cost of production [6]. The corresponding refractory metals, on the other hand, are often easier to source and manufacture, though at the expense of losing the elite refractory properties possessed by their ceramic counterparts.

Despite high melting temperatures, poor oxidation resistance in high temperature environments is common to both the early transition metals and transition metal carbides [3]. Degradation proceeds extremely rapidly due to the non-protective nature of the oxides grown on these materials. Current state-of-the-art silicon-based materials form extremely protective oxides which set the standard for oxidation-resistant materials design. These materials, however, have limited maximum use-temperatures set by the melting point of the oxide ($T_M \sim 1723^\circ\text{C}$) [7]. Additionally, the materials begin to actively oxidize as $\text{SiO}(\text{g})$ at temperatures above $\sim 1600^\circ\text{C}$ and low oxygen partial pressure (P_{O_2}), resulting in a loss in oxidation protection [8]. Thus, the need to identify materials which have acceptable oxidation resistance and to understand their oxidation mechanisms has grown alongside the need to increase material melting point.

A significant amount of literature exists investigating the oxidation of the early transition metals and metal carbides below 1400°C [9], [10], [11], [12], [13], [14], [15], [16], [17], [18], [19], [20], [21], [22], [23], [24], [25], [26], [27], [28]; however, the mechanisms which govern their oxidation at ultra-high temperatures are still largely unexplored. In addition, to the best of the author's knowledge, there is no literature which provides a direct comparison of the refractory metals to the carbides that isolate the role of carbon on the oxidation mechanisms and kinetics. As such, details about the differences in microstructural effects, transport mechanisms, and oxidation kinetics for the metals and carbides are still unknown.

The transition metal carbides have been widely considered as candidate materials for hypersonic components, such as wing leading edges and nose cones, due to their high melting points and retention of mechanical properties at high temperatures [2]. However, in hypersonic flight environments (speeds of Mach 5 or greater), shockwaves coupled with high temperatures lead to the dissociation of oxygen in proximity to these leading-edge components [29]. It has been demonstrated in prior literature that oxidation of Mo and W [30] and carbon [31] via atomic oxygen

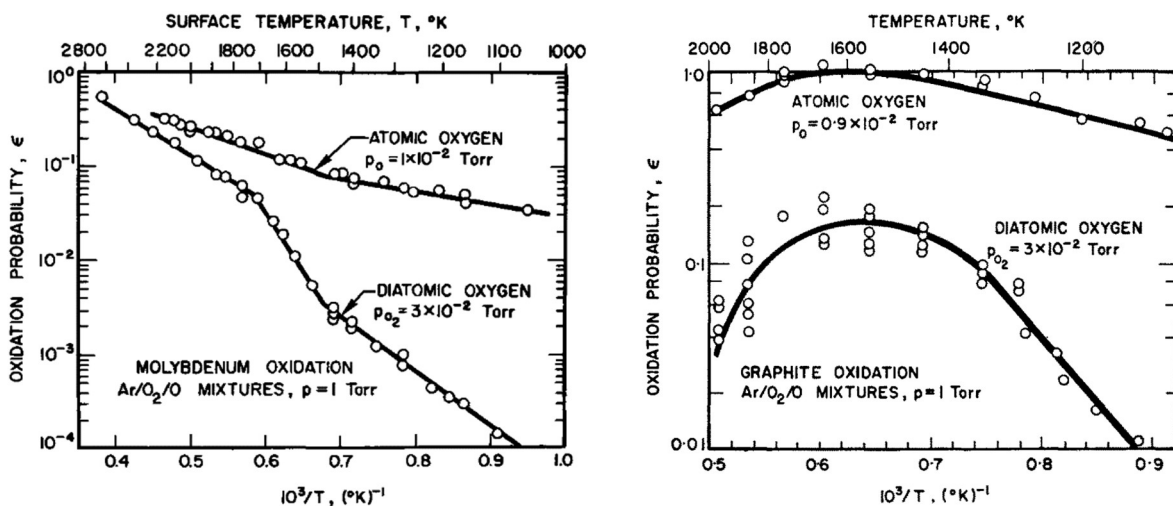


Figure 1.1: The oxidation probability for (left) Mo and (right) graphite in molecular and atomic oxygen. Graphics reproduced from [30] and [31].

(AO) occurs at a faster rate than in molecular oxygen (MO), shown in Figure 1.1. This lower rate is attributed to a lower energy barrier to oxidation as there is no longer a need to break the oxygen bond. Additional effects of AO have also been demonstrated, such as suppression of the passive/active transition temperature to form SiO(g) in SiC [32]. The recombination of AO on the surface of a material has also been shown to contribute non-negligible thermal energy to the surface which may affect the oxidation process [33], [34], [35], [36].

The following knowledge gaps have been identified for understanding oxidation mechanisms of refractory metals and carbides: 1) few studies have been conducted to compare the oxidation of any materials in MO and AO; 2) the oxidation kinetics and mechanisms of the early transition metals and metal carbides in high AO partial pressure environments have not been studied at all; and 3) The effects of AO recombination, i.e., catalycity and heat transfer efficiency to the material, on refractory metals and carbides are also unknown. Finally, most facilities capable of generated AO are either prohibitively expensive (arcjets or plasmatoms) or suffer from high AO recombination at chamber walls (microwave discharge furnaces) [37], preventing basic studies addressing these knowledge gaps.

The aim of this work is to address the knowledge gaps which exist in the understanding of the oxidation mechanisms of transition metals and metal carbides at ultra-high temperatures in hypersonic-like environments. The objectives of the planned work are: 1) explore the oxidation of early transition metals and their carbides in identical experimental conditions to elucidate the role of carbon on the oxidation process; 2) construct a new, cost-effective experimental system for high temperature oxidation which will enable the comparison of molecular oxygen and atomic oxygen environments; and 3) investigate the differences in oxidation mechanisms and kinetics of the transition metals and carbides in molecular oxygen and atomic oxygen environments.

Materials Selection

The materials of interest for this study were selected to exceed the current limitations of silicon-based materials and form oxides which have melting points greater than that of SiO_2 ($T_M \sim 1723^\circ\text{C}$). Table 2.1 lists the melting points of the group IV, V, and VI metals, carbides, and oxides and highlights in blue the materials which meet this criterion. Si-based materials, highlighted in orange, are listed for reference. Zr, Hf, and Ta, along with their carbides, are chosen for this work because of these melting points. Ti and TiC were initially included, but the low melting temperature of Ti limited studies to temperatures of 1300°C and below, so were dropped from additional consideration. Initial oxidation results for Ti and TiC are briefly addressed in Appendix B.

The body of literature concerning the oxidation of early transition metals below 1000°C is extensive. Above this temperature, significantly less has been reported, with few oxidation studies at temperatures higher than $1200\text{-}1400^\circ\text{C}$ [10], [15], [38], [39], [40]. Studies at very high or ultra-high temperatures have been conducted, but many of these focus on low Po_2 environments ($\text{Po}_2 <$

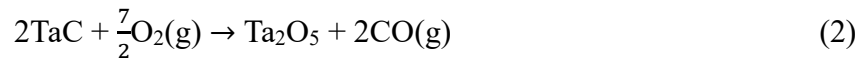
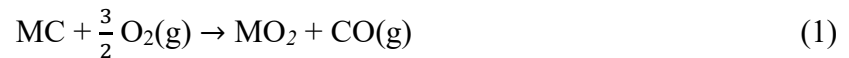
Table 2.1: The melting points of select transition metals, carbides, and oxides. Materials of interest to this study (blue) have all listed melting points higher than SiO_2 (orange).

‘*’ indicates sublimation temperature.

Melting Temperature ($^\circ\text{C}$)	Metal	Carbide	Oxide
Ti	1668	3016	1912 (TiO_2)
Zr	1855	3531	2710 (ZrO_2)
Hf	2233	3928	2800 (HfO_2)
Nb	2477	3600	1511 (Nb_2O_5)
Ta	3017	3999	1877 (Ta_2O_5)
Mo	2623	2580	802 (MoO_3)
W	3422	2785	1472 (WO_3)
Si	1414	2730*	1723 (SiO_2)

1×10^{-2} atm) [11], [12], [38]. More work is needed to elucidate the fundamental kinetic mechanisms which govern the oxidation of these metals at higher temperatures and relevant (near-atmospheric) P_{O_2} .

The oxidation of transition metal carbides has also been studied to great extent at less than 1400°C [16], [19], [20], [21], [22], [23], [25], [28], [41], increasingly so in more recent years as interest in UHTCs has driven research towards high melting point materials. Studies of transition metal carbide thermal and mechanical properties can be found in the ultra-high temperature regime because of their high melting temperatures [17], [24], [26], [27], [28], [42], [43], [44], [45], [46], [47]. However, ultra-high temperature oxidation has only been comprehensively evaluated for HfC by Courtright et al [17]. In general, the carbides will oxidize by the following reactions:



where $M = \text{Ti}, \text{Zr}, \text{or Hf}$ for equation (1). The production of gases at the carbide/oxide interface results in porous solid oxidation products, allowing oxygen to pass through the scale rapidly via gas-phase diffusion. Intuitively, this should allow for more rapid oxidation in carbides as compared to metals, which are expected to form dense scales in the absence of gas-phase oxidation products.

However, there are other mechanisms which may affect transport. For example, the group IV carbides form intermediate “oxycarbide” phases (MC_xO_y) or $\text{M}_x\text{O}_y+\text{C}$ regions at the carbide/oxide interface which may act as a diffusion barrier to oxygen [17], [20], [21], [24], [26], [28] changing the oxidation mechanism to diffusion-limited oxygen transport. Additionally, oxides generally have a greater molar volume than the substrates they grow on. The large change in volume during oxidation can create large growth stresses which can cause oxide cracking and

Table 2.2: Ratio of change in molar volume upon oxide formation, or Pilling-Bedworth Ratios (PBRs) for the materials discussed in this work.

Calculated as $PBR = \frac{V_{Oxide}}{V_{Substrate}}$

	Ti	Zr	Hf	Ta
Metal	1.78	1.54	1.59	2.47
Carbide	1.55	1.41	1.45	2.00

fracture. The ratio between the molar volume of an oxide and the substrate as it grows is known as the Pilling-Bedworth Ratio (PBR). The PBR for each material considered in this work was calculated and is reported in Table 2.2. Note that the PBR is lower for each carbide relative to its corresponding metal.

Additional factors which may affect oxidation either in metals or carbides include nonstoichiometry of the oxide [10], [49] or carbide [28], oxide sintering [17], [23], [50], phase transformations in the oxide [51] or substrate [52], and grain boundary density [28], [48]. This list is incomplete but describes many of the phenomena that will be considered for this work. A list of the potential oxidation mechanism and factors which may complicate the oxidation kinetics is given in Table 2.3. Each item is assigned a number and will be referred to throughout this work to correlate microstructural observations with measured kinetic trends. The effects of CO/CO₂(g) formation in the oxidation carbides could change the mechanism by which oxygen transports through the scale as compared to that formed on the metal, but these differences have never been addressed.

The aim of this work is to understand how the evolution of CO/CO₂(g) during the oxidation of the binary carbides affects the transport of oxygen through the scale as compared to the oxidation of the metal described in Part 1 of this document. Additionally, the oxidation behavior of these materials in AO will be investigated in Part 3. A literature review of the relevant literature is presented below.

Table 2.3: Oxidation mechanisms and non-idealities which may affect kinetics.

No.	Mechanisms	Rate Law
1.	Surface reaction control	Linear
2.	Gas phase diffusion by large defects	Linear
3.	Gas phase diffusion in a growing porous oxide	Parabolic
4.	Solid state diffusion in oxide	Parabolic
5.	Grain boundary oxidation	Parabolic

No.	Non-Idealities	Effect on Kinetics
6.	Decreasing area of substrate	Increase
7.	Short-circuit diffusion	Increase
8.	Densification of the oxide	Decrease
9.	Grain growth of the oxide	Decrease
10.	Increasing oxide plasticity	Decrease
11.	Oxycarbide formation	Decrease
12.	Oxide phase transformation	Variable
13.	Oxygen solubility in substrate	Delay Oxidation

Review of the Literature

a. The Oxidation of Zr and ZrC

The Zr-O binary phase diagram is shown in Figure 2.1 [53]. ZrO_2 is the only thermodynamically stable oxide which forms during the oxidation of Zr and ZrC. ZrO_2 has three major polymorphs: monoclinic (m- ZrO_2) from room temperature to 1170°C, tetragonal (t- ZrO_2) from 1170°C to 2370°C, and cubic (c- ZrO_2) above 2370°C. It is also known to exhibit significant oxygen-deficiency (ZrO_{2-x} , $x < 0.1$) [54], [55]. On cooling, transformation through the c/t and t/m transitions is accompanied by non-negligible volume expansions that have been suggested to play a role in the loss of oxide scale protection [20].

The low temperature phase, α -Zr, is HCP at room temperature. This phase has an extraordinarily high solubility for oxygen (up to 29 at%) and is stabilized by oxygen at high temperatures. The high temperature BCC phase, β -Zr, is present above 862°C when the metal has

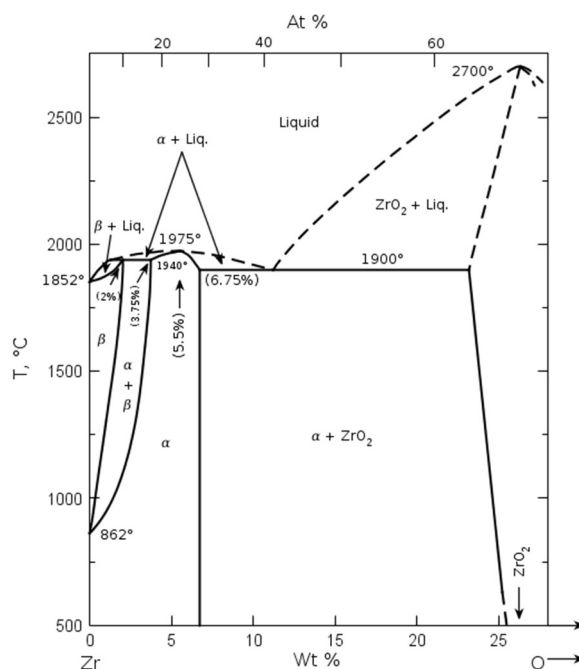


Figure 2.1: The Zr-O phase diagram. JACerS diagram no. 25 [53].

a low oxygen content. There are two notable two-phase regions on the phase diagram which may appear during the oxidation of Zr: the $\alpha+\beta$ region and the $\alpha\text{-Zr}+\text{ZrO}_{2-x}$ region. The $\alpha+\beta$ region is known to form a Widmanstätten-type microstructure with $\alpha\text{-Zr}$ platelets when quenched [50], [55], [56], [57]. Very few studies have reported a two-phase $\alpha\text{-Zr}+\text{ZrO}_{2-x}$ region during oxidation [50], [55].

The oxidation of Zr and Zr-based alloys has been widely studied due to their use as claddings in nuclear reactors. Because of the focus on this industry, the steam oxidation of Zircaloy-type alloys has been much more heavily explored than dry oxygen with the pure metal [50], [56], [58], [59], [60], [61], [62], [63], [64], [65], [66]. Initial onset of oxidation is governed by the dissolution of oxygen into the metal, and oxide formation will not occur before saturation at roughly 29 at% O (See Figure 2.1) [13]. Pemsler presented the only study on the high temperature oxidation of pure Zr in dry oxygen up to 1300°C and found oxidation to follow a parabolic rate law above 1100°C [39], [67], [68]. Oxidation of Zr is well-known to exhibit breakaway behavior after a temperature-dependent critical oxide thickness is reached [69], [70].

The available literature on ZrC oxidation is very complex due to the number of observed behaviors, varying with temperature, oxygen partial pressure, and inconsistencies in starting material. Gasparri et al. summarized ZrC oxidation by developing a kinetic and mechanistic model from 800-1100°C [20]. No oxidation kinetics were reported above this temperature in this study. Shimada investigated the formation of carbon at the ZrC/ZrO₂ interface up to 1500°C, but no kinetics were reported [71]. It is generally agreed that the high temperature oxidation of ZrC proceeds at a linear rate. A two-layered scale forms during oxidation: a porous ZrO₂ outer layer, and compact inner layer comprised of ZrO₂ and carbon [19], [20], [44], [71], [72]. An example of this duplex scale is shown in Figure 2.2. The outer layer grows with linear kinetics, while the inner

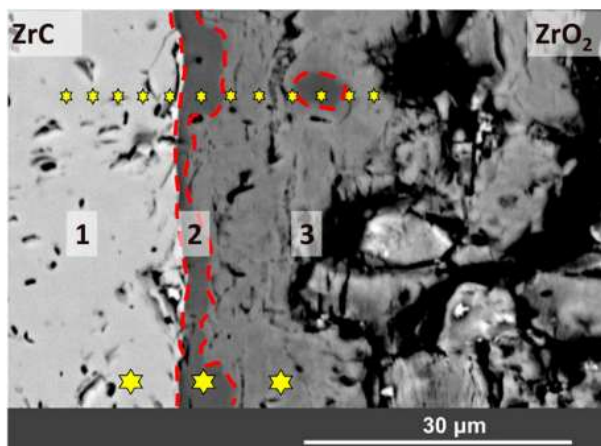


Figure 2.2: The duplex scale structure formed on ZrC. The stars indicate locations where EDS spectra were taken. Reproduced from [20].

layer grows with parabolic kinetics [21]. At a critical thickness, selective oxidation to form ZrO_2 and carbon occurs at the carbide/inner layer interface and oxidation of carbon to $\text{CO}(\text{g})/\text{CO}_2(\text{g})$ at the inner layer/outer layer interface establish a steady state, and the inner layer thickness remains constant for the remainder of oxidation [20].

While ZrC has been widely studied, there is still a significant amount of disagreement between literature sources involving the exact oxidation mechanisms for a few primary reasons. First, ZrC has been shown to spontaneously fracture post-oxidation between 853-1307°C [16] several minutes after cooling, making it challenging to study the oxidation kinetics [16], [25]. Several explanations for this have been presented, including intragranular oxidation followed by cooling [16], the presence of a layer of free carbon [19], and the volume expansion due to the m/t- ZrO_2 transformation [73]. Above these temperatures, the scale is reported to remain adherent. No studies have been conducted which identify the mechanism stopping the spallation behavior.

Second, the nature of the inner layer of the duplex oxide is inconsistent across the literature. Shimada noted the formation of amorphous carbon at the interface and conducted numerous

studies evaluating the mechanisms of formation of this layer at temperatures up to 1500°C [44], [71]. In contrast, Gasparrini et al. found a carbon layer which disappeared above 900°C, finding only sub-stoichiometric ZrO_{2-x} at the interface [19]. However, the presence of this carbon layer seems to be temperature, time, and oxygen pressure dependent [44], [71], [72], but no absolute correlations have been identified. Many authors have also suggested the formation of a transient “oxycarbide” phase at the interface which later breaks down into ZrO_2 and carbon [74]. This has never been directly observed due to ZrC’s ability to retain interstitial oxygen without significantly changing the crystal structure [16], [21]. The nature of the interface could be causing the observed spontaneous spallation. Oxidation studies are needed to investigate the kinetics of ZrC at higher temperatures, as well as understand the effects of carbon oxidation on oxygen transport through the oxide scale.

b. The Oxidation of Hf and HfC

Hf and Zr are well known for having very similar properties and behaviors as a result of the lanthanide contraction [75]. Their properties are so similar that even chemically separating the two metals can be extremely challenging [76]. Similarities between these materials can be easily seen by comparing the phase diagrams and oxidation behaviors.

The Hf-O phase diagram, shown in Figure 2.3 [77], is nearly identical to the Zr-O diagram. The diagram shows the same trends as Zr in phase stability with increasing oxygen content: high oxygen solubility in the metal, followed by a wide two-phase region of α -Hf + HfO_2 , followed again by pure HfO_2 . No reports involving these two-phase regions during oxidation have been reported. At higher temperatures, β -Hf is formed, but the α -Hf polymorph is stabilized by oxygen.

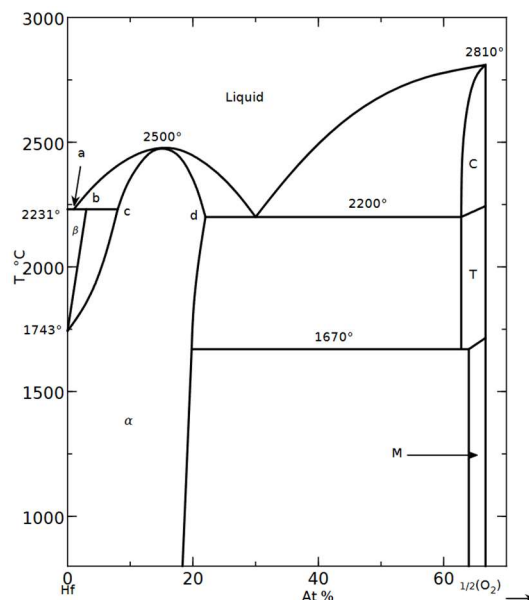


Figure 2.3: The Hf-O phase diagram. JACerS diagram no. 14243 [77].

HfO₂ is the only stable Hf oxide and shares the same polymorphic sequence as ZrO₂: monoclinic (m-HfO₂) from room temperature to 1670°C, tetragonal (t-HfO₂) from 1670°C to 2200°C, and cubic (c-HfO₂) above 2200°C. The metal also transforms from HCP α -Hf to BCC β -Hf at 1743°C. The primary difference between Zr-O and Hf-O phase stability is the higher temperatures for all phase transformations in the Hf-O system. For example, β -Zr forms at temperatures as low as 862°C (Figure 2.1), whereas β -Hf forms closer to 1750°C (Figure 2.3). Additionally, the m-t HfO₂ transition occurs around 1670°C, whereas the m-t ZrO₂ transition occurs around 1170°C.

Due to the high melting point of metal ($T_M \sim 2233^\circ\text{C}$) and oxide ($T_M \sim 2800^\circ\text{C}$), Hf is of great interest as a refractory material. As such, there have been several studies which are concerned with oxidation at very high temperatures. Given the chemical similarity between Hf and Zr, it is not surprising that their oxidation behaviors are also very similar [12]. Smeltzer and Simnad first conducted a kinetic study of Hf oxidation up to 1200°C in oxygen and found parabolic kinetics, assuming a similar mechanism to Zr oxidation [78]. Pemsler [40], [79] evaluated the oxidation

kinetics up to 1400°C in oxygen and found similar behavior. Kofstad [12] studied oxidation up to 1700°C in reduced oxygen environments. More data is needed on HfC oxidation kinetics at higher temperatures and oxygen pressures which will further elucidate its refractory capabilities.

HfC possesses the second highest melting temperature of all known binary compounds ($T_M \sim 3928^\circ\text{C}$) and, therefore, oxidation resistance in the ultra-high temperature regime is of interest [16], [17], [24], [27], [43]. However, the literature regarding the kinetic rate laws for HfC vary in their conclusions. A few studies have stated the oxidation of HfC follows a linear rate law. Berkowitz-Mattuck reported HfC oxidation between 1517°C and 1723°C was linear and proceeded via grain boundary oxidation [16]. Others have reported a parabolic rate law, though there is also disagreement within these studies [17], [24], [80]. Courtright et al. explored the oxidation kinetics across 1200-2200°C and found them to be parabolic at all temperatures. A change in oxidation mechanism was identified around 1800°C [17]. Below 1800°C, the oxide scale is porous and gas-phase diffusion governs oxygen transport according to the counter-current gas-diffusion model described by Holcomb et al [81]. As temperatures near 1800°C, oxidation slows because oxide sintering reduces the available pore volume in the oxide, limiting oxygen transport to a Knudsen diffusion mechanism. However, Holcomb also reported that the oxidation rate of HfC between 1200-1530°C varied minimally with temperature, so this observation is inconsistent. Above 1800°C, they suggested that solid-state diffusion of oxygen through HfO₂ becomes dominant, causing oxidation rate increases with increasing temperature.

The duplex scale formed on HfC is a well-reported phenomenon and an example is shown in Figure 2.4. Bargeron noted that the inner layer was very dense while the outer layer was very porous up to 2060°C, indicating an oxidation front at the inner layer/outer layer interface [24]. This dense layer is often referred to as an “oxycarbide” but is more correctly identified as oxide

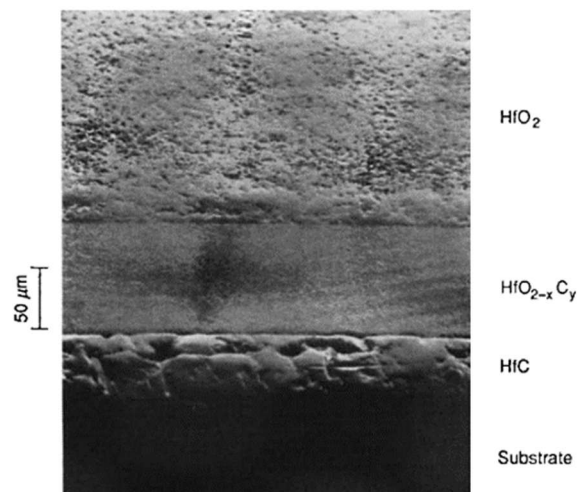


Figure 2.4: The duplex scale structure formed on HfC. Reproduced from [24].

with free carbon, shown microstructurally in Figure 2.5 [24], [26], [80]. Scott, He, and Lipke further investigated the oxide and carbon layer. They found that above about 1800°C, selective oxidation of Hf is no longer preferential and the carbon-containing inner layers are absent [26], [80]. The *t/c*-HfO₂ polymorphs have also been found in the inner layer, providing further evidence for the nano-segregated oxide microstructure, as these polymorphs are stabilized by surface energy at very small sizes [82]. These results suggest that the oxidation of HfC, and potentially the other group IV carbides, is heavily linked to microstructural development during oxidation.

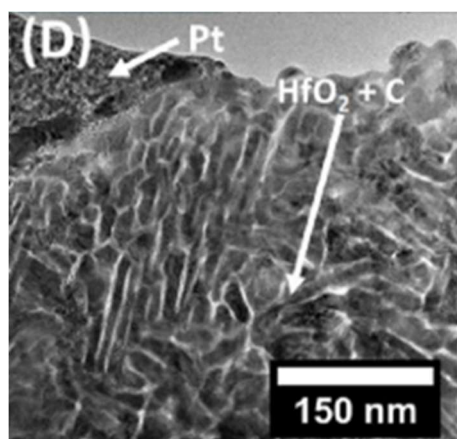


Figure 2.5: Phase separated HfO₂+C in the inner layer the scale formed on HfC. Reproduced from [26].

The study by Courtright is the only comparison of oxidation kinetics known to the author between a metal and its carbide. However, the comparison is not very quantitative, as the oxidation data of HfC is compared to an extrapolated dataset taken from a study by Smeltzer and Simnad [78] of Hf oxidation measured via thermogravimetric methods at lower temperatures (350-1200°C) conducted 36 years prior to Courtright et al.'s work. Additionally, Courtright et al. used two different oxidation techniques to measure the oxidation rate of HfC: thermogravimetric studies from 1200-1530°C, and CO₂-laser heating experiments from 1800-2200°C. The inconsistency highlights the need for comprehensive and self-consistent comparative studies to evaluate oxidation kinetics and mechanisms.

c. The Oxidation of Ta and TaC

The phase diagram of the Ta-O system is shown in Figure 2.6 [83]. The only stable oxide formed on Ta-based materials is Ta₂O₅. Pure Ta₂O₅ ($T_M \sim 1880^\circ\text{C}$) has two polymorphs which it may adopt: a low-temperature orthorhombic phase (β - or L-Ta₂O₅) or a high temperature tetragonal phase (α - or H-Ta₂O₅). The crystal structure of the low-temperature phase is of some debate because it is incommensurately modulated, also called an “infinitely adaptive” or “vernier” structure [84], [85], [86], [87], [88], [89], [90], [91], [92], [93]. In the case of L-Ta₂O₅, this means that the *b* lattice parameter changes with temperature, processing history, and other factors [87]. It has been suggested that the oxygen-deficient nature of the oxide allows for this behavior by creating or destroying oxygen anion sites, rather than forming point defects, to change the crystal size without disrupting the Ta sublattice [84]. This also means that the oxygen site stoichiometry is not maintained, and thus describing the defect structure of L-Ta₂O₅ cannot be accomplished with

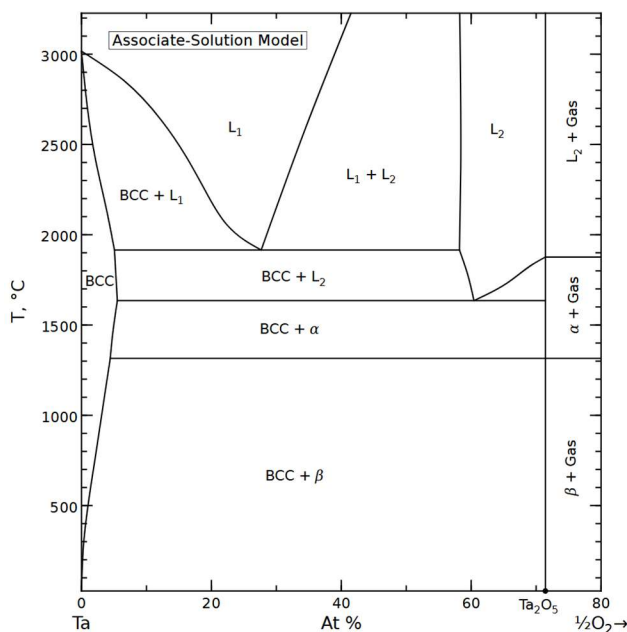


Figure 2.6: The Ta-O phase diagram. JACerS diagram no. 17438-B [83].

traditional Kröger-Vink notation [84]. Identifying the lattice parameters of oxide structure can be accomplished via X-ray diffraction (XRD) techniques [94], but XRD cannot reveal the specifics of what causes the changing structure. This has made understanding this phase very difficult and the details of the L-Ta₂O₅ crystal structure which are grown during oxidation have not been explored.

The H-Ta₂O₅ phase has also been historically difficult to study due to the nature of the L/H phase transformation. The transformation ($T_f \sim 1360^\circ\text{C}$) is very sluggish and reversible, and the oxide will fully revert to the orthorhombic L-Ta₂O₅ phase if cooled slowly from above this temperature [93], [95], [96], [97]. When quenched, however, the oxide transforms through a series of metastable polymorphs and has been reported as either a monoclinic or triclinic phase rather than reverting to the orthorhombic L-Ta₂O₅ [95], [97]. The crystal structure of the H phase was of significant debate due to the inability to quench the H phase to room temperature, but recent developments have provided greater insight into the structure [98].

Ta-based materials have an extremely high molar volume change upon oxidation to Ta_2O_5 (PBR ~ 2.5 and ~ 2.0 for Ta and TaC, respectively). As such, the oxides are generally non-protective due to cracks that form because of growth stresses. Because of this, the metal oxidizes extremely quickly at near atmospheric oxygen levels. The oxidation of pure Ta was studied by Kofstad at a range of temperatures and oxygen pressures [9], [10], [38]. At >1 torr Po_2 , they suggested that diffusion through the oxide scale is the rate-limiting step; however, significant variation in the oxidation rate above 1200°C prevented accurate study of the oxidation mechanisms at high temperatures and Po_2 s. It was suggested that the H- Ta_2O_5 phase is stabilized at reduced Po_2 (< 0.01 torr) and can form at temperatures as low as 1250°C , shown in Figure 2.7. The presence of both phases in the scale may cause the oxidation mechanism to change. However, these dual-phase scales have not been reported elsewhere.

TaC has the highest melting temperature of the known binary compounds ($T_M \sim 3999^\circ\text{C}$), making it an extremely interesting material for refractory and ultra-high temperature applications. However, it oxidizes very rapidly via grain boundary attack which causes grain lift-out as oxidation

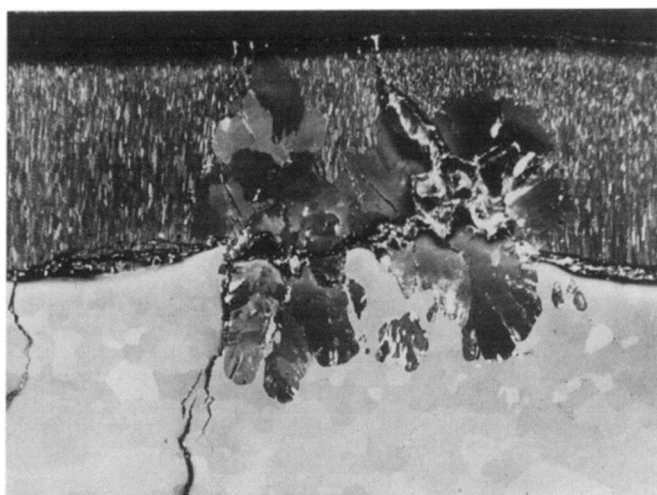


Figure 2.7: A cross section of Ta oxidized for 80 min at 1250°C in 10 Torr Po_2 . The primary scale is believed to be L- Ta_2O_5 , while the phase in the middle is believed to be H- Ta_2O_5 . Reproduced from [10].

progresses, shown in Figure 2.8 [48]. The oxide scale is fully porous and gives rise to linear kinetics. TaC exhibits even greater carbon sub-stoichiometry than ZrC, reaching to as low 33 at% (Ta_2C). The carbon content in TaC has been shown to affect the oxidation kinetics [28] and should be evaluated prior to study. For example, Desmaison-Brut et al. found that the monocarbide does not form an intermediate “oxycarbide” phase, while the hemicarbide (Ta_2C) does [28].

Because the oxidation of Ta and TaC is so rapid at high temperatures, no additional investigation of the oxidation behavior at high temperature ($T > 1300^\circ C$) and P_{O_2} has been conducted. Despite the differing oxide structures, the equilibrium oxide phase assemblage which forms in a P_{O_2} relevant to hypersonic applications at high temperatures and the effects that they have on the oxidation process have yet to be established. Thus, the oxidation of Ta and TaC should be evaluated in identical conditions to extend the upper temperature limit of existing literature, to evaluate the differences in oxidation behavior when carbon is present in the system, and to evaluate the effects of the phase transition on oxidation.

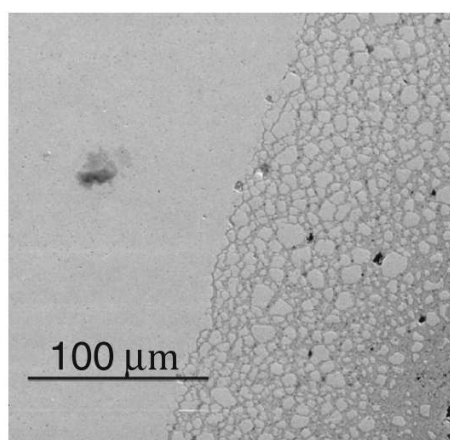


Figure 2.8: A cross section of TaC oxidized under an oxyacetylene torch for 60s (maximum surface temperature $2100^\circ C$) highlighting the grain boundary attack and grain lift-out mechanism in TaC. Reproduced from [48].

Part 1: The Role of Carbon in the High Temperature Oxidation of Transition Metals and Carbides

a. Oxidation Method

Oxidation experiments were carried out for M vs. MC (M = Ti, Zr, Hf, Ta) which allow for the direct comparison of the effects of carbon oxidation on oxygen transport through the scale. These experiments were conducted in a custom **resistive heating system (RHS)** with the sample geometry shown in Figure 3.1a and Figure 3.1b, respectively. The RHS, based on the design pioneered by Karlsdottir and Halloran [99] and iterated upon by Shugart and Opila [49] and Backman and Opila [100], utilizes Joule heating to achieve sample temperatures into the ultra-high temperature regime. The “dogbone” shape of the sample takes advantage of the inverse relationship between resistance and cross section area to localize the “hot zone” to the center of the specimen (Figure 3.1b, orange circle). An emissivity correcting pyrometer (Pyrofiber Lab, Pyrometer Instrument Co., Windsor, NJ) is used to measure the sample temperature in the hot zone and actively adjust for changing optical properties as the material oxidizes. This pyrometer is in a feedback loop with a Eurotherm controller (BPAN controller, MicroPyretics Heaters International,

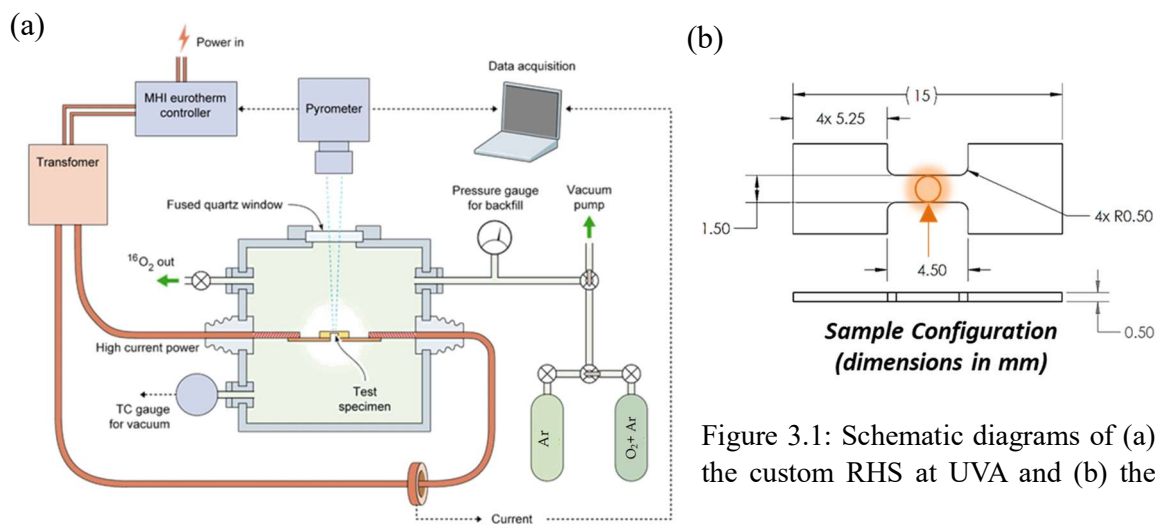


Figure 3.1: Schematic diagrams of (a) the custom RHS at UVA and (b) the

Inc., Cincinnati, OH) to achieve the temperature of interest. Temperature control can be maintained at and below 1800°C with an accuracy of roughly $\pm 20^\circ\text{C}$ at 1300°C and $\pm 50^\circ\text{C}$ at 1800°C. The sample is enclosed in a steel chamber during heating which allows for precise control over the oxidizing environment. Samples are clamped to conductive leads using alligator clips. Yttria-stabilized zirconia (YSZ) pads and Pt foil are placed between the sample and the clips to minimize reactivity. The hot zone of the sample is not in contact with any surface, minimizing impurities introduced during oxidation.

For this work, samples were ramped to the desired temperature in ultra-high purity Ar at a flow rate of 1000 sccm. Oxidation was carried out in a 1% O₂ – bal. Ar environment at atmospheric pressure, also at 1000 sccm. This P_{O₂} was selected to reduce the oxidation rate, and thus the oxidation kinetics can be evaluated against temperature, time, and microstructural features. Thus, the role of carbon can be highlighted in M vs. MC experiments, where the only difference between the experiments is the chemistry of the substrate. Recession of the base material was the primary comparative metric because factors like oxide sintering and varying PBR may skew comparisons made via oxide thickness. Weight gain cannot be used because dogbone samples are not heated uniformly across their entire length in the RHS. Oxidation temperatures were selected based on the lowest melting temperature in each material system. Oxidation times were selected as such that a significant scale is grown on each material, but that the sample is not consumed.

Samples were analyzed post-oxidation in plan view and in cross section at the hot zone. In plan view, scanning electron microscopy (SEM; Quanta 650 FEG-SEM, FEI Company, Hillsboro, OR) and energy dispersive X-ray spectroscopy (EDS; Oxford Instruments, Abingdon, UK) were used to characterize oxide surface morphologies. X-ray diffraction (XRD; Empyrean Diffractometer, Malvern Panalytical, Malvern, United Kingdom) was used to determine which

oxide polymorph forms on the outer-most scale. In cross section, SEM was used to measure oxide growth/material recession for oxidation kinetics. SEM/EDS was used to correlate the sample microstructures in both fracture and polish cross section to the oxidation experiments. Tracer oxidation experiments utilizing heavy oxygen isotope $^{18}\text{O}_2$ in conjunction with time-of-flight secondary ion mass spectrometry (TOF-SIMS; TOF-SIMS V, ION TOF, Inc., Chestnut Ridge, NY; C. Zhou, North Carolina State University) were used to monitor oxygen isotope diffusion through the oxide scales. Light microscopy (LM; RH-8800 Light Microscope, Hirox Co. Ltd., Tokyo, Japan) was used to identify non-stoichiometry in the oxide via color. Instrumental gas analysis (IGA; Eurofins EAG, Syracuse, NY) was used to determine the carbon stoichiometry of the carbide materials. Raman microscopy was used to study free carbon identified in the ZrC system.

Before oxidation, a high-resolution transmission electron microscope (TEM; Themis-Z STEM, Thermo Fisher Scientific, Waltham, MA) equipped with selected area electron diffraction (SAED) was used to probe the crystallinity of the carbides and to verify that the resulting carbon signal is all from the carbide phase and not from any free carbon. Focused ion beam (FIB; Helios DB FIB-SEM, FEI Company, Hillsboro, OR) milling was used to make thin foils of the carbides.

Oxidation kinetics based on material recession were plotted to determine the relevant rate laws. Recession values were measured from the center third of the base material. Data points represent averages from two or more samples, of which 10-20 data points were taken from each sample. Error bars represent one standard deviation. Recession data was plotted versus t , $t^{1/2}$, and on log-log plots and R^2 values for each temperature were compared to estimate the kinetic rate law. Due to the large error bars for the data, many rate laws demonstrated good fits to the data. Rate laws which fit the oxidation data with the highest R^2 value were considered as the probable rate law. Here, the oxidation kinetics are plotted versus linear time for simplicity.

b. Oxidation of Ta vs TaC

i. Experimental Method

A sheet of 0.635 mm (0.020 in.) thick Ta (99.5% pure, metals basis) was sectioned into RHS specimens via electrical discharge machining (EDM; Exothermics, Inc., Amherst, NH, USA). EDM samples were lightly ground with P1200 SiC foils to remove residue from the machining process. Three-inch TaC pucks produced by hot isostatic pressing (HIP; Kurt J. Lesker Company, Pittsburg, PA) were diamond machined (Bomas Machining Specialties, Inc., Woburn, MA) into the dogbone geometry of 0.5 mm (0.020 in) thick. Archimedes method gave a density of 14.3 g/cm³, or 99.3% of theoretical density, and IGA determined the TaC to be highly stoichiometry TaC_{0.998}. HRTEM also showed the carbide was highly crystalline and had no free carbon, shown in Figure 3.2.

Ta and TaC were oxidized at 1300°C, 1400°C, and 1500°C for up to 10 min at each temperature in 1 atm of flowing 1% O₂ – Ar. These temperatures were chosen because 1300°C was the highest temperature reported previously for the oxidation of pure Ta [10], [38]. These times were chosen because oxidation of 10 minutes or longer was nearly complete for Ta in these conditions. In some cases, especially at 1500°C for TaC, samples would break before the desired

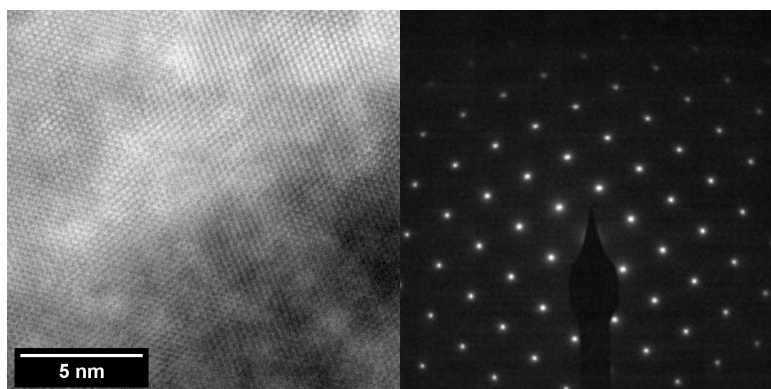


Figure 3.2: Example of a (a) HRTEM micrograph and (b) SAED pattern from a piece of an unoxidized TaC specimen.
TEM and SAED thanks to H. Heinrich.

end time. Because fracture stops current flow, and thus heating, these samples were still included in the data set with an end time at the time of fracture. Additional Ta samples were oxidized at 1300°C for 2, 5, 10, 20, and 50 min in 1000 ppm Po_2 – Ar to verify that oxidation rate law is limited by oxygen transport through the scale, not the rate of reaction. All resulting oxides were imaged in plan view and cross section using SEM. Cracking of the oxide scale on Ta and oxide scale porosity on TaC were quantified via image thresholding in ImageJ [101]. The oxide scale was isolated by masking the images, then the threshold of the oxide scale was adjusted such that only the features of interest were highlighted. The area fraction of these features as compared to the total area of the isolated oxide scale is reported as the area fraction of such features. Grain size of the oxide was measured in plan view using the average linear intercept method.

Tracer oxidation experiments were conducted on Ta samples at 1300°C and 1400°C. Samples were oxidized per the procedure above for 4.5 minutes in a standard laboratory grade mixture of 1% $^{16}\text{O}_2$ – bal. Ar ($^{18}\text{O}_2$ natural abundance 0.2%), then oxidized a second time in a highly enriched heavy oxygen atmosphere ($^{18}\text{O}_2$ 97% enriched) (Sigma Aldrich, Saint Louis, MO). Samples were kept at temperature between oxidizing atmospheres while the chamber was evacuated and backfilled with ultra-high purity Ar. The chamber was filled to around -100 Torr gauge pressure with Ar before $^{18}\text{O}_2$ was introduced, to maintain a somewhat low Po_2 (~10% $^{18}\text{O}_2$ – bal. Ar). The second oxidation time varied from 10-30 seconds. The time was not strictly kept because the goal was to identify transport pathways and not to track transport kinetics. ToF-SIMS was used to generate isotope maps of the oxide cross sections.

The formed oxides were analyzed using XRD equipped with micro-focus incident optics. Due to the small size of the samples and the incident beam (720 x 720 μm), the signal-to-noise ratio was poor. To improve the analysis, two additional samples of Ta were oxidized to completion

in a box furnace in air. One sample was exposed to 1300°C and the other 1450°C, both for one hour, and then air quenched. To prevent impurities during oxidation, these samples were placed on small pucks of sintered pure Ta₂O₅, which were placed on small sheets of Pt foil. The resulting oxides were ground to a powder with a mortar and pestle, then analyzed with powder XRD to obtain reference diffraction patterns from below and above the L/H-Ta₂O₅ phase transition temperature (~1360°C). This was not done for TaC, due to a low supply of samples.

ii. Results

Figure 3.3 shows XRD analysis indicating only two oxide phases grown on both Ta and TaC: L-Ta₂O₅ and H'-Ta₂O₅ (quenched high temperature phase). Due to poor signal-to-noise ratios in the data, representative XRD data from Ta fully oxidized at 1300°C and 1450°C are shown.

Charts describing the oxidation mechanisms observed during the oxidation of Ta and TaC are shown in Figure 3.4 and 3.5, respectively. Representative cross sections of the hot zone for each area of the diagrams are also displayed in the figures. A cross section from each major

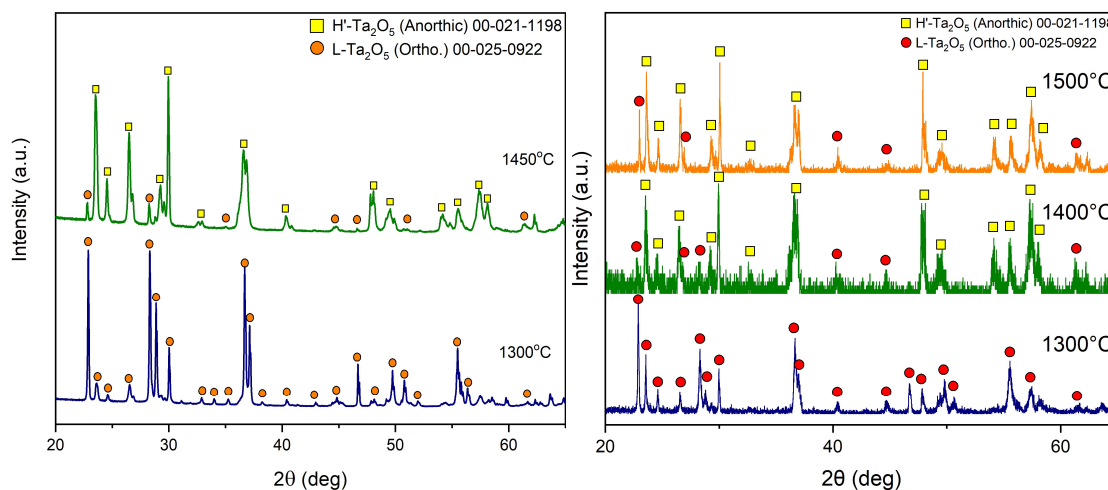


Figure 3.3: (Left) Powder XRD from Ta samples completely oxidized in a box furnace and (Right) XRD from TaC samples oxidized for 5 min in 1% O₂, showing the L- and H'-Ta₂O₅ oxide phases. The tetragonal H-Ta₂O₅ is not stable at room temperature and quenches into the H' phase when cooled below the phase transformation temperature (~1360°C).

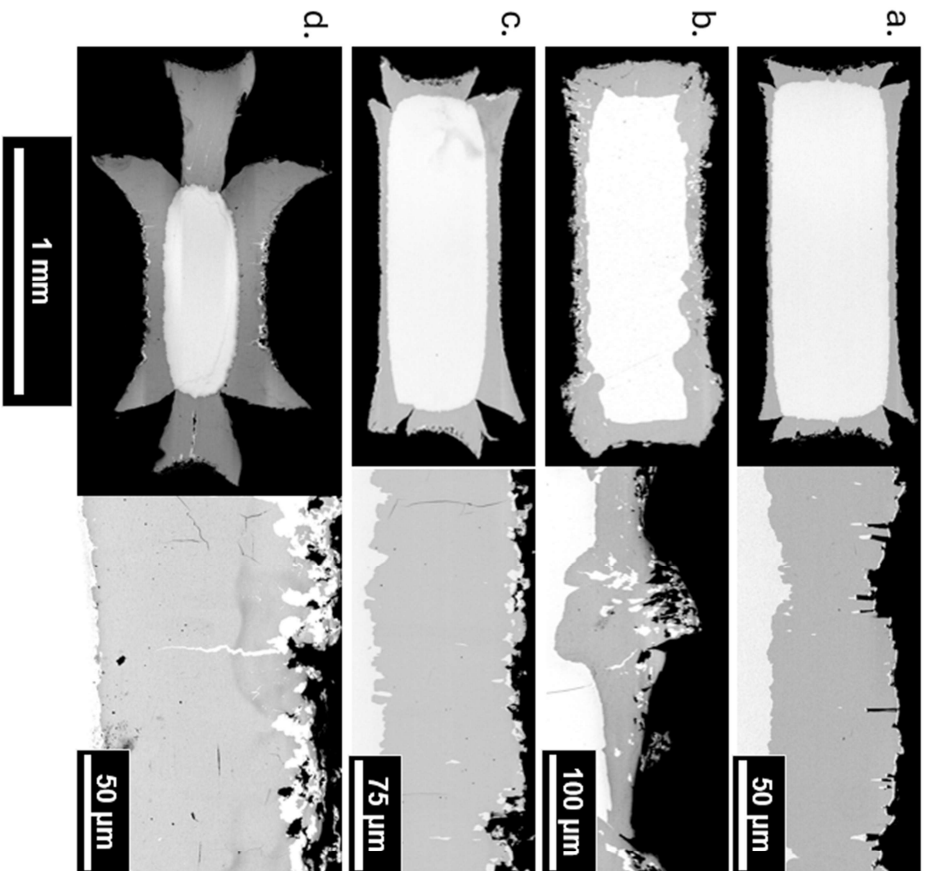
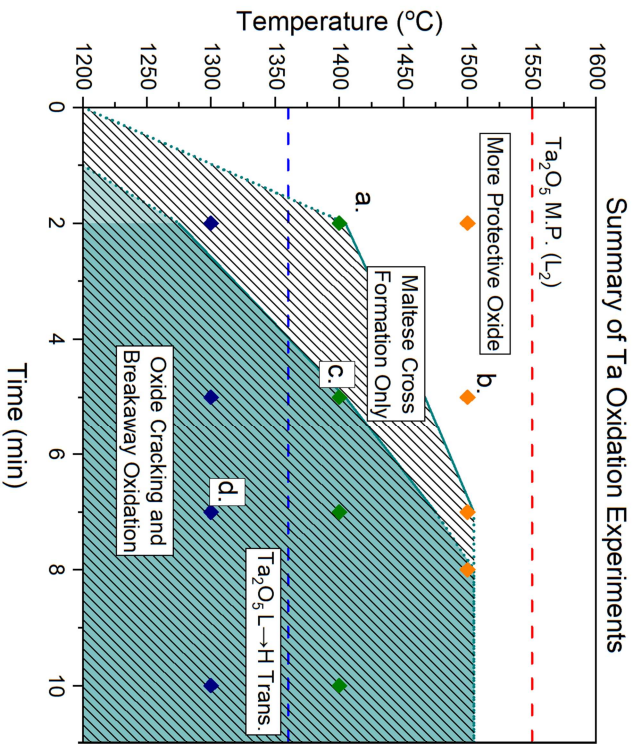


Figure 3.4: (Left) Chart summarizing the Ta oxidation experiments conducted and the identified relevant mechanisms to the oxidation rate. Data points marked with a letter refer to the micrographs shown on the right side. (Right) Micrographs of samples which are representative of each area shown on the graph. From top to bottom: (a) post-oxidation at 1400°C for 2 min, showing Maltese cross formation, but no oxide cracking; (b) post-oxidation at 1500°C for 5 min, showing no Maltese cross formation or oxide cracking; (c) post-oxidation at 1400°C for 5 min, showing both Maltese cross formation and oxide cracking; and (d) post-oxidation at 1300°C for 7 min, showing extensive Maltese cross formation and heavy oxide cracking. Boundaries are drawn as straight lines between data points and do not represent explicit data measurements.

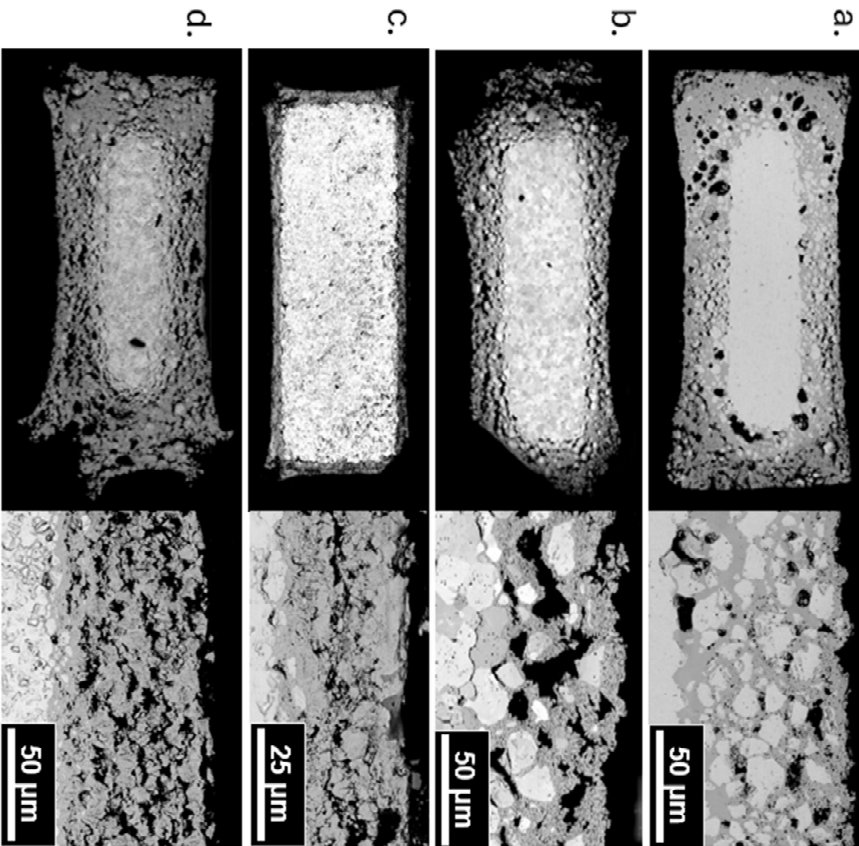
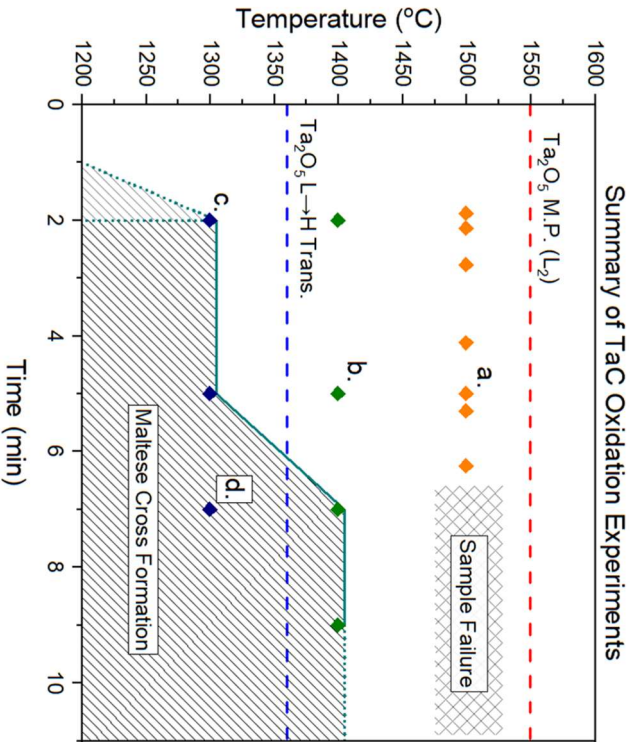


Figure 3.5: (Left) Chart summarizing the TaC oxidation experiments conducted and the identified relevant mechanisms to the oxidation rate. Data points marked with a letter refer to the micrographs shown on the right side. (Right) Micrographs of samples which are representative of each area shown on the graph. From top to bottom: (a) post-oxidation at 1500°C for 5 min, showing no Maltese cross formation, extensive void coalescence, and extensive TaC grain lift-out; (b) post-oxidation at 1400°C for 5 min, showing no Maltese cross formation and grain lift-out; (c) post-oxidation at 1300°C for 2 min, showing extensive Maltese cross formation, but no grain lift-out; and (d) post-oxidation at 1300°C for 7 min, showing extensive Maltese cross formation and no grain lift-out. Boundaries are drawn as straight lines between data points and do not represent explicit data measurements.

mechanism change is shown at various temperatures and times explored. Additional micrographs for all explored conditions can be found in Appendix A.

For both materials, the corners of the oxides sometimes are flayed outwards in a ‘Maltese cross’ morphology. As shown in Figures 3.4 and 3.5, the formation of this morphology is dependent on temperature and time. At 1300°C both materials exhibit this cross morphology at all times. At 1400°C, the oxide on Ta still shows this cross morphology, but the oxides on TaC do not split at the corners. At 1500°C, the oxides on Ta remain intact until 7 minutes of oxidation, whereas the oxide corners on TaC are always completely intact.

The initially grown oxide scale on Ta is a dense, single-layer scale (Figure 3.4a). Some unreacted Ta metal can be found within the scale. The oxide also exhibits significant cracking which varies with temperature and time. Figure 3.6 shows the area fraction of the oxide scales occupied by cracks after Ta oxidation for 5 min. At lower temperatures and longer times, the oxide scale is found to crack more, whereas the scale remains more intact at higher temperatures and shorter times.

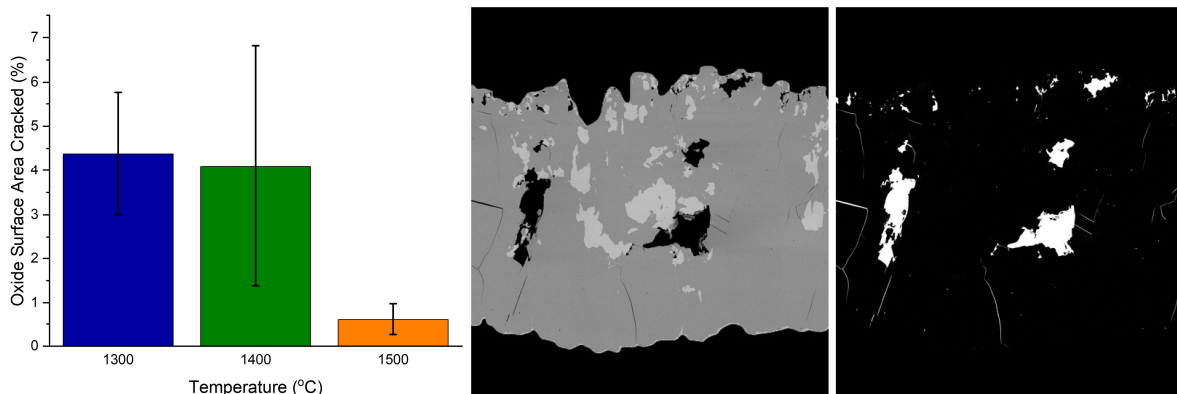


Figure 3.6: Area fraction measured in cross section of oxide scale on Ta occupied by cracks and voids at each temperature after 5 min of oxidation. Error bars represent standard deviation of values measured across multiple samples. An example scale from Ta oxidized at 1400°C for 5 min in 1%O₂ – Ar and its thresholded image are shown on the right.

The oxide grown on TaC is also a single layer containing extensive pore and void networks at all temperatures and times due to CO(g) egress. Unlike Ta, the oxide does not show signs of cracking. Similar to Ta, a large degree of unreacted TaC can be seen in the oxide scale, primarily towards the carbide/oxide interface. Additionally, as temperature increases, an increasing amount of these carbide grains can be found in the oxide scale. Higher magnification micrographs, such as that shown in Figure 3.5b, show oxide growth at the grain boundaries of the TaC.

Figure 3.7 shows plan view images of the surfaces of the oxides formed on Ta and TaC after oxidation at 1400°C for 5 min. Figure 3.8 shows the amount of the oxide surfaces occupied by voids, pores, or cracks as a function of temperature and time. For Ta, the area fraction of the oxide surface occupied by large scale defects decreases with time at all temperatures. The trend of the defects with temperature is not monotonic. From 1300°C to 1400°C , the area fraction increases, then decreases substantially after oxidation at 1500°C . For TaC, the oxide exhibits fine, well-rounded grains with small holes and pores, attributed to the CO(g) evolution during oxidation.

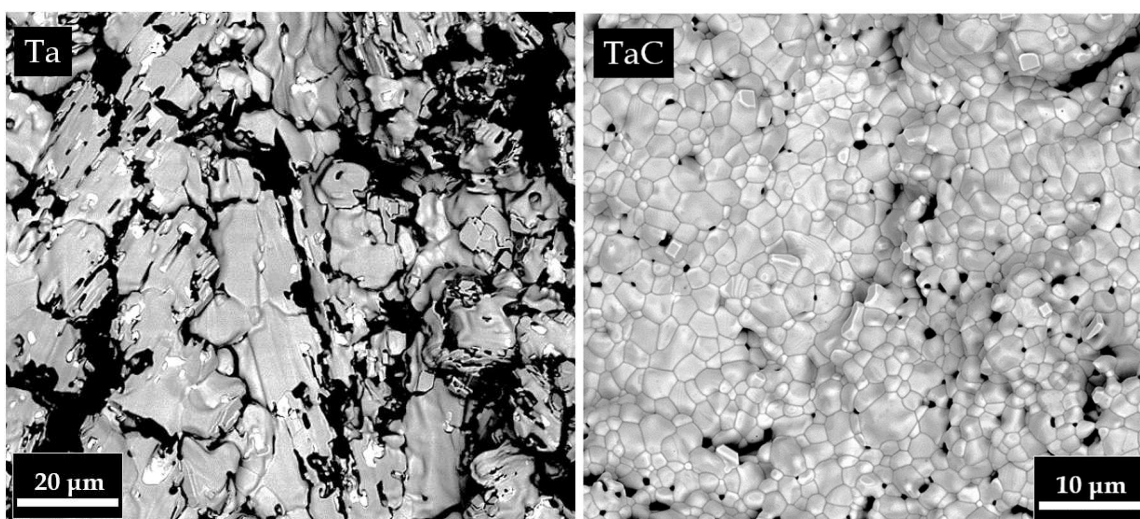


Figure 3.7: (Left) Backscatter SEM plan view micrograph of the oxide formed on Ta after 5 min of oxidation at 1400°C in 1% O_2 – bal. Ar. Note the large plate-like conglomerates of Ta_2O_5 grains. (Right) Backscatter SEM plan view micrograph of the oxide formed on TaC after 5 min oxidation at 1400°C in 1% O_2 – bal. Ar. Note the fine grains of Ta_2O_5 with intergranular holes for escaping CO(g) created during oxidation.

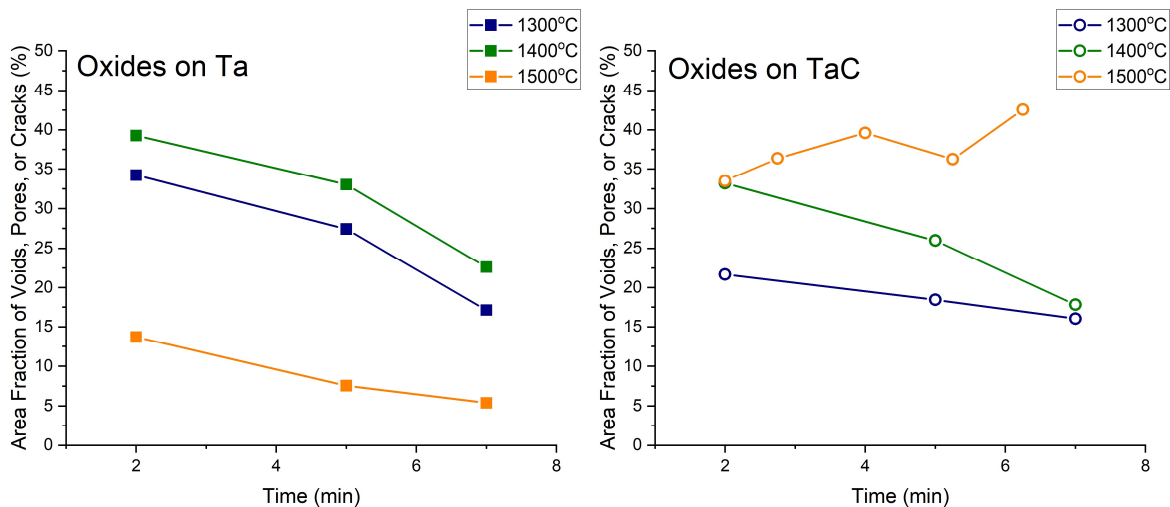


Figure 3.8: Area fraction of voids, pores, or cracks found in plan view on the oxides grown on (left) Ta and (right) TaC. Measured via image thresholding.

Maximum surface porosity/cracking in the oxide formed on TaC is found after 6.25 minutes of oxidation at 1500°C. Void, pore, and crack fraction on the surface of the oxides decreased with time in almost all cases, except at 1500°C on TaC. Figure 3.9 shows the change in grain size on the oxide surface grown on Ta and TaC with temperature and time, showing an increase in average grain size as both temperature and time increase. At 1500°C, Ta exhibits an order of magnitude larger oxide grain growth rate. The grains found on TaC are always smaller than the grains found on Ta.

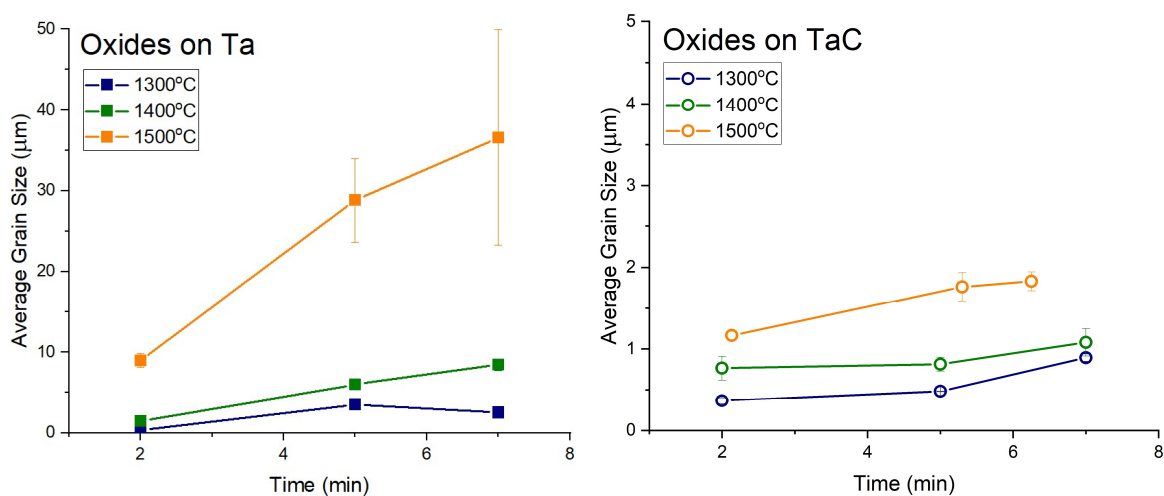


Figure 3.9: Average grain size as measured in plan view on the oxides grown on (left) Ta and (right) TaC. Measured via the average line intercept method. Note the difference in y-axis scale.

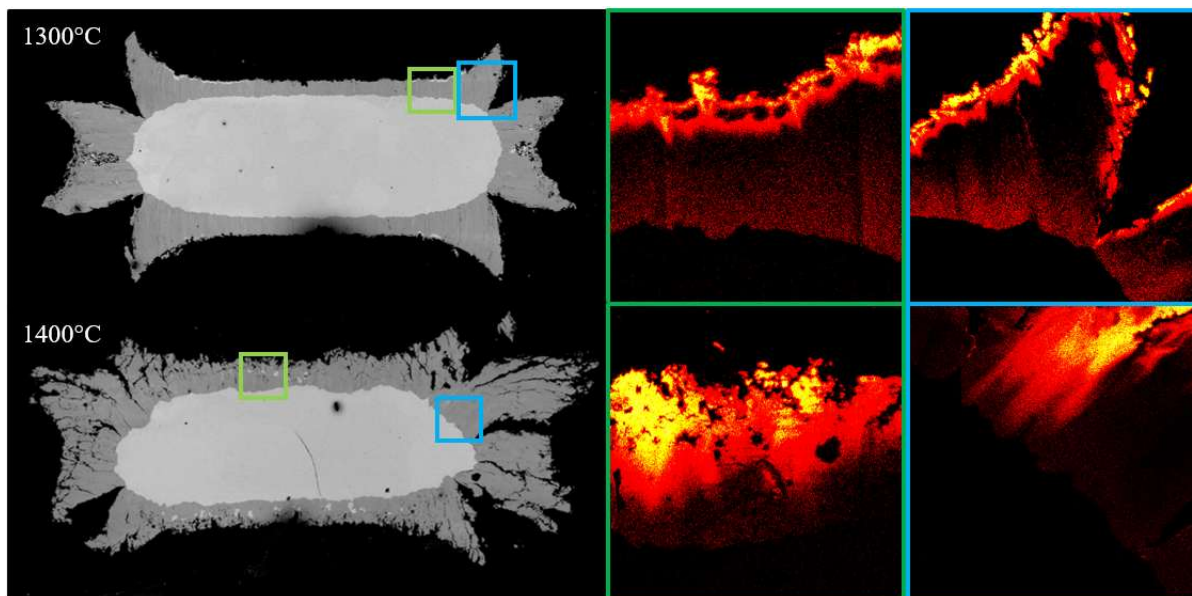


Figure 3.10: Polished cross sections and ToF-SIMS ^{18}O isotope maps of after tracer oxidation for 4.5 minutes in $^{16}\text{O}_2$. Top row oxidized for 6 seconds in $^{18}\text{O}_2$ at 1300°C , bottom row oxidized for 20 seconds in $^{18}\text{O}_2$ at 1400°C . Results courtesy of C. Zhou (North Carolina State University).

Cross sections and ^{18}O isotope maps from ToF-SIMS of Ta from tracer oxidation experiments are shown in Figure 3.10. One sample each is shown for oxidation at 1300°C and 1400°C . The sample oxidized at 1300°C was oxidized for 4.5 minutes in $^{16}\text{O}_2$, then 6 seconds in $^{18}\text{O}_2$. The sample oxidized at 1400°C was oxidized for 4.5 minutes in $^{18}\text{O}_2$, then 20 seconds in $^{18}\text{O}_2$. In the center of both Ta samples, ^{18}O is largely found on the surface of the oxide scale. After 1300°C exposure, cracks in the oxide at 1300°C can be seen highlighted with ^{18}O signal and an increased signal of ^{18}O can be found at the metal/oxide interface, though there is negligible ^{18}O found between this interface and the surface. After 1400°C exposure, no cracks containing ^{18}O are visible, and the ^{18}O signal is limited to the outer surface of the oxide. No increased ^{18}O signal is visible at the metal/oxide interface.

The recession of the base material was measured from cross section SEM images with ImageJ [6]. The results were plotted versus time to evaluate the oxidation kinetics, shown in Figure 3.11. At short times, Ta recession is found to be parabolic at all temperatures. At longer times for

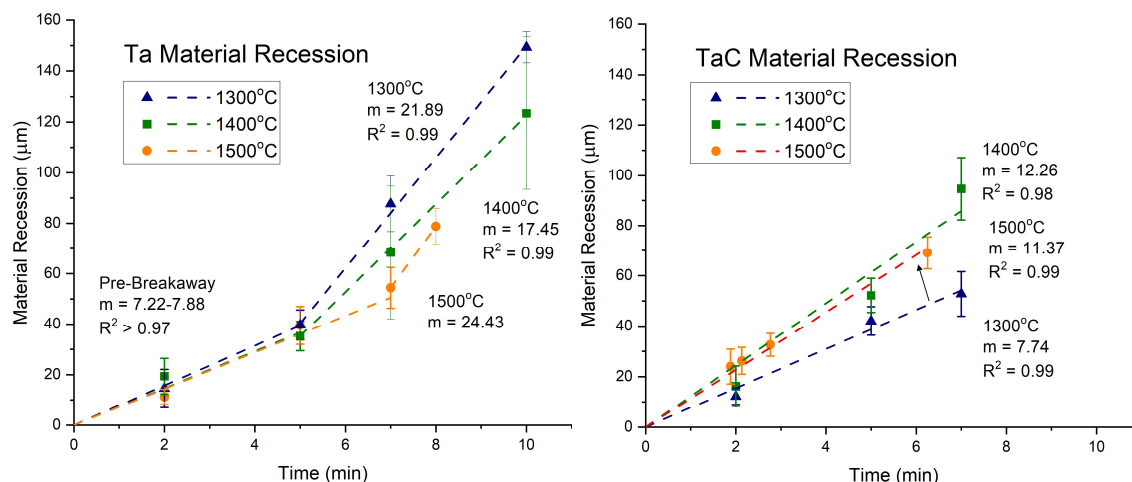


Figure 3.11: Comparison of the oxidation kinetics for Ta and TaC at 1300-1500°C in 1%O₂-Ar. The black arrows follow the direction of increasing temperature to highlight the abnormal behavior for Ta oxidation at 1300°C.

Ta and for all times for TaC, recession rates were found to be linear at all temperatures. For Ta, differences in initial parabolic recession up to 5 min of oxidation are negligible at all measured temperatures. Breakaway oxidation is observed, and onset is between 5-8 min, with higher temperatures having a longer time to breakaway onset. After breakaway begins, the oxidation rate becomes linear and increases by a factor of between 2.2 to 3.3 times. Although based on limited data, post-breakaway, the oxidation rate of Ta decreases from 1300°C to 1400°C, then increases again when temperature is raised to 1500°C. The TaC recession rate is uniformly linear at all measured times. The rate increases from 1300-1400°C and does not change significantly from 1400-1500°C.

The recession rate of Ta oxidized under 1000 ppm Po₂ is shown in Figure 3.12. The initial recession follows a parabolic rate law (shown by the dotted line) up to 10 min, then exhibits a similar breakaway behavior and recession becomes linear.

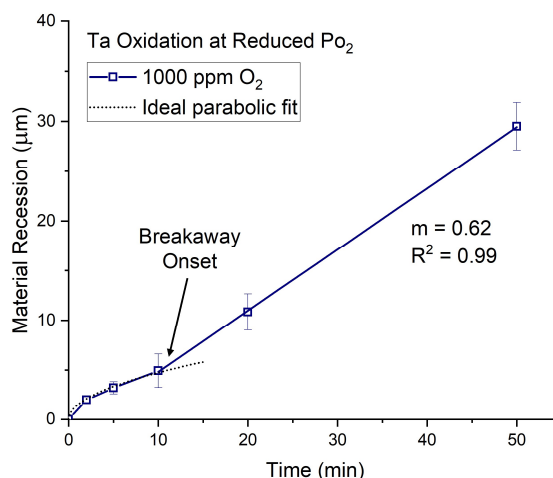


Figure 3.12: Oxidation kinetics for Ta at 1300°C in 1000 ppm O₂-Ar.

iii. Discussion

IGA and TEM/SAED (Figure 3.2) indicate that the TaC used in this study is highly stoichiometric and crystalline monocarbide phase. XRD indicates that the oxide phase formed on Ta and TaC are the same at each respective temperature. Additionally, assuming that the high temperature oxidation reactions for Ta and TaC are rapid relative to oxygen transport via gas-phase or solid-state diffusion, the changing recession kinetics shown are ideally indicative of the transport mechanisms through the scale. Differences in substrate grain size ($\sim 200\mu\text{m}$ in Ta, $\sim 40\mu\text{m}$ in TaC) are not expected to significantly affect the oxidation kinetics, as the substrate will readily react with any available oxygen before it has time to transport through the grain boundaries. Thus, differences in oxide microstructure driven by substrate chemistry are expected to be responsible for differences in oxidation kinetics.

The initial parabolic recession rate up to 5 min for Ta is indicative of solid-state diffusion through a dense, adherent scale (see Figure 3.4a and Table 2.3.4). After breakaway for Ta and for all times in TaC, the linear recession rate suggests that oxidation is gas-phase diffusion limited

through large defects in the oxide, given the assumption that reaction rates are rapid (Table 2.3.2). Ta forms a cracked oxide post-breakaway, which aligns with this rate law. TaC, however, forms a porous oxide, so the transport mechanism that was expected was parabolic oxidation through a growing porous oxide (Table 2.3.3). It is suggested the large voids visible in Figure 3.5 are responsible for most of the oxygen transport and thus drive linear oxidation with respect to time in TaC. These experimental results for oxidation kinetics (Figure 3.11) showing slower oxidation kinetics for TaC than Ta do not align with pre-conceived mechanism assumptions which assumed that the porous scales formed on carbides would allow rapid oxygen ingress and thus more rapid oxidation than their counterpart metals.

The Maltese cross shape shown in Figures 3.4 and 3.5 forms on materials that have a large PBR, usually 2.0 or greater, because of lateral stresses which are created during oxide growth. The PBR for Ta is 2.5 and TaC is 2.0 and explains why the Maltese cross shape is more pronounced in the oxide on Ta compared to the oxide on TaC. However, despite the split corners creating fast oxidation paths to the underlying material, Maltese cross formation does not coincide with the onset of breakaway oxidation on Ta. The corners of both substrates are rounded significantly during oxidation, evident from Figures 3.4 and 3.5, and suggest that these split corners are also a site of rapid oxygen attack, but such attack is not significant enough to affect the bulk recession rate.

The Maltese cross stops forming at shorter times and higher temperatures for both Ta and TaC, showing that the oxide becomes more compliant at higher temperatures. The plasticity of the Ta metal substrate also likely alleviates some of the stresses created during growth. The oxide grown on TaC is highly porous and growth stresses in the oxide can be relieved by deforming the oxide at pores throughout the scale rather than concentrating at the oxide corners. Thus, less stress

relief is required to prevent corner oxide failure, and the Maltese cross formation is stopped at lower temperatures. Figure 3.5 shows that the Maltese cross structure stops forming on TaC at a lower temperature (1400°C) than observed in Ta (1500°C).

The same stresses which create the Maltese cross during growth also drive cracking in the oxide on Ta. These cracks are responsible for the breakaway oxidation shown in Figure 3.11. At 1300°C, scale cracking and breakaway oxidation occurs around 5 min exposure time. At 1400°C, because of the increased oxide compliance, cracking and breakaway oxidation are slightly delayed, with oxide cracking beginning around 5-6 min. Figure 3.6 shows large error bars in the cracking fraction of the oxides on Ta at 5 min, indicating some variation in cracking onset. The ToF-SIMS data in Figure 3.10 supports these findings, showing ^{18}O diffusion through a crack in the scale formed at 1300°C after 5 min, while no cracks are shown in the oxide grown at 1400°C. Instead, Figure 3.10 shows solid-state diffusion of ^{18}O through the oxide scale at 1400°C after 5 min, with no increased ^{18}O signal at the metal/oxide interface which would indicate rapid oxygen ingress. The fraction of cracks found in the oxide grown on Ta after 5 min correlates well with the oxidation rate, shown in Figure 3.13.

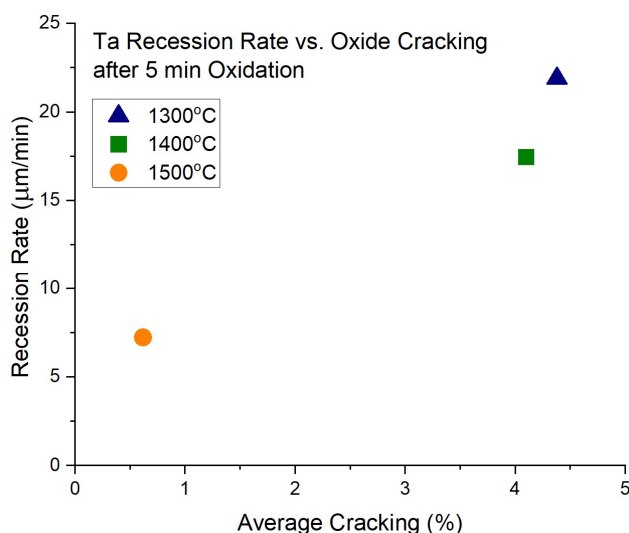


Figure 3.13: Correlation of Ta post-breakaway oxidation rate to average crack area fraction.

Kofstad studied Ta oxidation from 1000-1300°C from 0.01-100 torr P_{O_2} and observed breakaway behavior during oxidation at 1000-1050°C in 10-100 torr P_{O_2} [10]. The shape of the curve in Figure 3.12 is highly reminiscent of the curves presented in Kofstad's work (initial parabolic regime followed by an increased linear regime post-breakaway), suggesting that similar oxidation mechanisms may be at play, though they did not report oxidation kinetics at 1300°C and 7.6 torr P_{O_2} (1% O_2 S.T.P.). At higher temperatures, it was indicated that breakaway behavior was either delayed or not observed due to increased plasticity of the oxide. The time scales they studied are too coarse to see if breakaway oxidation occurred at <10 min and 1300°C in their data, though similar conclusions are seen here: onset of breakaway behavior occurs later in exposure at higher temperatures. The area fraction of voids, pores, and cracks found in the oxide both in cross section and in plan view also correlate well to the changes in oxide plasticity with temperature.

The reduced P_{O_2} experiments shown in Figure 3.12 demonstrate that the oxidation process slows with a reduced amount of oxygen in the environment. Because breakaway onset is related to the oxide cracking, the change in oxidation mechanism at the breakaway point at 10 min exposure time indicates that the oxidation rate is still dependent on the microstructure of the oxide at 1000 ppm P_{O_2} . Therefore, the assumption that the oxidation reaction rate is rapid relative to the oxygen transport rate through the scale is valid. These experiments also show that breakaway is delayed at lower P_{O_2} , indicating breakaway onset is likely dependent on scale thickness as well as temperature.

TaC shows significant evidence of preferential grain boundary attack during oxidation, as has been reported in the literature [28], [48]. As grain boundary oxidation progresses, oxide begins to form between carbide grains below the carbide/oxide interface. The volume increase which accompanies oxide formation dislodges the carbide grains from the bulk and results in the large

amount of unreacted carbide grains dispersed throughout the oxide. At 1300°C, very little grain boundary oxidation occurs, and much fewer carbide grains are found in the scale. As temperature increases, the degree of grain boundary oxidation increases, and more carbide grains can be found in the oxide scale for any given time at higher temperatures. At 1500°C, carbide grains are observed nearly all the way through the thickness of the scale. These carbide grains do not seem to impact the growth of the oxide scale in any way, though it could affect the mechanical properties of the scale. Additionally, the grain boundary oxidation likely undermines the mechanical integrity of the underlying carbide. No grain boundary oxidation is observed in Ta, so the unreacted metal in the scale is believed to be unrelated to grain boundary oxidation. Possibly, rapid diffusion down the cracked and highly columnar oxide results in oxygen bypassing the remnant metal in the scale on the way to the underlying bulk material. However, more investigation into this phenomenon is needed to verify the mechanism.

The changes in oxide grain size with temperature (Figure 3.9) show that some grain growth is occurring at all temperatures. Coupled with the decrease in surface porosity, these features are indicative of oxide sintering. The oxide on Ta forms large plate structures which grow significantly larger as temperature increases, up to an average size of $36.6 \pm 13.3 \mu\text{m}$ after 7 min at 1500°C. For TaC, oxide grain growth is limited by the formation of new pores due to CO(g) formation, and the maximum average grain size observed is $1.8 \pm 0.2 \mu\text{m}$ after 6.25 min oxidation at 1500°C. The smaller grains have an increased curvature and therefore a greater driving force for sintering, driving the highly rounded grain morphology shown in Figure 3.7 (right). In the oxide formed on TaC, the pores and large voids are always found throughout the oxide and the oxide does not become significantly more protective with increasing temperature. The oxidation rate of TaC does not change significantly from 1400°C to 1500°C, despite the measured increase in plan view

porosity of the oxide at 1500°C shown in Figure 3.8. The data suggests that increasing oxidation time leads to a decrease in surface porosity at 1300°C and 1400°C. Oxide sintering during growth closes the porosity in the oxide at these temperatures. In cross section, the oxides grown at 1500°C clearly have fewer fine pores in the oxide as compared to lower temperatures, inconsistent with the surface porosity data. Therefore, the origin of the increasing surface porosity in TaC at 1500°C is still unknown. However, the degree of sintering within the oxide is believed to be enough to slow oxidation at 1500°C slightly as compared to the oxidation rate at 1400°C. Fewer pores can be seen in Figure 3.5a than in Figure 3.5b-d, likely a result of this increased sintering.

iv. Conclusions

Oxidation studies of Ta and TaC have been conducted at 1300°C, 1400°C, and 1500°C in a 1%O₂ – Ar environment. Additional Ta oxidation was conducted at 1300°C in a 1000 ppm Po₂ environment. Several morphological and kinetic observations were made which were not explained by the traditional understanding of metal and carbide oxidation. Initial parabolic oxidation of Ta is governed by diffusion through the oxide scale. At longer times, the oxide cracks due to stresses created during growth and oxygen rapidly ingresses through these cracks in the scale, driving a linear oxide growth rate. Material consumption rates were shown to be lower for Ta than TaC pre-breakaway. After Ta breakaway oxidation starts, TaC recession rates are slower at all measured temperatures.

The oxide grown on Ta becomes more protective at higher temperatures, potentially preventing oxide cracking or splitting at the corners. The material consumption rate of Ta decreased with increasing temperature, while the consumption rate of TaC increased with

increasing temperature. Large voids appear to be the primary oxygen transport path through the oxide on TaC, respectively. The oxidation of the carbon in TaC forms a porous oxide with large voids making the oxide less protective. Despite oxide sintering, these pores are retained at high temperatures. The pore networks allow for more stress relief in the oxide scale, so Maltese cross formation on TaC is observed to stop at lower temperatures than seen for Ta oxidation.

Both Ta and TaC have melting points above 3000°C, which would make them excellent structural materials for inert ultra-high temperature applications. However, given the relatively low melting point of the grown oxide (1550°C for L₂, 1880°C for L₁) compared to other refractory oxides, neither Ta or TaC would make an excellent oxidation resistant material at such temperatures. Additionally, the high density of Ta and TaC makes them much less desirable in aerospace applications. At intermediate temperatures up to 1500°C, Ta could make an acceptable oxidation barrier if used prior to the breakaway oxidation point, as the oxide may not crack yet, and oxidation will be comparatively slow. In any condition where the oxide grown on Ta cracks, generally longer than 5 min, TaC would be preferred, as material recession is slower than oxidation through the cracked oxide on Ta.

- ii. Oxidation of Zr vs ZrC
 - a. Experimental Method

A sheet of 0.711mm (0.028 in) thick sheet of a commercially pure (CP) Zr alloy (Zr702, United Titanium, Inc., Wooster, OH) and a 3-inch ZrC puck produced by HIP (Kurt J. Lesker Company, Pittsburg, PA) were machined into RHS specimens in the same way as described for Ta and TaC. IGA analysis indicates that the carbide is highly stoichiometric (ZrC_x , $x=0.97$). Oxidation was carried out between 1300°C and 1800°C (100°C steps) in flowing 1% O_2 – Ar at 1 atm for up to 10 minutes, or until samples failed. Oxidation kinetics were measured at 1300°C, 1400°C, and 1600°C. Zr softened significantly at 1600°C such that the samples sagged and failed. After oxidation at 1300 and 1400°C, the oxides formed on ZrC samples would spall 3-5 minutes after cooldown. To successfully characterize samples in cross section with their oxides mostly intact, samples were put into a quick-cure epoxy (SamplKwick, Buehler, Lake Bluff, IL) to effectively “lock” the oxides in place. This was not an issue for Zr metal samples. Samples were characterized via SEM, TEM, EDS, XRD, and Raman Microscopy.

- b. Results

A chart describing the oxidation mechanisms observed during the oxidation of Zr is shown in Figure 3.14. Representative polished cross sections of the hot zone for each area of the diagram are also displayed in the figure, showing an example of each major oxidation mechanism observed as a function of the temperatures and times explored. Additional micrographs for all explored conditions can be found in Appendix A.

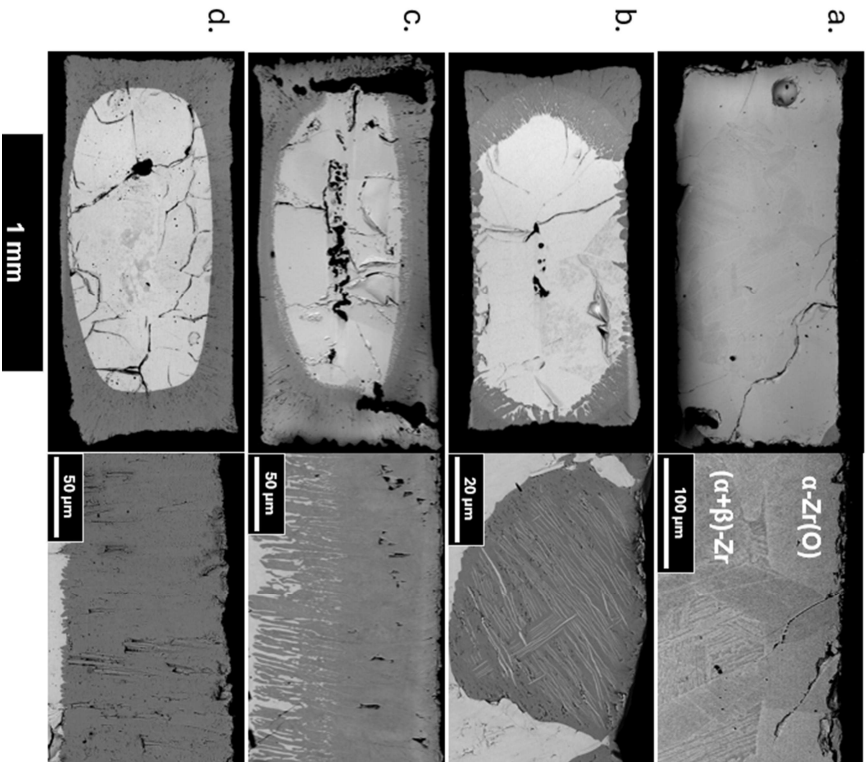
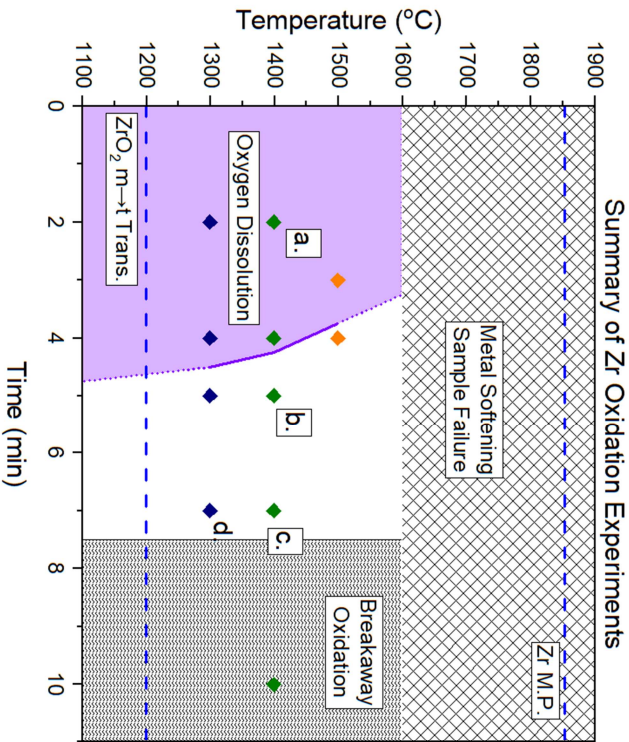


Figure 3.14: (Left) Chart summarizing the Zr oxidation experiments conducted and the identified relevant mechanisms to the oxidation rate. Data points marked with a letter refer to the micrographs shown on the right side. (Right) Micrographs of samples which are representative of each area shown on the graph. From top to bottom: (a) post-oxidation at 1400°C for 2 min, showing a Widmanstätten $\alpha+\beta$ Zr microstructure in the bulk Zr, but no oxide formation; (b) post-oxidation at 1400°C for 5 min, showing separate oxide island formation containing a $\alpha\text{-Zr(O)}+\text{ZrO}_2$ Widmanstätten microstructure; (c) post-oxidation at 1400°C for 7 min, showing both oxide cracking and a two-phase $\alpha\text{-Zr(O)}+\text{ZrO}_2$ finger-like microstructure; and (d) post-oxidation at 1300°C for 7 min, showing only a cracked oxide structure. Boundaries are drawn as straight lines between data points and do not represent explicit data measurements.

At very short oxidation times, no oxide scale is formed on Zr. A Widmanstätten microstructure of $\alpha+\beta$ Zr [50], [51] is apparent in the center of the bulk Zr, shown in greater detail in Figure 3.14a. A single-phase layer of α -Zr stabilized by oxygen was found near the metal/gas interface, referred to going forward as α -Zr(O). As time progressed, the $\alpha+\beta$ Zr region became smaller until the entirety of the remaining bulk was comprised of α -Zr(O). ZrO₂ growth began much later into oxidation, starting at the corners of the sample, followed by the short edges, and finally the long edges. This progression is consistent with the Zr-O phase diagram (Figure 2.1). For this work, the long edges are of primary interest because they more closely represent bulk material. Oxide growth on these edges began after around 3-5 minutes of oxygen exposure, starting earlier with higher temperature. Oxide growth started with the formation of small islands of oxide, shown in Figure 3.14b, which coalesced into a continuous oxide scale as oxidation proceeded. XRD indicated that the oxides that grew on Zr are only comprised of the monoclinic m-ZrO₂ structure post-oxidation. An example XRD pattern is shown in Figure 3.15.

Two microstructures are observed in the grown oxides, shown in greater detail in Figure 3.16. The first is a highly cracked oxide. The second is a two-phase oxide comprised of α -

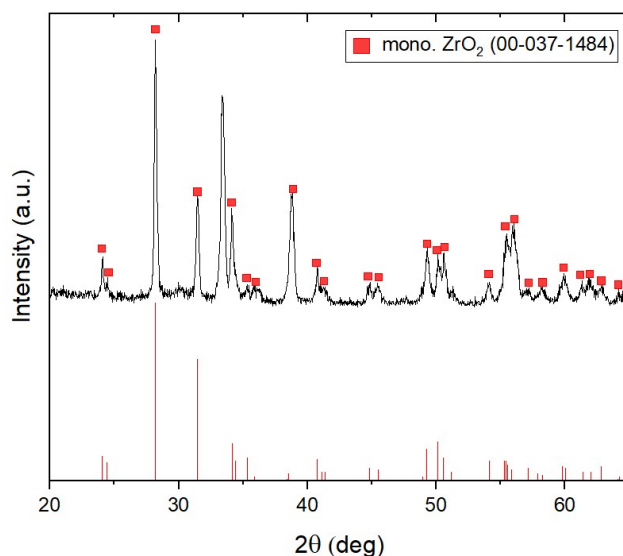


Figure 3.15: XRD pattern of Zr after 5 min oxidation at 1400°C

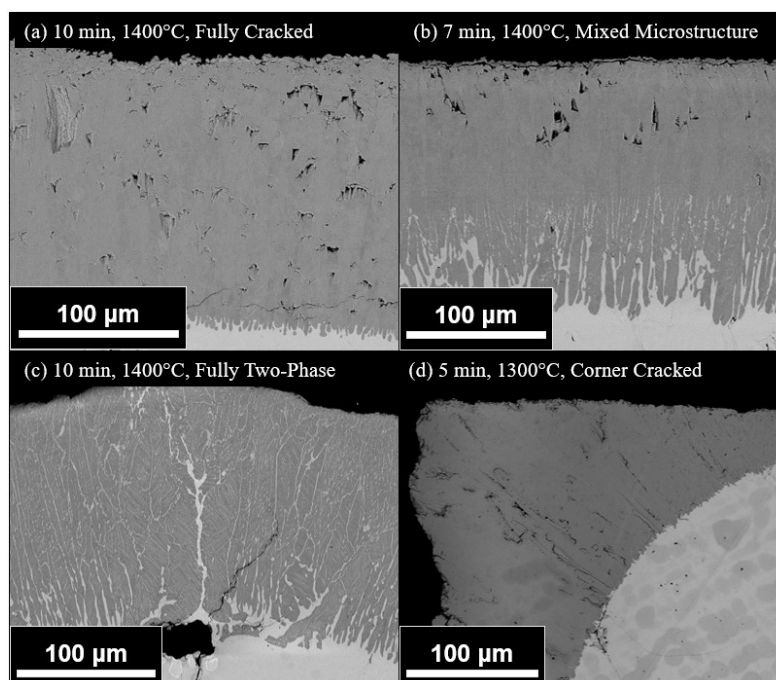


Figure 3.16: Polished cross section backscatter micrographs of oxidized Zr after (a-c) 7-10 min at 1400°C and (d) 5 min at 1300°C in 1%O₂-Ar. Varying degrees of cracking and/or two-phase oxide are present.

Zr(O)+ZrO₂. At the metal oxide interface, this two-phase region has a finger-like morphology normal to the interface, visible in Figure 3.16b-d. Within the oxide itself, a Widmanstätten-like morphology can be seen, with α -Zr(O) having a needle-like morphology within the ZrO₂, as shown in Figure 3.14b and 3.16c. The oxide can also contain both microstructures simultaneously, being partially cracked and partially two-phase, as shown in Figure 3.16b. The two-phase oxide was not observed in the oxide at 1300°C, but was observed to occur at all times after oxidation at 1400°C. The oxide islands formed at initial oxide growth always exhibit a two-phase microstructure.

The oxides grown on Zr were found to be mostly well-adherent. Sometimes, the oxide delaminated from the underlying metal, leaving large voids in the oxide scale, visible in Figure 3.14c as the large black areas near the sample corners. The corners of the oxides do not split to form a Maltese cross. When the oxide is entirely two-phase, the oxide sometimes appears to bulge outward and exhibits a rumpled morphology when observed in plan view (Figure 3.17).

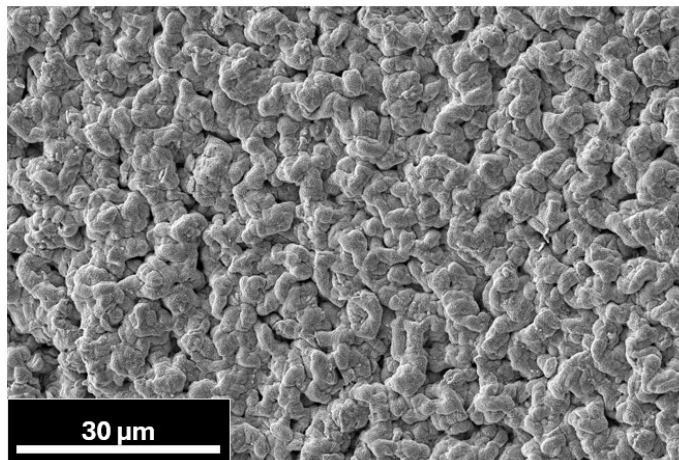


Figure 3.17: Plan view secondary electron micrograph of the rumpled surface of an oxide grown after 5 min of oxidation at 1400°C on Zr in 1% O₂ – Ar.

Another chart describing the oxidation mechanisms observed during the oxidation of ZrC is shown in Figure 3.18. Representative polished cross sections of the hot zone for each area of the diagram are also displayed in the figure, showing an example of each major oxidation mechanism observed as a function of the temperatures and times explored. Additional micrographs for all explored conditions can be found in Appendix A.

The oxides grown on ZrC show varying structures. Oxide spallation occurred post-oxidation at 1400°C and below, shown in Figure 3.18c and 3.18d. The oxides spalled and fell apart several minutes after being removed from the RHS. Still images taken throughout this spontaneous spallation process are shown in Figure 3.19. Micrographs of the samples which exhibited spallation were captured by putting the samples into a quick-curing epoxy very quickly after the experiment ended. The oxide still separated from the carbide while in epoxy and a significant gap is visible at the carbide/oxide interface due to the poor oxide adherence, shown in Figure 3.18c and 3.18d. The gap fills with epoxy during the curing process. At 1500°C and above, the oxide became much

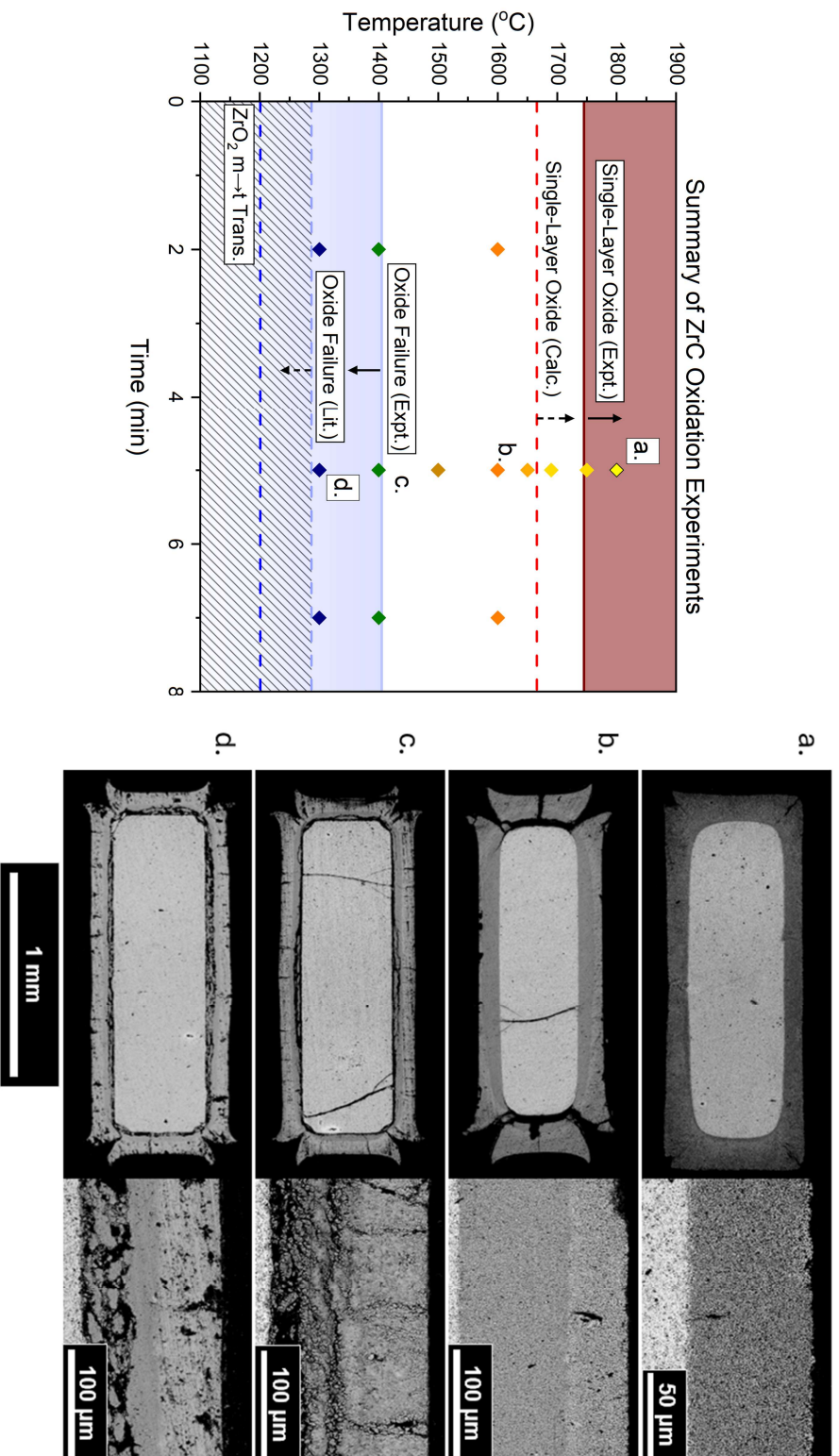


Figure 3.18: (Left) Chart summarizing the ZrC oxidation experiments conducted and the identified relevant mechanisms to the oxidation rate. Data points marked with a letter refer to the micrographs shown on the right side. (Right) Micrographs of samples which are representative of each area shown on the graph. From top to bottom: (a) post-oxidation at 1800°C for 5 min, showing very slight Maltese cross formation and only a single-layered oxide; (b) post-oxidation at 1600°C for 5 min, showing Maltese cross formation and a mostly adherent two-layered oxide; (c) post-oxidation at 1400°C for 5 min, and catastrophic failure of the two-layered oxide; and (d) post-oxidation at 1300°C for 5 min, showing Maltese cross formation and catastrophic failure of the two-layered oxide. Boundaries are drawn as straight lines between data points and do not represent explicit data measurements.



Figure 3.19: Time sequence of macro photos showing the spontaneous breakdown of the oxide scale formed on a single ZrC sample oxidized at 1400°C for 5 min in 1% O₂ – Ar. From left to right, the pictures show the sample 1 min, 3 min, and 5 min after being removed from the RHS.

more adherent, shown in Figure 3.18a and b. Maltese cross formation is observed after oxidation at all temperatures, but is less distinct after oxidation at 1800°C, shown in Figure 3.18a.

A two-layer oxide was formed on ZrC below 1750°C. The outer layer is carbon-free ZrO₂ and is very porous with well-defined oxide grains, shown in Figure 3.20a. At conditions where catastrophic oxide failure occurs, this layer contains many vertical cracks which stop abruptly at the inner layer boundary, seen in Figures 3.18c and 3.18d. The inner layer is carbon-rich ZrO₂ and, when adherent, it has a denser morphology, shown in Figure 3.20b. Inspection of the inner layer at higher resolution via TEM/EDS shows that the carbon in the inner layer takes the form of nano-sized channels interspersed throughout the ZrO₂, shown in Figure 3.20d. The carbon channels are well aligned perpendicular to the carbide/oxide interface. SAED was used to probe the crystal structure of the oxide formed at the carbide/oxide interface and identified both m-ZrO₂ and ZrC very close to the interface, shown in Figure 3.20f. Further into the oxide scale, only m-ZrO₂ is identified, shown in Figure 3.20g.

Raman microscopy (514.5 nm laser, 50x objective lens, numerical aperture of 0.5) was used to investigate the form and crystallinity of the carbon. An example Raman spectrum is shown in Figure 3.21. The carbon is highly ordered graphite, showing a D/G ratio of between 0.6 and 0.4. The graphite becomes slightly less disordered (lower D/G ratio) further from the carbide/oxide

interface, Figure 3.21 (right). HRTEM of one of the carbon channels is shown in Figure 3.22, plainly showing the ordered graphite aligned parallel to the channel direction, perpendicular to the carbide/oxide interface.

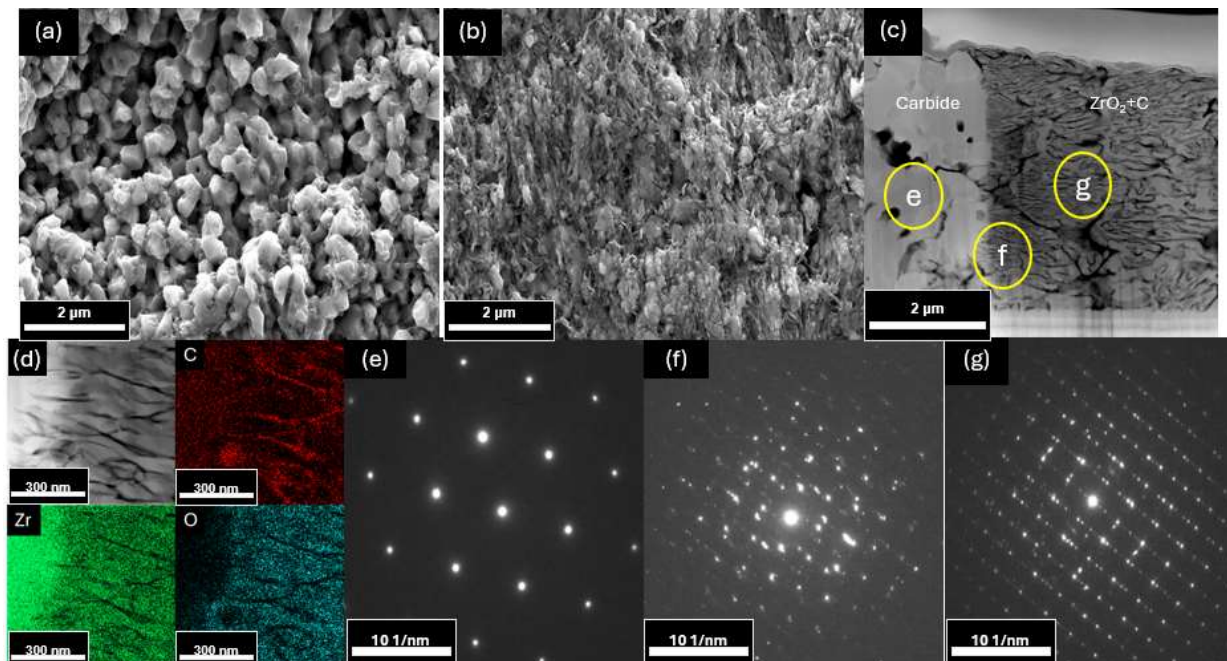


Figure 3.20: High resolution SEM/TEM on ZrC oxidized for 7 min at 1600°C in 1% O₂ – Ar; (a) and (b) are secondary electron images of the outer and inner oxide layers, respectively; (c) TEM micrograph of a FIB liftout from across the ZrC/inner oxide layer boundary; (d) TEM/EDS of the inner oxide layer; (e-g) SAED patterns from (e) the bulk ZrC, (f) oxide very near the carbide/oxide interface (indexed as m-ZrO₂ and ZrC), and (g) the oxide further into the scale (indexed as m-ZrO₂). TEM/EDS and SAED thanks to H. Heinrich.

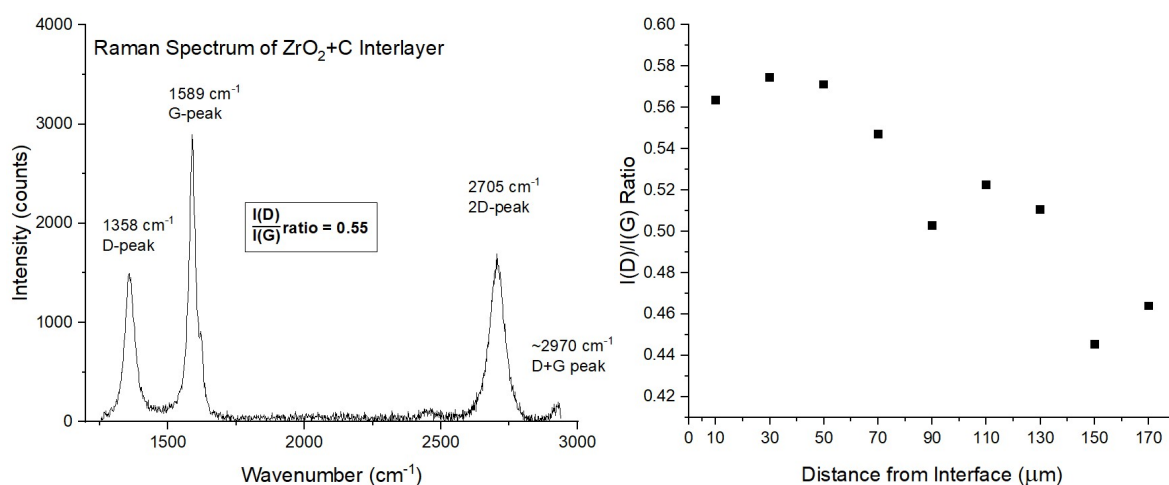


Figure 3.21: (Left) A Raman spectrum from the inner ZrO₂+C layer grown on ZrC after 5 min oxidation at 1600°C and the ratio of the D and G peaks as a function of distance from the carbide interface. Raman courtesy of J. Thompson.

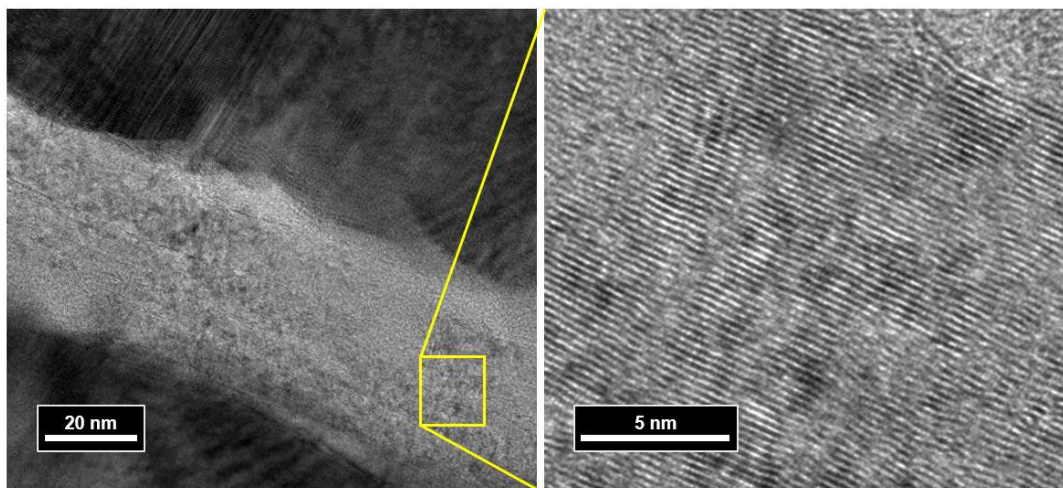


Figure 3.22: HRTEM of a carbon channel near the carbide/oxide interface on ZrC oxidized at 1600°C. TEM courtesy of H. Heinrich.

The oxidation rates measured via material recession are reported in Figure 3.23 and Figure 3.24. Oxidation rates were not measured for Zr above 1500°C because the material softened and sagged during experiments, resulting in failure. Material recession kinetics were found to be parabolic for Zr (prior to breakaway) and linear for ZrC. Zr showed negative recession at early times, indicating a swelling of the bulk metal. At 10 min oxidation, the recession rate jumped significantly.

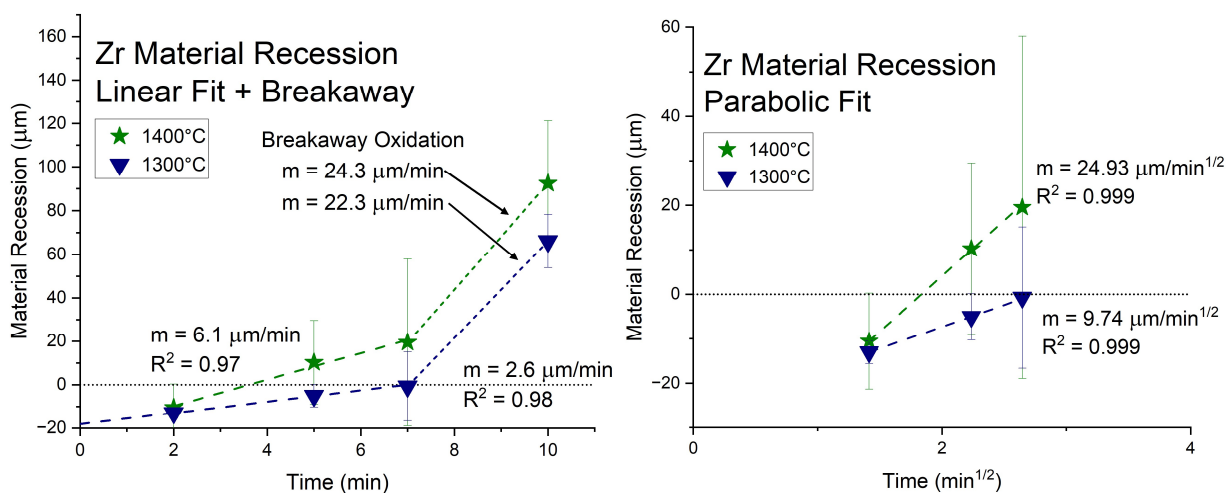


Figure 3.23: Comparison of the oxidation kinetics for Zr at 1300°C and 1400°C plotted versus linear time. The pre-breakaway recession is plotted versus parabolic time to show the change in mechanism at breakaway oxidation onset.

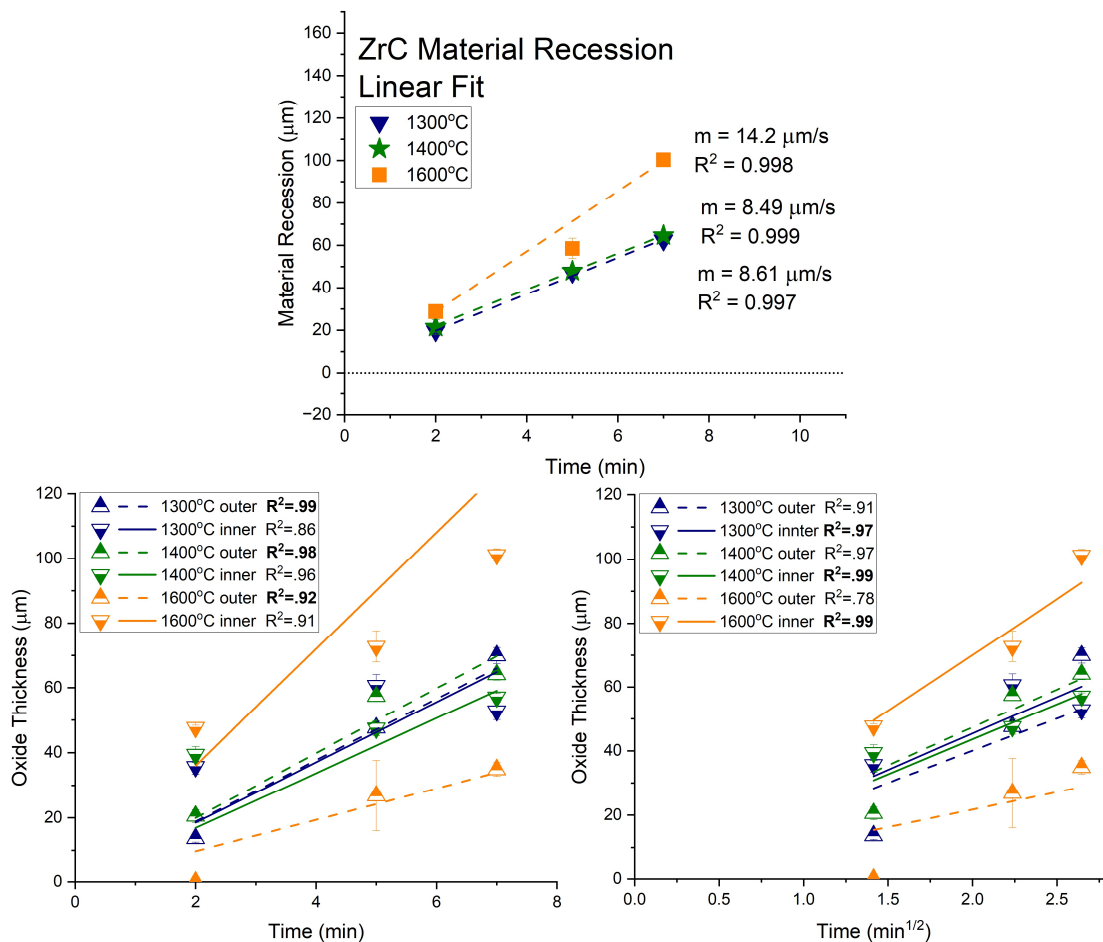


Figure 3.24: (Top) Recession kinetics of ZrC and comparison between (bottom left) linear and (bottom right) parabolic fits for the growth kinetics of the inner and outer ZrO_2 layers formed on ZrC from 1300-1600°C in 1% O_2 -Ar. Bolded R^2 values indicate the highest value between the rate laws. Rate law fits constrained through the origin to represent no delay in initial oxide growth.

For ZrC, the growth rates of both oxide layers were also measured independently and plotted versus both linear and parabolic time, shown in Figure 3.24. Data was fit versus a linear trendline and the R^2 values of each fit are listed. While the growth rate of the oxide layers could be fit to several rate laws with R^2 fits greater than 0.95, the prevailing growth rate was assumed to be the fit with the highest R^2 value. By this assumption, the inner layer growth rate correlated most strongly to parabolic kinetics at all temperatures and the outer layer correlated strongly to a linear growth rate at all temperatures.

Pore size and density of the porous oxide layer formed on samples exposed to 1600°C and

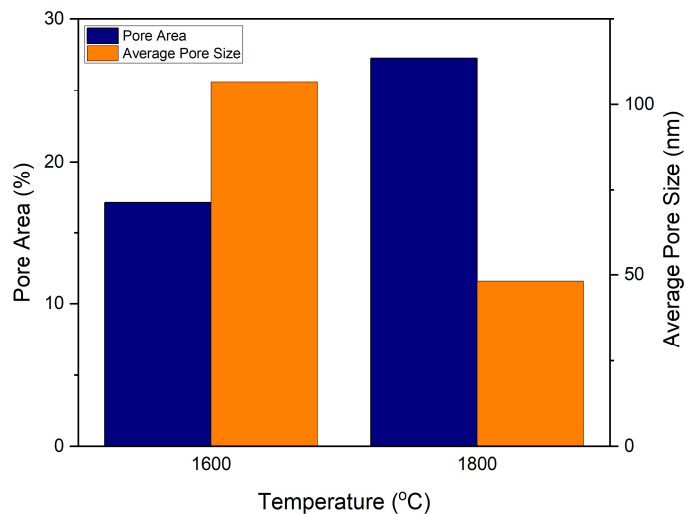


Figure 3.25: Oxide pore size analysis between ZrC samples oxidized at 1600°C and 1800°C for 5 min. The navy columns indicate pore area fraction (left y-axis) and the orange columns indicate average pore size (right y-axis).

1800°C were measured using the “Analyze Particles” function in ImageJ [101], and the results are shown in Figure 3.25. Particles identified smaller than 10nm were removed as noise, as this is smaller than the per pixel resolution of the images used. A reduction in pore size throughout the oxide scale is found when temperature increases from 1600°C to 1800°C.

c. Discussion of Results

During the early stages of Zr oxidation, oxygen is dissolving into the metal, delaying external oxide scale growth (Table 2.3.12), as seen in Figure 3.14a. The lattice parameters of Zr increase as oxygen content increases towards the solvus (Figure 2.1) [13], [102], resulting in the swelling observed during early oxidation. Other researchers have observed the formation of a Widmanstätten ($\alpha+\beta$) microstructure upon quenching Zr from the $\alpha+\beta$ stability region [50], [51]. The oxygen concentration at the boundary between the $\alpha+\beta$ Zr and α -Zr(O), shown in Figure 3.14a, can be identified using the Zr-O phase diagram (Figure 2.1). The diffusion rate of oxygen in Zr

metal was estimated using the thickness of the α -Zr(O) region via a simplified form of a solution to Fick's 2nd law assuming a semi-infinite system, the nominal diffusion distance equation:

$$x = \sqrt{Dt} \quad (3.1)$$

where x is the layer thickness, D is the diffusivity, and t is the time. Some calculated diffusivity values are shown in Table 3.1. These values are slightly greater than, but within one order-of-magnitude of, literature values for oxygen diffusivity in α -Zircaloy alloys, which contain alloying components that will slightly reduce the oxidation rate (Zircaloy-2: Zr-1.5%Sn- 0.15%Fe-0.1%Cr-0.05%Ni) [52], [63].

Table 3.1: Diffusivity of oxygen in α -Zr calculated from equation (3.1). Values compared to oxygen diffusivity in α -Zircaloy 2 from [52].

T (°C)	D (cm²/s) Measured	D (cm²/s) Literature
1500	4.7E-06	1.7E-06
1400	3.3E-06	8.6E-07
1300	2.1E-06	3.9E-07

After the surface of the Zr metal is saturated with oxygen, oxide growth occurs rapidly. Oxide growth starts at the corners of the specimen where oxygen is able to saturate the metal bidirectionally. The parabolic recession rates for Zr suggest solid-state diffusion-controlled oxygen transport in ZrO₂, as grain boundary oxidation is not observed and the oxide is not porous (Table 2.3.2). The oxidation rate follows a parabolic growth rate until after 7 minutes of oxidation, where onset of breakaway oxidation occurs. The oxides reported in literature which form on CP Zr are only a single layer ZrO₂. However, a two-phase α -Zr(O)+ZrO₂ oxide is thermodynamically stable according to the phase diagram (Figure 2.1) and is found here at the metal/oxide interface. This two-phase microstructure has only been observed to form upon quenching during oxidation [103] despite being stable. Thermally grown two-phase α -Zr(O)+ZrO₂ is not well documented in

literature [55] and its effect on the oxygen transport mechanism has not been identified. Its presence here is likely related to the rapid cooldown used to end the oxidation experiments. The presence of only m-ZrO₂ after rapid quench also indicates that the oxide undergoes rapid polymorphic phase change back to the monoclinic phase occurs on cooling, as the t-ZrO₂ phase is the thermodynamically stable phase at the exposure temperatures.

The oxide on Zr is under compressive stress created during growth, evident by the relief of such stresses via oxide rumpling and delamination [104], [105], [106]. Additional stresses created during volume expansion are likely relieved through the deformation of the underlying Zr, shown by the misshapen and cracked bulk visible in all examples in Figure 3.14. The oxide does not form a Maltese cross morphology, likely because the corners of the Zr oxidizes first and can freely grow without splitting.

The PBR of Zr is 1.54 which, by conventional understanding, would suggest the oxide will generally be protective and not likely to crack. However, breakaway oxidation is a well-recognized phenomenon in Zr oxidation [70], [107]. An in-depth analysis of oxide growth stresses at 900°C conducted by El Kadiri et al. showed that the stress sign changes from compressive to tensile at a critical oxide thickness, at which point the oxide cracks [69]. The oxide cracking allows for more rapid oxygen ingress via gas diffusion, leading to the breakaway oxidation behavior. When the oxidation rate is compared between samples which have cracked and those which have not, the samples which exhibit cracking show a higher rate of material recession, indicating a microstructural dependence on the oxidation rate, shown in Figure 3.26. This agrees with literature explanations of Zr breakaway oxidation at lower temperatures and helps explain the large error bars at longer oxidation times in Figure 3.23. This also indicates that the interface between the two-phase oxide region and the cracked oxide is very likely near the region where stresses in the

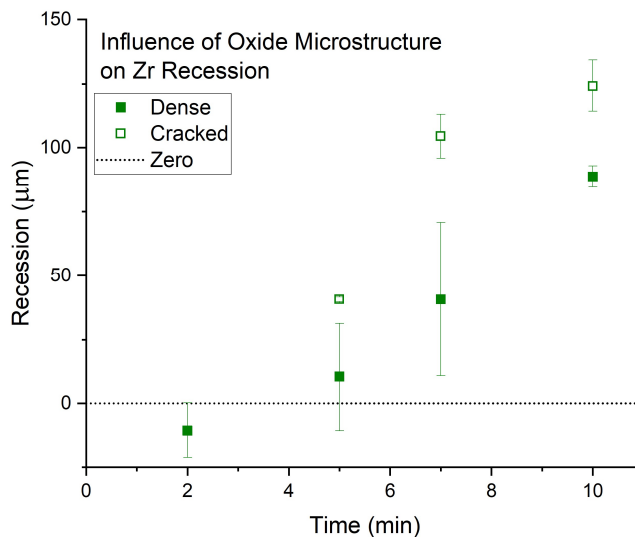


Figure 3.26: Recession rate of Zr at 1400°C in 1% O₂, grouped by dominant oxide microstructure. The data point at 2 min oxidation has not grown any oxide, so there is no difference in microstructure and the data points overlap. Error bars represent one standard deviation.

oxide switch from compressive to tensile. The time to breakaway onset has been reported to decrease at a decreasing rate with increasing temperature [107]. Apparently, the change in time to breakaway onset between 1300°C and 1400°C is minimal. Interestingly, cracking is found at all times at 1300°C (Figure 3.14d), but breakaway behavior is still observed after 7 min.

The oxides grown on ZrC show very different stress behavior than those grown on Zr. As previously suggested for the oxide grown on TaC, a porous oxide will not show the same cracking behavior as a dense scale because the pores will accommodate some of the stress in the oxide. In contrast to that result, the data here show that Maltese cross formation only occurs for the porous oxide on ZrC and not for the dense oxide on Zr. Because of the low oxygen solubility in ZrC, oxide growth initiates uniformly around the ZrC rather than just at the corners like Zr. The corner oxides are confined by the bulk oxide and will split to continue growing. Additionally, the ZrC is significantly less compliant than the Zr, and will not relieve as much of the oxide growth stresses at the carbide/oxide interface. Vertical cracking in the outer oxide layer on ZrC suggests the oxide

is under tensile stress during oxide growth. This tensile force is due to unconstrained growth at the oxide/gas interface.

The spontaneous spallation of the oxide scale on ZrC is found here to occur at 1400°C and below, slightly above the literature reported range of 853-1307°C [16]. Several studies suggested that intergranular stresses created by oxidation at ZrC grain boundaries is responsible for the spontaneous material failure [16]. However, no evident grain boundary oxidation was identified in ZrC in any experiments conducted for this work (Figure 3.20c).

Wei et al. proposed the volume change on transformation through the t/m-ZrO₂ transformation caused spallation of their oxides above 1000°C. The t-ZrO₂ polymorph is thermodynamically stable at all the temperatures investigated here. While t- and c-ZrO₂ are frequently reported for intermediate temperature oxidation of ZrC [17], [18], [19], [20], neither polymorph was identified at 1600°C. Size-driven stabilization of the high temperature oxide polymorphs have been reported as the origin of t- or c-ZrO₂ present below their transformation temperatures [82], [108]. It is possible that the higher oxidation temperatures ($\geq 1500^\circ\text{C}$) could cause increased ZrO₂ growth at this interface, causing the higher temperature polymorphs to no longer be stable at room temperature. Measurements near the carbide interface (Figure 3.20c) yield an average oxide crystallite size of 39 ± 10 nm, which is above the maximum size for t-ZrO₂ size-stabilization (~ 30 nm [108]). Shimada also reported a sharp increase in the intensity of the m-ZrO₂ peaks and decrease in the intensity of t/c-ZrO₂ peaks found in the ZrC oxidation products as temperature approached 1500°C [44], matching this hypothesis as well as the temperature where spallation stops occurring. Unfortunately, due to the catastrophic failure of the interfaces at 1300-1400°C, no crystallographic data could be collected from the interface prior to failure. The connection between the phase transformation in the oxide and the spontaneous scale spallation

cannot be confirmed with the available data, but fits with observations and seems a plausible explanation for the cessation of oxidation spallation at 1500°C. More crystallographic data regarding the polymorphic transformations in the oxide that occur during ZrC oxidation is needed to verify this hypothesis.

The oxide growth kinetics on ZrC is considered next. The overall linear oxidation rate for ZrC suggests gas-phase diffusion via the pores and cracks in the oxide (Table 2.3.2) is the dominant oxygen transport mechanism. These findings agree with literature reported rates [20]. The growth rate laws of the separate oxide layers which formed on ZrC also followed literature reports: a linear growth rate of the outer layer and a parabolic growth rate of the inner layer [20], [21]. A linear growth rate, assuming reaction rates are rapid relative to oxygen transport, is indicative of gas-phase diffusion through a porous or cracked oxide (Table 2.3.2), consistent with the oxide scale morphology shown in Figure 3.20a. A parabolic growth rate is indicative of either solid-state diffusion (Table 2.3.4) or gas-phase diffusion through a growing porous oxide (Table 2.3.3).

Several authors have shown that for ZrC oxidation between 800-1100°C, the parabolic growth rate of the inner oxide layer is due to competing oxide growth at the carbide/oxide interface and carbon removal by CO(g) at the inner/outer oxide interface [19], [20], [44], [71]. Gasparri et al. observed the inner layer reached a limiting thickness of approximately 20 μm during oxidation at 800°C. This is far smaller than the thicknesses observed here (60-100 μm after 7 min), implying significantly greater oxygen diffusion rates through the inner layer. Additionally, the inner layer is reported here to be thicker than the outer layer, which seems contradictory to the parabolic growth rate observed. The error in the data presented here is large and, therefore, may not accurately identify the kinetic rate laws for the inner layer. Because of the relatively few data points collected in this study, a t-table indicates the slopes of these lines can be varied by factor of

2.8 and still remain within a 95% confidence interval. Thus, while the observed rate laws are believed to follow literature trends, more oxidation data at temperatures at 1500°C and higher is needed to accurately characterize the oxide layer growth kinetics. For this work, because of the observed parabolic oxide growth kinetics for the inner oxide layer, oxygen diffusion through the carbon-containing inner layer is assumed to be the rate-limited step.

Above 1750°C, only a single-layered oxide scale was observed on ZrC. Ellingham-type calculations of the Zr-C-O system conducted using data from the FactSage “FactPS” database [109] are shown in Figure 3.27. These calculations show that the formation of free carbon during oxidation is favored up to 1659°C, at which point $\text{ZrO}_2 + \text{CO}(\text{g})$ becomes the dominant reaction.

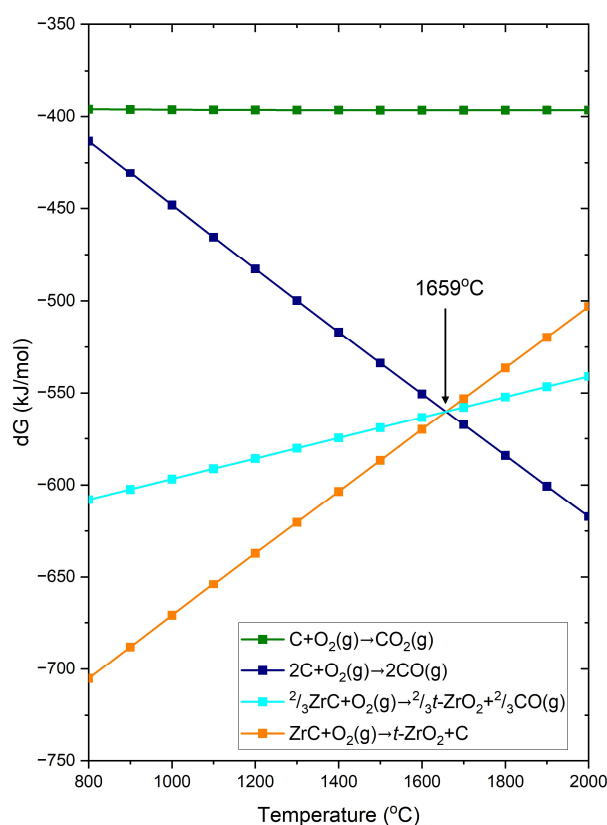


Figure 3.27: The ZrC Ellingham diagram. Free carbon is no longer predicted to be the most stable C-containing reaction product above 1659°C; instead, $\text{CO}(\text{g})$ becomes most stable. Experiments just above this temperature do not align with these calculations. Experiments at 1750°C show that favored $\text{CO}(\text{g})$ formation results in a single-layered oxide scale.

Here it is observed that at lower temperatures, Zr is preferentially oxidized from ZrC at the carbide/oxide interface to form ZrO_2+C . TEM/EDS (Figure 3.20d) and Raman microscopy (Figure 3.21) confirmed the formation of free carbon during oxidation at 1600°C . The D/G peak ratio from the Raman spectroscopy indicates this carbon is highly graphitic, becoming slightly more disordered with distance from the carbide/oxide interface [110]. Figure 3.18a shows the retention of free carbon in the scale above the calculated thermodynamic limit, as high as 1690°C . Given temperature gradients through the oxide scale in RHS samples [100], potential errors in emissivity readings, and the uncertainty in the thermodynamic data, the accuracy of the sample temperature readings in the RHS is not high enough to sufficiently probe this temperature to an accuracy of less than $\pm 50^\circ\text{C}$.

The oxidation results (Figure 3.23 and 3.24) indicate that oxidation of ZrC is more rapid than the oxidation of Zr pre-breakaway. At early times, the porous oxide formed on ZrC allows for more rapid oxygen ingress towards the underlying bulk material. Once the oxide on Zr cracks and breakaway oxidation occurs, Zr oxidation becomes significantly more rapid. At temperatures where the oxide on ZrC is a single-layered scale, initial recession measurements showed $50\pm 1.9\ \mu\text{m}$ of ZrC recession after 5 min at 1800°C yielded compared to $58\pm 4.7\ \mu\text{m}$ of recession after 5 min at 1600°C . This decrease in recession at higher temperatures occurs despite the loss of the dense, oxygen-diffusion limiting inner oxide layer. Figure 3.25 shows a decrease in the average pore size in the outer scale. This may imply that simultaneously with the loss of the carbon-containing layer, the pore size shrinks such that parabolic diffusion through growing porous scale becomes the rate limiting step. No confirmation of this mechanism can be made at this time other than that recession of the bulk ZrC is lower at 1800°C than at 1600°C .

d. Conclusions

The oxidation of Zr and ZrC have been conducted between 1300°C and 1800°C in a 1% O₂-Ar environment. From the studies conducted, there are several roles in which carbon affects the oxidation of Zr and ZrC. During early exposure, Zr metal's high solubility for oxygen delays the onset of scale and creates compressive stresses in the oxide during growth. ZrC has a much lower solubility for oxygen and so oxide formation starts promptly with the introduction of oxygen. During the dissolution phase, Zr metal recession is slower than ZrC recession. Upon oxide growth, the oxide formed on Zr is dense, while the oxide formed on ZrC is porous due to CO(g) evolution.

The dense oxide formed on Zr led to compressive stresses in the oxide and eventually led to breakaway oxidation. After breakaway onset, the oxidation rate of Zr becomes much faster than for ZrC. On ZrC, an inner layer of ZrO₂+C is observed to act as a diffusion barrier to oxygen and is likely responsible for maintaining the slower rate of ZrC recession. Above 1750°C, the carbon in the inner layer is no longer thermodynamically favorable and a single-layer porous oxide scale is formed. Despite the loss of the suspected diffusion barrier, recession rates decreased when the inner layer was lost. A decrease in oxide pore size due is suspected to be responsible, but more kinetic data is needed to determine the transport mechanisms with greater certainty.

For ZrC, oxide spallation occurs after oxidation at 1300-1400°C, but stops at and above 1500°C. This is believed to be due to ZrO₂ grain-growth driven retention of the higher temperature polymorphs of ZrO₂ at room temperature, which matches the data presented, though more conclusive evidence is needed to verify this hypothesis. From 1300-1600°C, the recession rate of ZrC increases as temperature increases. The porous oxide scale which grows in tension cracks due to rapid initial oxide formation and a much higher stiffness of the underlying ZrC. At temperatures

lower than 1500°C, this tension creates large cracks in the scale, but this stress is relieved at higher temperatures.

At 1800°C, the free-carbon-rich inner oxide layer is no longer stable and reacts to form CO(g) such that a single-layered, porous ZrO₂ scale is formed. However, a reduction in pore volume at 1800°C relative to that observed at temperatures between 1300 and 1600°C decreases the overall oxidation rate, despite the lack of a dense inner oxide layer, suggesting a change in the oxygen transport mechanism. Detailed study of oxygen diffusion pathways through the scale are needed to verify these mechanisms.

For any application longer than 10 minutes, ZrC is the preferred material for oxidation resistance because the breakaway behavior exhibited by Zr will drive rapid recession of the underlying material; however, ZrC must be heated to a minimum of 1500°C, or catastrophic oxide failure will occur. Additionally, the low melting point of Zr (1855°C) must be considered.

- i. Oxidation of Hf vs HfC
 - a. Experimental Method

A sheet of 0.635mm (0.020 in.) thick Hf (99.5% pure, metals basis) was sectioned into RHS specimens via electrical discharge machining (EDM; Exothermics, Inc., Amherst, NH, USA). EDM samples were lightly ground with P1200 SiC foils to remove residue from the machining process. Three-inch HfC pucks produced by hot isostatic pressing (HIP; Kurt J. Lesker Company, Pittsburg, PA) were diamond machined (Bomas Machining Specialties, Inc., Woburn, MA) into the dogbone geometry of 0.5mm (0.020 in) thick. IGA determined the HfC to be highly stoichiometric HfC_{0.991}. Oxidation of HfC was conducted at 1600, 1700, and 1800°C in flowing 1% O₂ – Ar at 1 atm for up to 11 min, or until sample failure. Many of the HfC samples did not survive the oxidation experiments to the desired exposure time. Oxidation of Hf was conducted only at 1600°C in flowing 1% O₂ – Ar at 1 atm for up to 10 minutes, or until samples failed. Sample softening and sagging was an issue above 1600°C. The samples which survived were mounted in epoxy and polished, then examined via SEM and TEM/EDS. Micrographs were measured and analyzed using ImageJ [101].

- b. Results

Figure 3.28 shows a backscatter SEM cross section from Hf after 5 min of oxidation at 1600°C. The microstructures formed are similar to those previously observed in Zr oxidation (see Figure 3.14b-d). At very short oxidation times, no oxide scale is formed on Hf. No Widmanstätten microstructure is visible in the bulk Hf, even at 2 min of oxidation time. This is consistent with the phase diagram (Figure 2.3) in which β-Hf is only stable above 1743°C. HfO₂ growth began much later into oxidation, starting at the corners of the sample, followed by the short edges, and finally

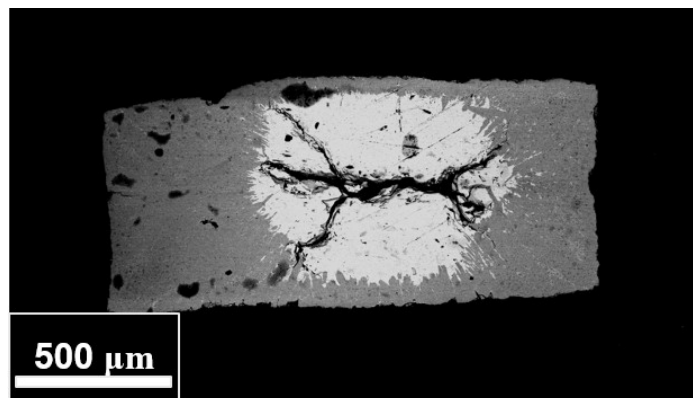


Figure 3.28: Backscatter cross section micrographs of Hf after 7 min of oxidation at 1600°C in 1% O₂ - Ar. The growth oxide and the remaining metal are highly reminiscent of Zr oxidation.

the long edges. For this work, the long edges are of primary interest because they more closely represent bulk material. Oxide growth on the corners began around 2 min of oxygen exposure, while oxide growth on the long edges began just before around 5 minutes of oxygen exposure.

Upon growth, the oxide forms one of two different microstructures: a highly cracked oxide and/or a two-phase layer of α -Hf+ZrO₂. The two-phase layer is primarily HfO₂ with thin, acicular α -Hf needles shown in Figure 3.29a. At the metal/oxide interface, a finger-like two-phase morphology can also be observed, Figure 3.29b. The presence of the two-phase layer is consistent

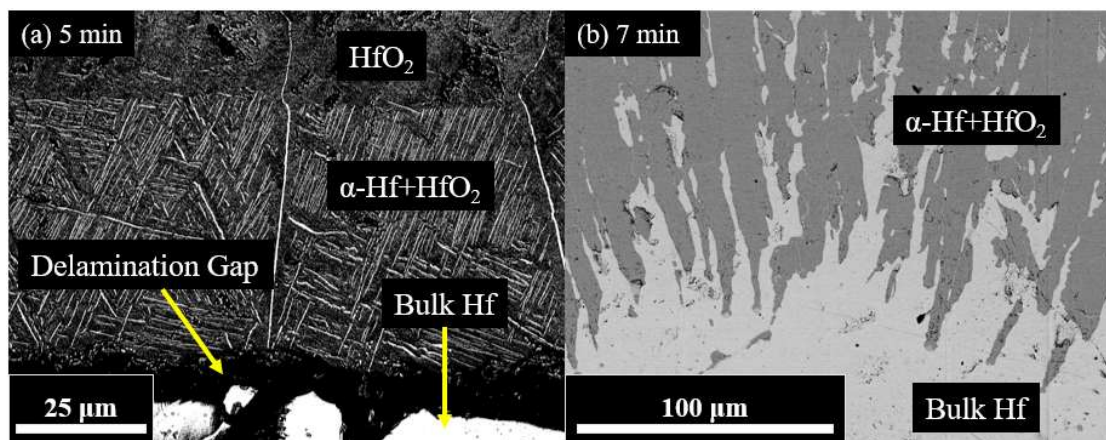


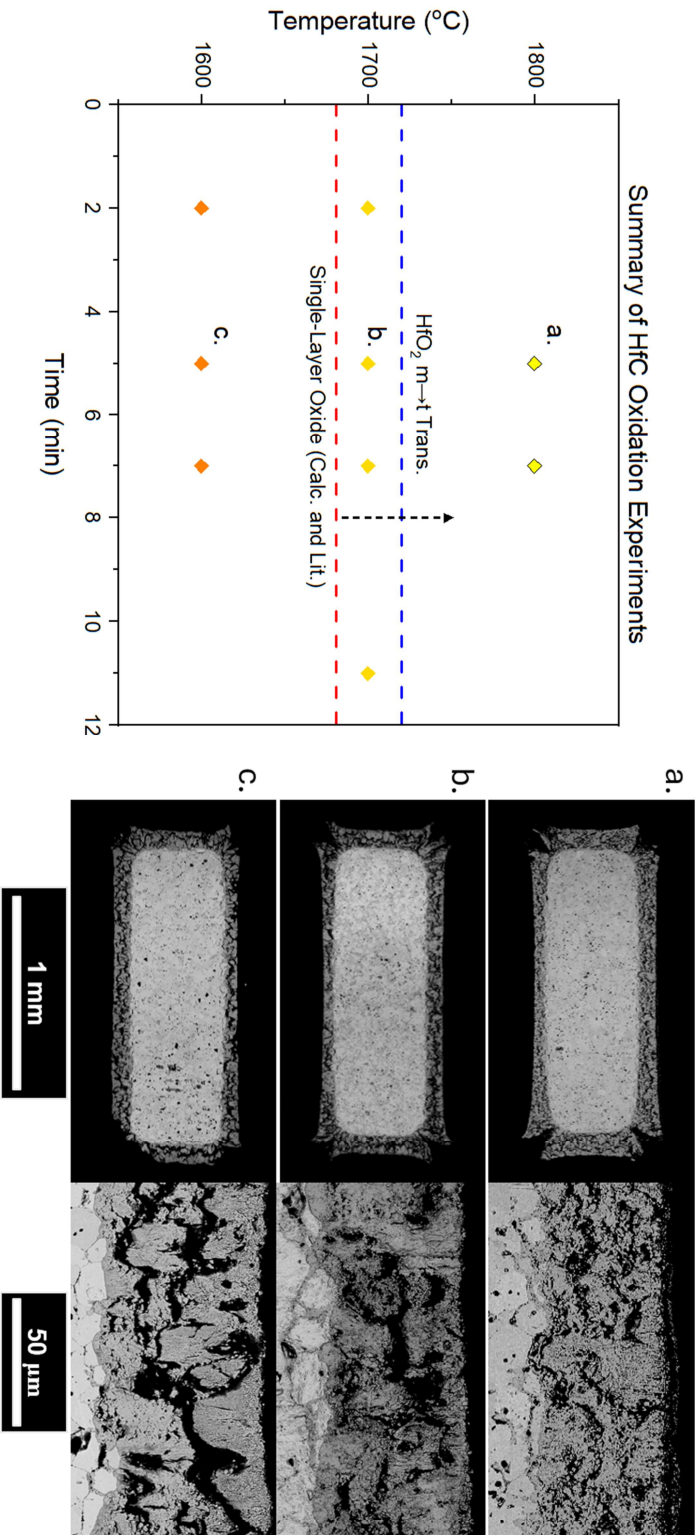
Figure 3.29: Backscatter cross section micrographs of Hf after 5-7 min of oxidation at 1600°C in 1% O₂ - Ar, demonstrating various phenomena observed during oxidation. (a) A partially cracked, partially two-phase oxide scale which was not adherent to the underlying Hf. The two-phase region shows highly aligned, acicular α -Hf in a HfO₂ matrix. (b) Shows a large finger-like microstructure at the metal/oxide interface; the oxide is very adherent to the metal.

with the two-phase region on the Hf-O phase diagram. The oxides were found to be mostly well-adherent. Sometimes the oxide delaminated from the underlying metal, leaving a small gap at the metal/oxide interface shown in Figure 3.29a. When the finger-like morphology is present, no delamination is observed. Also similar to Zr, the corners of the HfO₂ did not split to form a Maltese cross and large voids in the oxide scale can be found near the corners of the material, shown in Figure 3.28. Large voids in the center of the remaining metal are also visible in Figure 3.28.

A chart describing the oxidation mechanisms observed during the oxidation of HfC is shown in Figure 3.30. Representative polished cross sections of the hot zone for each area of the diagram are also displayed in the figure, showing an example of each oxidation temperature explored. Additional micrographs for all explored conditions can be found in Appendix A.

The oxides grown on HfC are very similar over all temperatures at which they were grown in this work. All show a highly porous oxide which also contains large voids. Additionally, each shows grain boundary oxidation and slight carbide grain liftout just near the carbide/oxide interface. Results are summarized in Figure 3.30 along with representative micrographs. A very thin layer is observed at the carbide/oxide interface, shown in Figure 3.31a, averaging $0.7 \pm 0.1 \mu\text{m}$ in thickness at all temperatures. An EDS line scan was conducted across this interface, shown in Figure 3.31b. Elevated levels of both carbon and oxygen are found in this inner layer. Immediately adjacent to the inner layer, striated layers of pores can be observed in the oxide which have a similar thickness to the inner layer.

Deeper investigation into this inner layer was conducted using TEM/EDS and SAED. A summary of these results is shown in Figure 3.32. The thin inner layer is found to be comprised of phase segregated HfO₂+C. SAED indicates that the oxide phase within this layer is primarily tetragonal phase. Farther into the oxide, the monoclinic phase is the primary polymorph.



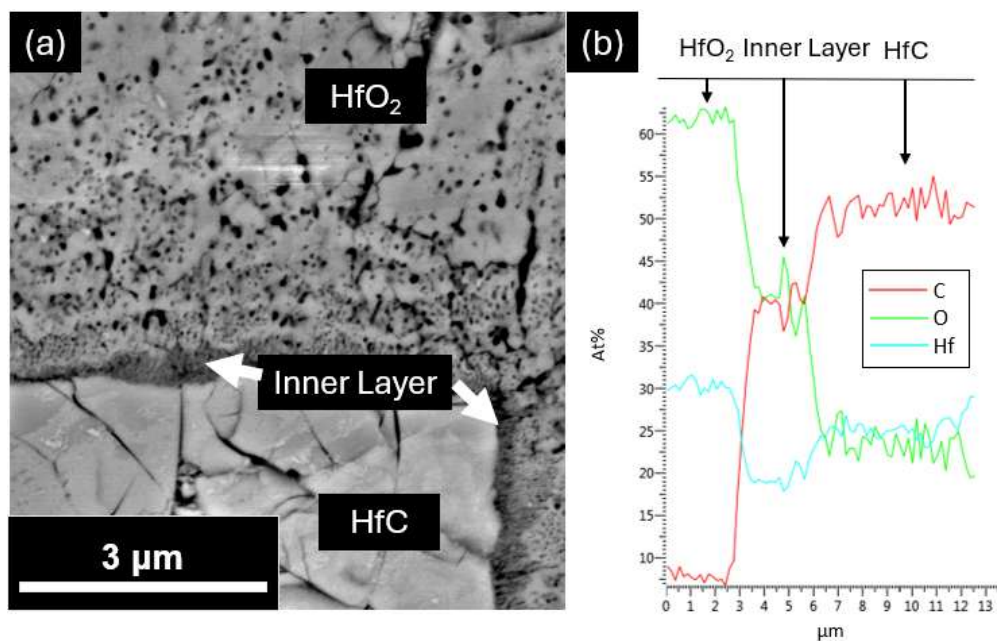


Figure 3.31: (a) Backscatter cross section SEM micrographs of HfC post-oxidation across the carbide/oxide boundary and (b) an EDS line scan across the inner layer. HfC oxidized at 1600°C for 5min in 1%O₂-Ar.

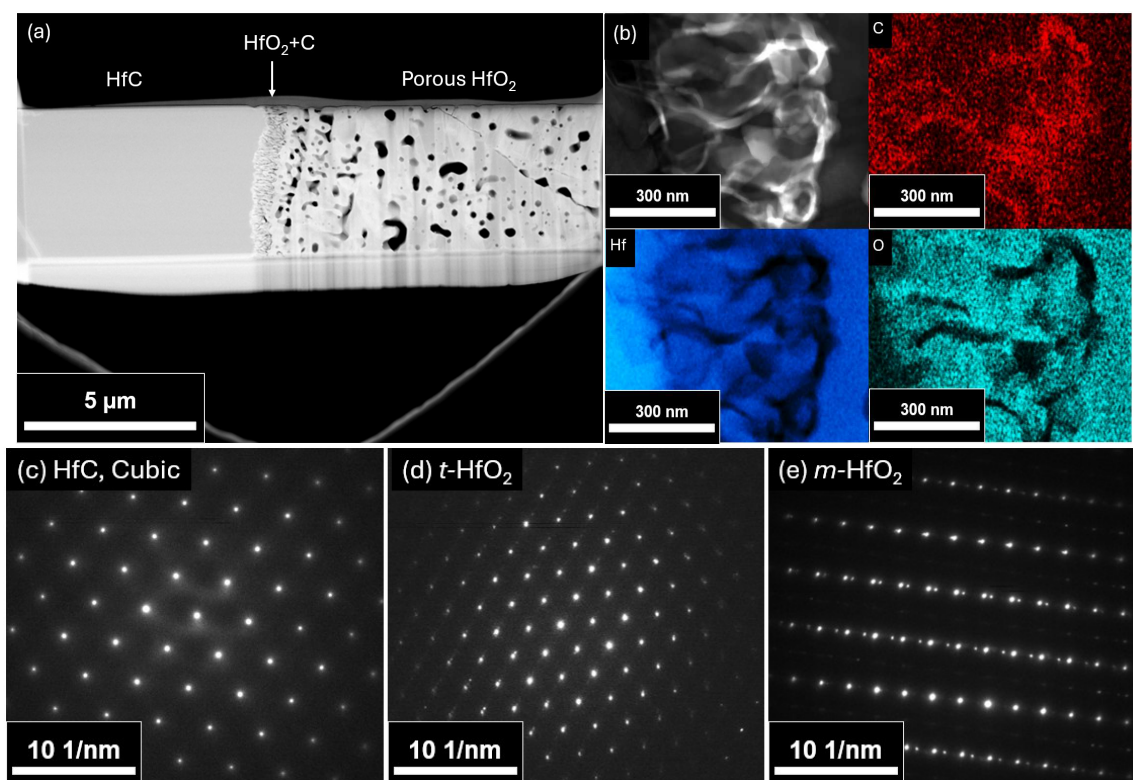


Figure 3.32: (a) TEM micrograph of a FIB liftout from oxidized HfC across the carbide/inner/outer layer boundaries; (b) TEM/EDS of the HfO₂+C layer; and (c-e) SAED patterns from the areas around the inner layer, showing (c) cubic HfC below the oxide, (d) tetragonal HfO₂ in the HfO₂+C layer, and (e) monoclinic HfO₂ in the bulk oxide. HfC oxidized at 1600°C for 7min in 1%O₂-Ar. TEM/EDS and SAED thanks to H. Heinrich.

The material recession rate for Hf and HfC are shown in Figure 3.33. For Hf, both a linear and parabolic fit with time are shown. An initially negative material recession was observed (i.e. bulk material swelling due to interstitial oxygen uptake) followed by a positive parabolic recession rate. After 7 min of oxidation, Hf experiences breakaway oxidation similar to Zr. The remaining metal was always found to be thicker than it was before the experiment (marked by the gray line at $y = 0$). The recession rate of HfC is found to be linear and relatively unchanged at all observed temperatures. The pre-breakaway recession rate of Hf and HfC are very comparable. After breakaway, Hf oxidation proceeds much faster than HfC oxidation.

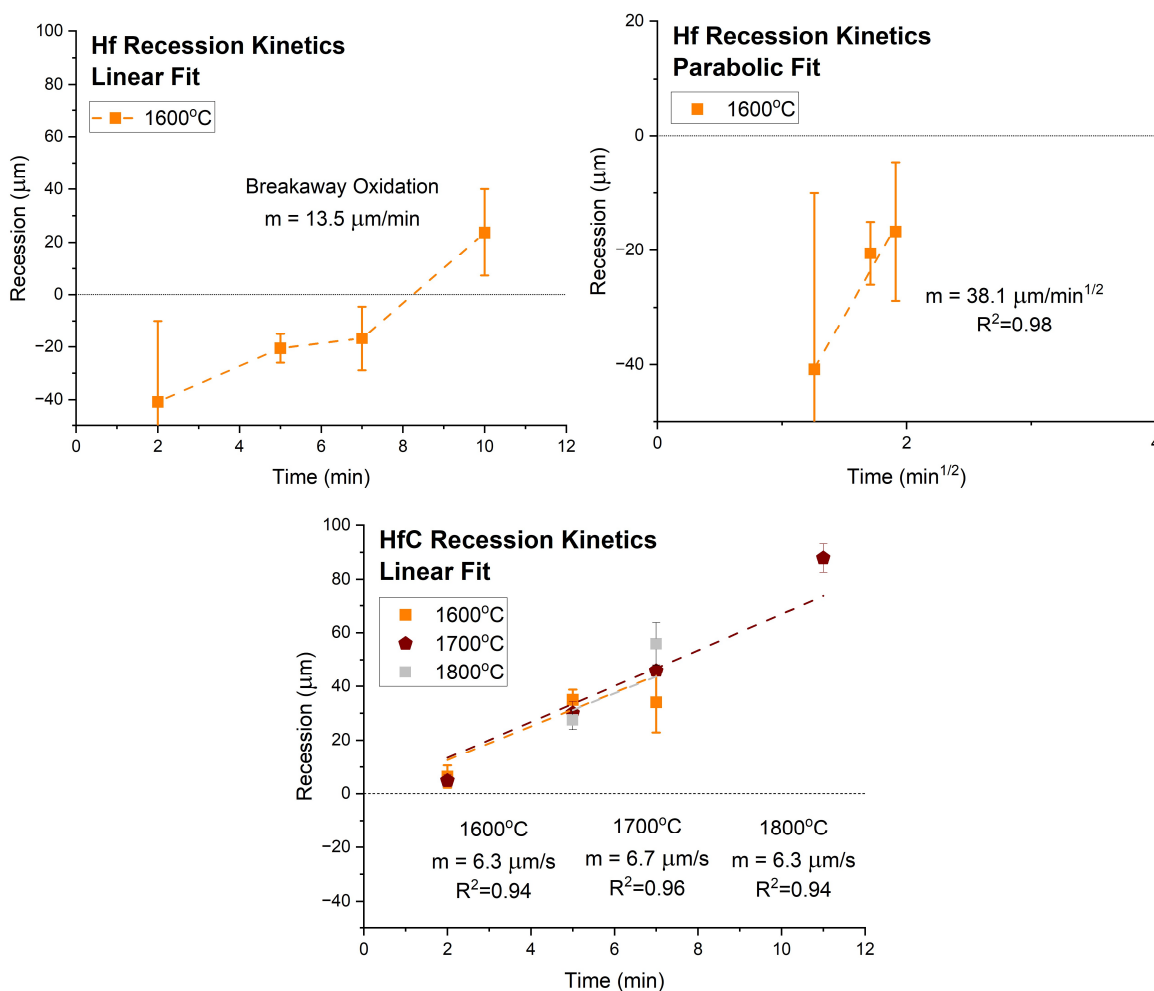


Figure 3.33: Recession rate of (top) Hf and (bottom) HfC. Recession for Hf shown versus (top left) t and (top right) $t^{1/2}$.

c. Discussion

As mentioned in the literature review section of this work, Hf and Zr are well known for having very similar properties and behaviors [75], including oxidation behavior [12]. Similarities between these materials are shown here by comparing the phase diagrams, oxidation behaviors, and post-oxidation microstructures of Zr and Hf within this work.

The same sequence of oxidation products following an increasing oxygen content are formed on Hf as were formed on Zr: metal with dissolved oxygen, followed by a two-phase oxide of α -Hf + HfO₂, followed by HfO₂. Some phases, such as the high temperature β -Hf phase, are not visible because the oxidation temperature explored here is below the α/β Hf transition point (1750°C). No $\alpha+\beta$ Hf Widmanstätten microstructure due to quenching is observed, though it would presumably form at temperatures greater than 1750°C. Unfortunately, due to sample softening, oxidation at such temperatures was not possible.

The microstructure of the two-phase oxide grown on Hf at 1600°C exhibits the same finger-like morphology shown previously for Zr oxidation at 1400°C. As previously noted, this results in the oxide growing in compression at the metal/oxide interface. The metal is therefore in tension during oxide growth. Such tension, coupled with the thermal shock created when the samples are quenched, results in the cracking seen throughout the remaining metal, such as that observed in Figure 3.28. In some cases, the compression in the oxide results in buckling and delamination, as observed in Figure 3.29a.

The recession rate of Hf prior to the breakaway event fits best to a parabolic trend. The oxide is not porous, indicating solid-state diffusion (Table 2.3.3) is the rate limiting mechanism. Unlike in the case of Zr, no oxygen-stabilized α -Hf zone is visible to confirm that oxygen diffusion

through the material is slowly occurring. However, the lack of an oxide scale on the long edge of the sample after 2 min of oxidation is indicative that dissolution of oxygen into the metal is still occurring. Thus, it can be concluded that oxygen dissolution into the metal is the rate limiting step prior to oxide scale formation.

Breakaway oxidation behavior in Hf has not been reported often but has previously been reported for Hf in steam environments [111]. In contrast, Zr breakaway oxidation is well studied due to its importance in predicting nuclear cladding lifetime [60], [61]. It was hypothesized here that, because of the similarities between Zr and Hf, breakaway oxidation is expected to occur, via the same mechanism as Zr breakaway. Compressive stresses in the oxide are created during growth at the metal/oxide, while tensile stresses are created at the oxide/gas interface due to unconstrained expansive growth. When a critical oxide thickness determined by these stresses is reached, oxide cracking occurs, and breakaway oxidation begins. However, oxide cracking is visible in many of the investigated scales before breakaway oxidation is observed (see Appendix A) and so cannot be directly correlated to breakaway behavior. More experimental evidence regarding stress states in the oxide is needed to verify the acting mechanism for breakaway oxidation.

Similar to Zr/ZrC, the oxides grown on HfC show a Maltese cross structure, while Hf does not. This is again attributed to the difference in oxygen solubility and substrate stiffness between the metal and carbide. During Hf oxidation, oxygen dissolution distributes the oxygen throughout the metal, deforming the metal via swelling and saturating corners of the sample first. Oxide grows on the corners before the oxide on the bulk material grows. The metal is plastic enough to deform, accommodating some of the oxide growth stresses so the oxide may grow freely without splitting. During HfC oxidation, the low solubility for oxygen causes oxide to grow more uniformly around the sample. The high stiffness of the carbide means it will not deform to accommodate the large

stresses created during oxide growth and these stresses concentrate at the corners, resulting in cracks to relieve the stress and Maltese cross formation.

The recession rates measured during the oxidation of HfC are linear and nearly unchanging as temperatures increase. The oxide is observed to be highly porous at all measured temperatures. It also contains large voids throughout the entirety of the scale. These are likely the origin of the linear oxidation kinetics (Table 2.3.2). This is in disagreement with Courtright et al.'s data which indicated a slowing parabolic oxidation rate as temperatures increased up to 1800°C [17]. The oxidation rates observed for HfC were forced through a parabolic fit and plotted compared to Courtright et al.'s [17] work and Scott et al.'s [80] work in Figure 3.34. Additionally, the observed pre-breakaway oxidation rate for Hf is compared to the extrapolated data from Smeltzer and

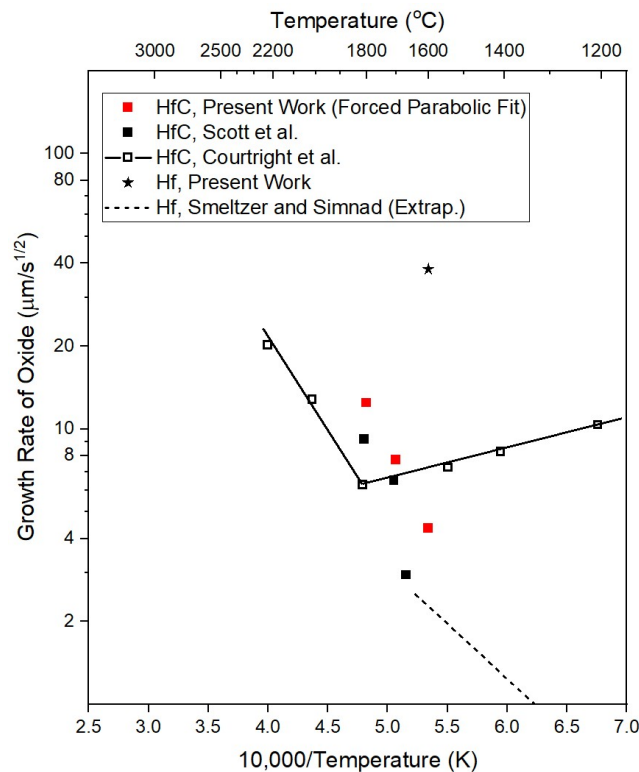


Figure 3.34: Comparison of the oxidation rates of Hf and HfC to the work completed by Courtright et al. (air, 21% Po_2) [17], Scott et al (1% Po_2) [80], and Smeltzer and Simnad (1-100% Po_2) [78].

Simnad [78]. The rates for HfC are very comparable to those found in literature, despite the disagreement of the observed mechanisms, but the rate for Hf is much higher.

The linear oxidation kinetics for HfC presented here are more closely aligned to the mechanisms observed by Berkowitz-Mattuck: linear oxidation kinetics and preferential grain boundary oxidation [16]. Indeed, grain boundary oxidation is observed at all temperatures, evident from the carbide grain-lift out at the carbide/oxide interface. Additionally, the unchanging oxidation rate with temperature agrees with the minimally temperature-dependent oxidation rates expected for gas-phase diffusion and reported by Holcomb et al. following his counter-current diffusion model, though the model predicts parabolic oxidation through fine pores in the oxide rather than linear oxidation in the large pores observed in this study [10].

The inner layer of HfO_2+C reported by several authors was found to be much smaller (~ 1 μm thickness) than indicated in literature (~ 90 μm [24], ~ 20 μm [26]). Despite being reported as a diffusion barrier to oxidation [17], [24], the growth of this layer is limited to this small thickness and no parabolic trend is observed during HfC oxidation. The unchanging thickness of the inner layer with time is a result of competing reactions to form HfO_2+C at the carbide interface and to form $\text{CO}(\text{g})$ at the inner/outer layer interface. The microstructure and phase content of the inner does, however, follow the observations of Scott, He, and Lipke, as shown by the TEM/EDS analysis in Figure 3.32 [26], [80]. As oxidation progresses, the carbon from the inner layer is oxidized, leaving behind a porous network which forms the outer layer pore structure [26].

Ellingham-type calculations of the Hf-C-O system were conducted using data from the FactSage “FactPS” database [109] to corroborate this temperature. The free energy calculations, shown in Figure 3.35, indicate that the formation of free carbon during oxidation is favored up to 1681°C . Beyond this temperature, $\text{HfO}_2+\text{CO}(\text{g})$ becomes the dominant reaction. Below 1681°C

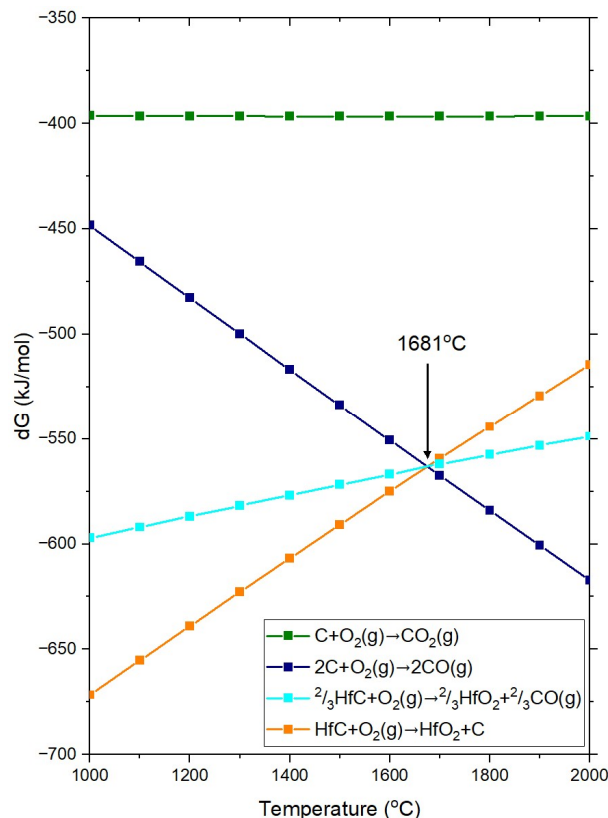


Figure 3.35: The HfC Ellingham diagram. Free carbon is no longer predicted to be the most stable C-containing reaction product above 1681°C; instead, CO(g) becomes most stable. Experiments just above this temperature do not align with these calculations.

Hf is preferentially oxidized from HfC at the carbide/oxide interface to form HfO₂+C. These results disagree with experimental findings. The retention of free carbon in the inner scale is observed at all measured temperatures (1600-1800°C), including above the calculated thermodynamic limit. Given temperature gradients through the oxide scale in RHS samples [100], potential errors in emissivity readings, and the uncertainty in the thermodynamic data, the accuracy of the sample temperature readings in the RHS is not high enough to sufficiently probe this temperature to an accuracy of less than ±50°C. Scott, He, and Lipke reported the free carbon layer to be absent above 1800°C as a result of an amorphous HfC_xO_y phase which forms at the carbide/oxide interface [80].

d. Conclusions

Oxidation studies of Hf and HfC were conducted between 1600°C and 1800°C for up to 11 minutes in a 1% O₂ – Ar environment. The oxidation behavior of Hf was found to be very similar to Zr, both microstructurally and kinetically. The oxidation of HfC was found to follow a linear growth rate, different from the parabolic growth rate usually reported in the literature. The oxidation rate of HfC did not vary significantly with increasing temperatures.

From these observations, the role of carbon in the oxidation of HfC is to disrupt the scale formation via the formation of gaseous CO(g), driving linear oxidation kinetics at all temperatures. An inner layer of HfO₂+C is observed, but in the results presented here, it does not act as a diffusion barrier as suggested by other researchers [24]. For Hf metal oxidation, high oxygen solubility delays the onset of oxide formation and causes swelling of the substrate. After maximum swelling, the parabolic recession rate of the Hf is comparable to the linear recession of HfC. After 7 minutes of oxidation, Hf experiences breakaway oxidation attributed to stresses formed during oxide growth. The smaller PBR of HfC (Table 2.2) and high porosity and large voids in the oxide scale prevent stress-related critical failure events such as breakaway, but the oxide still provides no barrier to oxygen ingress because of the porous scale. Above 1800°C, free carbon in the inner layer is no longer reported to be stable but is found in the oxides formed at 1800°C in the present study. Literature reports accelerated oxidation rates above this temperature [17], [26].

iv. Part 1 Conclusions

The oxidation of M vs MC (M = Zr, Hf, Ta) has been investigated at a variety of temperatures to elucidate the role of carbon on the oxidation process. A resistive heating system

(RHS) in conjunction with an emissivity-correcting pyrometer was utilized to conduct the experiments. This system has previously been used to conduct oxidation experiments on a variety of materials and has shown good agreement with the literature [49]. Oxidation was conducted at a reduced oxygen pressure such that material reaction with oxygen would be rapid and thus mass transport through the oxide scale becomes the rate-limiting step.

It was found that all three metals investigated exhibited initially parabolic oxidation kinetics. For Ta, this was governed by diffusion through a relatively dense scale at oxidation times less than 5 min. For Zr and Hf, this was governed by oxygen dissolution into the metal. These metals have high solubilities for oxygen (Hf ~20 at%, Zr ~29 at%) and so a significant amount of oxygen exposure is required to saturate these materials. Around 4-5 minutes of oxygen exposure, saturation of the material was reached and oxide growth began. Beyond these parabolic regimes, the metals all exhibited a breakaway oxidation behavior driven by cracking in the oxide scale. Linear kinetics were observed by all materials, indicating oxygen diffusion occurs via gas-phase diffusion through these cracks.

The oxygen solubility in the carbides is also substantially lower than the oxygen solubility in the metals, particularly of the group IV metals. Oxide growth was not delayed by the diffusion of oxygen through the bulk material, but instead began to form very early into oxygen exposure. This affected the way the oxide grows on the surface of the material to such a degree that the stress gradients through the scale were altered. For example, ZrC showed Maltese cross formation and cracking of the outer layer of its oxide scale, while the oxide on Zr metal grew in compression and did not display a Maltese cross.

For the carbides, carbon oxidation produces CO(g) which creates a network of pores in the oxide scale. As such, oxygen ingress through the scales was observed to be rapid and linear.

However, the porosity in the scales also increased the oxide scales' tolerance of the stresses created during oxidation. The porous scales did not experience cracking onset to allow for more rapid oxygen ingress through the scale than was already occurring through the pore networks. Therefore, while initial oxidation of the carbides was either of comparable rate or slightly more rapid than the oxidation of the metal during the parabolic oxidation regime, the carbides' unchanging oxidation mechanism yielded slower recession kinetics than the metals post-breakaway, despite the porous scale morphology. Additionally, sintering of the oxide can lead to a decrease in the average pore size in the oxide scale and in turn slow oxidation through the scale.

The oxides grown on the group IV carbides showed a two-layered oxide scale. The outer layer is porous and comprised solely of oxide. The inner layer is dense and comprised of oxide and free carbon. This inner layer, though reportedly growing parabolically, is shown not to have a significant impact on the oxidation kinetics. At higher temperatures, the formation of free carbon at this interface is no longer favorable, and a single-layered porous scale comprised solely of oxide is formed. Despite the loss of the parabolically growing layer, the oxidation rate of ZrC was shown to decrease where this layer is not present.

From these results, it is observed that the primary roles of carbon in the oxidation of transition metal carbides as compared to their metal counter parts are as follows:

- 1) Carbon reduces the solubility of the oxidizing material, affecting oxide growth initiation and altering the stress gradients formed in the oxide during growth. When carbon is not present, oxygen dissolution into the oxidizing material following parabolic kinetics can be a major part of the oxidation behavior.
- 2) Carbon oxidizes to form CO(g) , which creates a porous oxide scale as it egresses from the oxidizing material. This changes the oxidation mechanism from solid-state

diffusion limited to gas-phase diffusion limited. The carbides will oxidize with a linear kinetics. However, at higher temperatures, the increased surface area created by the pores can create a driving force for sintering, decreasing the pore size and pore network volume, decreasing the oxidation rate.

- 3) The porosity created by carbon oxidation and subsequent CO(g) egress can benefit the oxide scale by accommodating some of the stresses created during oxide growth. This can prevent cracking and other stress-related phenomena from occurring. For example, during the oxide growth of Ta and TaC at 1400°C, deformation of the oxide scale into a Maltese cross morphology happens in the dense oxide formed on Ta, but not in the scale formed on TaC.
- 4) The Pilling-Bedworth Ratio (PBR) for the carbides is consistently lower than for the metals. The smaller molar volume change prevents some of the large stress gradients in the oxides grown on metals from forming when the oxides are grown on carbides.
- 5) The melting point of the carbides is often much higher than the melting point of the metals. Therefore, the metals had a greater tendency to sag and deform during higher temperature oxidation experiments. The addition of carbon raises the melting point of the substrate and prevents the softening of the material. However, the lower stiffness of the metals may also accommodate some of the stresses created during oxide growth.

v. Future Work

While much insight into the role of carbon was obtained from this study, time and material supply constraints prevented much additional characterization which would enhance this work. In particular, more oxidation data would be beneficial in concretely determining the oxidation

mechanisms identified in this work. Additionally, more in-depth investigations into the minutiae of the oxidation mechanisms observed would greatly enhance understanding. In particular, the major role that oxide growth stresses played during oxidation was surprising and worthy of a large-scale investigation. Additional characterization of the carbon-rich inner oxide layers would also provide great insight into the oxidation of ZrC and HfC. Finally, significantly more effort should be put towards “double oxidation” oxygen tracer experiments. Visual tracking of oxygen diffusion through these scales is an invaluable resource which would certainly enable a more accurate understanding of the rate-limiting transport mechanisms at play during high temperature oxidation.

Part 2: Construction of a Novel Microplasma Resistive Heating System

a. Background

The hypersonic environment is characterized by high-enthalpy, highly dissociated gas flows across leading edge components. Starting around Mach 5, non-negligible quantities of atomic oxygen (AO) are produced in the vicinity of these surfaces. The effects of AO on the oxidation process are largely unknown due to the extreme nature of this environment and the difficulty of experimental evaluation. Traditional facilities for studying hypersonic flows, such as arc-jets and plasmatrons, are important tools which can simulate a realistic approximation of such environments. However, most large-scale facilities (except for the MESOX solar furnace [33], [34], [35], [112], [113], [114]) are not capable of isolating the effects of the plasma (and thus, AO) from temperature effects for oxidation studies. Additionally, these facilities are prohibitively expensive (\$150K+/day operating cost, \$1M+ to build) and are not feasible for high-throughput or large-scale studies. Microwave discharge furnaces are a more cost-effective option but tend to suffer from a low AO flux due to recombination at the chamber walls [37]. Low AO fluxes are not feasible for the short time scale necessitated by ultra-high temperature oxidation experiments. Thus, a new approach is needed to evaluate oxidation behavior in an ultra-high temperature, AO containing environment.

High-pressure DC hollow-cathode discharges, more commonly referred to as microplasmas (MPs), are a type of plasma where at least one dimension is smaller than 1mm [115]. It is shown here that the characteristics of these plasmas allow for the cost-effective production of AO for ultra-high temperature oxidation testing. The characteristics of MPs are as follows:

1. Near-atmospheric pressure stability (1-100 Torr magnitudes); allows for use of standard laboratory vacuum equipment to achieve discharge, reducing cost.
2. A non-Maxwellian, high-tail electron energy distribution function; more high-energy electrons in the plasma provide greater probability of dissociative collisions, increasing the flux of AO.
3. Non-equilibrium thermodynamics ($T_{\text{ion}} \ll T_{\text{electron}}$); the high surface-area-to-volume ratio of MPs quenches the ion temperature, resulting in a “cold plasma” ($\sim 100^{\circ}\text{C}$) and removing the effects of temperature from plasma.

By flowing a gas through a capillary with sufficient potential across it, a MP jet is formed. These jets have been used for a variety of applications, especially in nanomaterials synthesis [115], [116], [117], [118], [119], [120], [121]. In this objective, the aim is to utilize an MP to allow for cost-effective, ultra-high temperature AO oxidation studies. Designing a new RHS to incorporate an oxygen MP jet will allow for ultra-high temperature AO oxidation studies.

It has already been established that the RHS produces oxidation results which are comparable to a traditional furnace [49]. Extension of its capabilities to include effective AO generation would create a new oxidation tool which could be used to evaluate a material's oxidation resistance in a hypersonic-like environment. This system, while lacking the high-enthalpy characteristics achievable by an arc-jet or plasmatron facility, will enable the effects of AO to be decoupled from the high-enthalpy conditions, such as high temperature, high pressure, and high flow velocity. Additionally, the estimated cost of the new RHS and MP is only \$50K and with negligible operating costs. Thus, a RHS equipped with a MP will be a cost-effective, efficient way to gain a better understanding of the oxidation processes occurring in the hypersonic environment.

b. Construction Outline

The existing RHS in the Opila lab at the University of Virginia [100] currently utilizes five out of the six available flanges of its cube-shaped chamber. A new RHS was designed and constructed which utilizes the sixth and final flange on the bottom of the chamber to incorporate a MP. To differentiate this new RHS from the old, the new RHS is referred to as the **microplasma resistive heating system (MRHS)**. The MP used in the MRHS was designed after the one reported by Koh, O'Hara, and Gordon [116], [122].

Several necessary modifications were made to the MRHS to enable the function of the MP. MP operating pressures are between 1-100 Torr, so control over the background pressure in the chamber is needed. A pressure-sensing flow controller (PC-EXTSEN, Alicat Scientific, Tucson, AZ) in a control loop with a capacitance manometer (Baratron, MKS Instruments, Inc., Andover, MA) was installed which allows for fine control of the background gas inlet. Additionally, a needle valve was added to the vacuum line. These two features, in tandem, allow gas to be precisely added and removed to achieve steady-state pressures with ± 0.1 Torr accuracy. During operation, the MP jet exit is "pressure matched" to the chamber pressure to ensure even AO density in the jet [122].

Further design modifications were made to improve the MRHS capabilities relative to the original RHS. Primarily, an upgraded temperature controller, transformer, and emissivity-correcting pyrometer were installed to allow for higher experiment temperatures (up to 2500°C). Additionally, pressure conditions in the chamber are adjustable via a computer, centralizing the controls and making operation more straightforward. Finally, a larger chamber size was used, allowing more room for the MP jet, additional fittings on the chamber flanges, larger sample sizes, and easier loading/unloading of samples.

After construction, oxidation experiments were conducted using Ta to compare the extent of oxidation in the MRHS to that produced in the original RHS. AO production in the MP was also characterized by two methods. First, a benchtop plasma spectrometer (FLAME Miniature Spectrometer, Ocean Insight Inc., Orlando, FL) with a fiber optic feedthrough (Douglas Electrical Components, Randolph, NJ) was used to identify AO in the MP jet. Second, the dissociation efficiency of the MP was estimated by mass loss due to Kapton HN erosion [123] following ASTM E2089-15(R20).

For the mass loss experiments, Kapton HN films were placed between two PTFE washers to create a fixed exposure area. PTFE was chosen because of its low AO recombination coefficient [124]. Samples were placed in a vacuum chamber and evacuated to <200 mTorr for at least 48 h to remove any moisture adsorbed on the Kapton. They were then weighed using a precision microbalance (XSE205 DualRange, Mettler Toledo, Columbus, OH) and stored in a vacuum desiccant chamber. Before exposure, samples were reweighed to ensure no moisture had adsorbed to the Kapton, then loaded into the MRHS. After evacuating the chamber and refilling with Ar to 65 Torr, oxygen flow was started and the MP was turned on. Samples were exposed to the energized MP for 2-8 h, then re-weighed to determine AO flux f_{AO} according to Equation (1):

$$f_{AO} = \frac{\Delta M}{A\rho E_y t} \left[\frac{\text{O atoms}}{\text{cm}^2} \right] \quad (1)$$

where ΔM is the mass loss after exposure (g), ρ is the Kapton HN density (1.42g/cm³), A is the exposure area (cm²) t is the exposure time (s), and E_y is the known erosion yield of Kapton HN (2.81 x 10⁻²³ cm³/O atom). Shorter exposure times were not conducted due to the uncertainty in the erosion yield weight measurements at such times. The AO flux was compared to the estimated

flux of O_2 molecules f_{MO} passing through the capillary to determine the dissociation fraction η by the MP, as in Equation (2):

$$\eta = \frac{\frac{1}{2}f_{AO}}{f_{MO}} \quad (2)$$

where the $\frac{1}{2}$ accounts for the two oxygen atoms per MO molecule. These exposures were repeated using a pure Ar plasma and with a non-energized flow of 1% O_2 – balance Ar to ensure that neither the gas nor the plasma alone were causing erosion of the Kapton HN. Additional PTFE washers were exposed without a Kapton film to track and correct for mass loss from the PTFE.

c. Results

i. Construction of the MRHS

Figure 4.1 shows a picture of the fully constructed and operational MRHS, the operational microplasma, and a system schematic. The system can reach 10^{-2} Torr vacuum and be set to any pressure between 1-1000 Torr with 0.1 Torr precision. The equipped emissivity-correcting

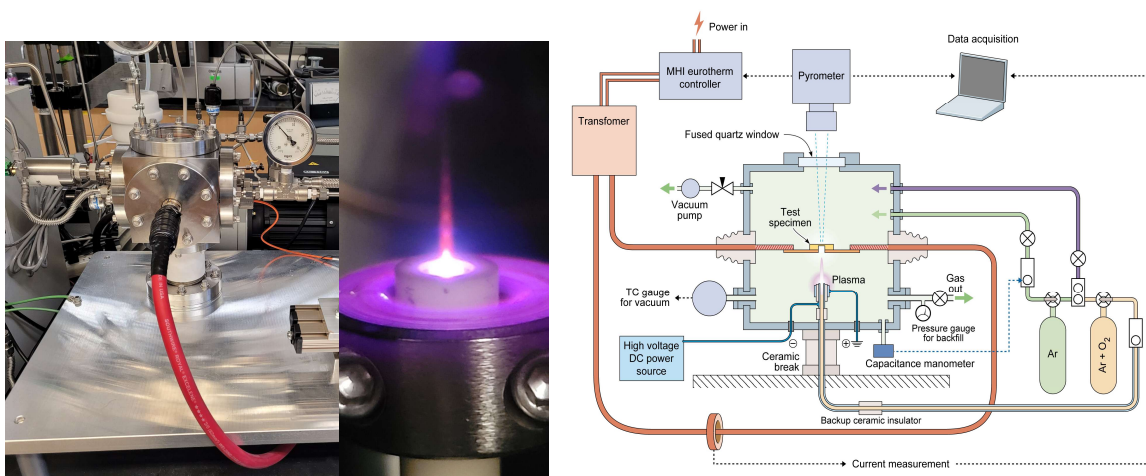


Figure 4.1: (left) The MRHS at UVA, (middle) the functioning MP jet in the MRHS, and (right) a technical schematic of the MRHS.

pyrometer (Pyrofiber Lab, The Pyrometer Co, Ewing, NJ) is capable of measuring temperatures up to 2500°C and has a spot size of 1.2mm. The power supply (BPAN-O-PLUS, MHI Inc, Cincinnati, OH) supplies up to 3000W to the sample. Temperature is controlled by a Eurotherm Controller in a feedback loop with the pyrometer. Sample temperatures up to 2400°C with $\pm 30^\circ\text{C}$ accuracy have been achieved.

The MP construction consists of a small stainless-steel capillary (I.D. 250 μm), an alumina dielectric tube, and an annular stainless steel outer cathode. A mixture of Ar and O₂ flows through the capillary at ~ 100 sccm. For MP experiments, the chamber is filled with background Ar gas to a pressure of 65 Torr. A regulated current of 8-20 mA with a negative DC bias is applied to the capillary and the outer electrode is connected to ground.

ii. Oxidation Validation

Ta oxidation experiments were also conducted in a RHS without a MP [100] to corroborate the reliability of the MRHS results. Figure 4.2 shows polished cross sections of the oxide on the bottom surface of Ta samples oxidized at 1300°C in the RHS and in the MRHS in MO only. Differences between the experiments include the direction of oxygen flow (the side of the sample

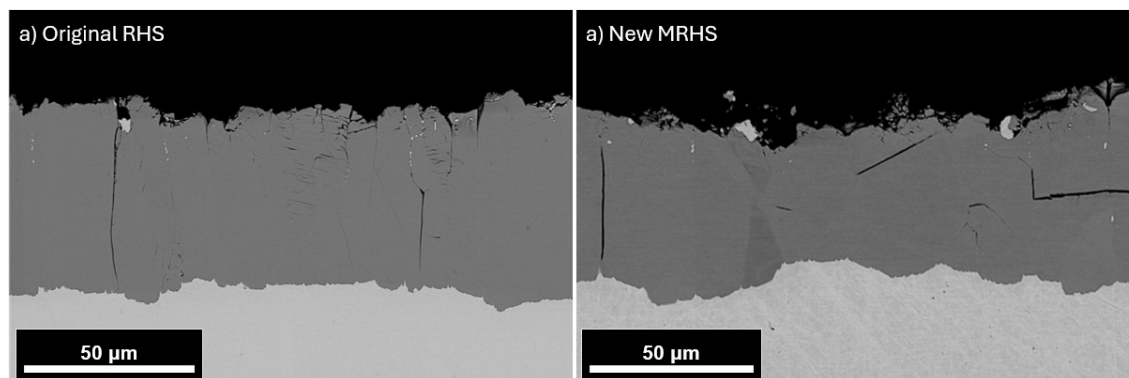


Figure 4.2: Polished backscatter micrographs of oxidation cross sections after oxidation in (left) RHS and (right) MRHS. Oxidized for 5 minutes at 1300°C in 100sccm of 1% O₂ – bal. Ar.

instead of the bottom) and background chamber pressure (one atmosphere Ar rather than 65 torr Ar). Recession of the Ta substrate was used as the comparative metric. Differences were statistically insignificant between the RHS ($39.0 \pm 6.0 \mu\text{m}$) and MRHS ($42.6 \pm 2.5 \mu\text{m}$). The oxidation kinetics of Ta were found to be consistent whether oxidation by MO is carried out in the MRHS or RHS, which compares favorably to results from indirect heating in a box furnace [49].

iii. Oxygen Dissociation Confirmation and Quantification

Plasma emission spectroscopy confirmed the dissociation of oxygen in the MP. AO has a strong, persistent emission line at a wavelength of 777.1 nm that is not shared by Ar and can thus be identified via emission spectroscopy. This peak was observed in any of the measured oxygen-containing gas conditions (0.1% - 20%, bal. Ar) while the MP jet was turned on. Additionally, when the MP gas was changed to pure Ar, the peak at 777.1 nm wavelength was absent. Example spectrographs from an oxygen containing flow and a pure Ar flow are shown in Figure 4.3. This evidence confirmed that AO was being produced by the MP.

Figure 4.4 depicts five Kapton HN samples after exposure to the MP. Three leftmost

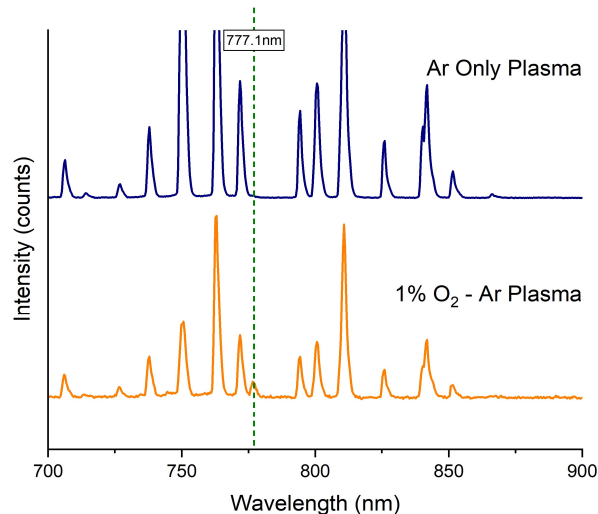


Figure 4.3: Emission spectrograph from the microplasma (15mA, 65 Torr, 0.25mm I.D.) in (top) oxygen containing and (bottom) pure Ar flows.

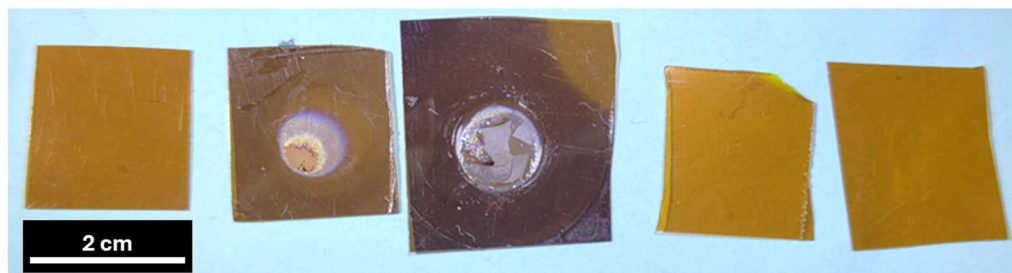


Figure 4.4: Kapton HN films exposed to (left to right) 0, 2, and 8 h in 1% O₂ plasma, 2 h in pure Ar plasma, and 2 h in 1% O₂ gas.

samples were exposed to 1% O₂ – balance Ar plasma. The second from the right was exposed to pure Ar plasma. The rightmost sample was exposed to a non-energized 1% O₂ – balance Ar gas. Increasing levels of erosion can be seen on the samples exposed to the oxygen-containing plasma. No erosion is visible on the film exposed to pure Ar plasma or the MO only gas.

Figure 4.5 shows the measured erosion mass loss and the dissociation fraction η calculated by Equations (1) and (2) versus time. The linear mass loss is consistent with literature regarding Kapton HN exposure to AO [123]. However, the linear trendline calculated does not intersect the origin. A satisfactory explanation for this has not been identified. The dissociation efficiency appears to be decreasing as time increases, with values near $\eta = 40\%$ estimated near $t=0$, while at

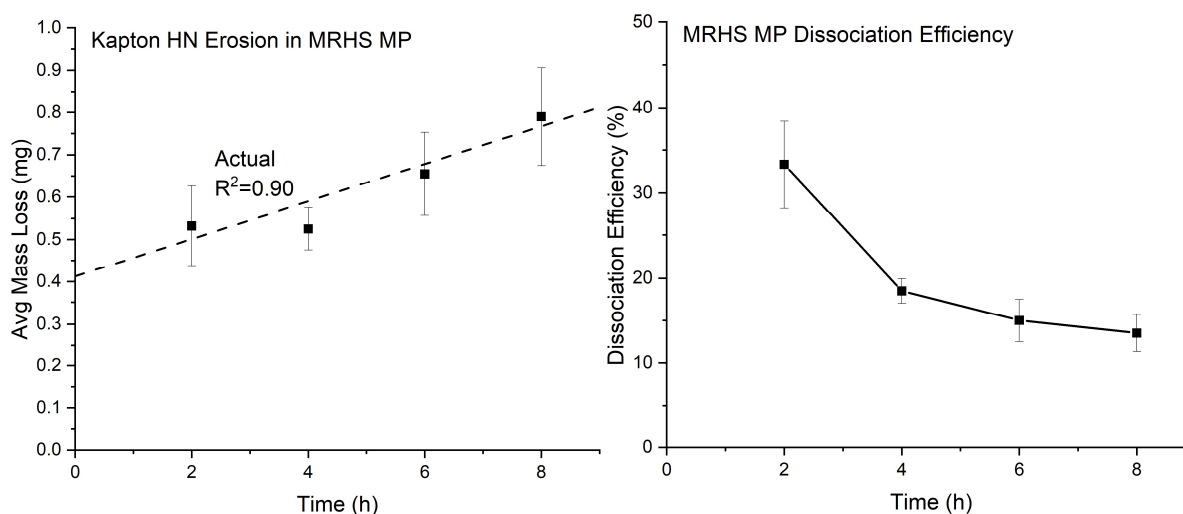


Figure 4.5: (left) Mass loss of Kapton HN films corrected for polymer hydration and mass loss from the PTFE washers; (right) Dissociation efficiency based on a 100 sccm flow of 1% O₂ – Ar through the MP capillary.

longer times, values closer to $\eta = 10\%$ are observed. The lack of damage on the Kapton exposed to an Ar only plasma exposure and the 1% O₂ – Ar gas further supports that dissociated oxygen is being generated. It is assumed here that the MP dissociates a 1% O₂ – balance Ar gas into 0.6% O₂ – 0.4% (2O) – balance Ar gas. The range of oxygen dissociation expected for hypersonic vehicles flying between Mach 8-10 is estimated to be between 10-50%, depending on altitude [125], so the MRHS will produce results representative of this flight regime.

d. Conclusions

The MRHS has been constructed and successful experiments have been conducted using this new system. Oxidation results in the MRHS are shown to be comparable to the original RHS for MO exposures of Ta. Plasma emission spectroscopy and Kapton HN erosion studies have verified the dissociation of oxygen in the MP jet. Mass loss measurements conducted according to ASTM E2089-15(R20) estimated the AO dissociation efficiency to be as high as 40%, which is within the hypersonic flight trajectories expected in the Mach 8-10 range.

e. Future Work

The AO dissociation fraction is sensitive to several factors, including the current applied, the capillary size, the relative height of the cathode compared to the capillary end, the thickness of the dielectric, and the pressure in the chamber. These parameters need to be systematically controlled to quantify the AO flux in the MRHS and will be systematically varied to get a better understanding of how the MP parameters affect the AO dissociation efficiency. Collaborations with the Dedic lab at UVA are planned to attempt more quantitative assessments of dissociation

efficiency, including two-photon absorption laser induced fluorescence [126] to provide spatially resolved concentration maps of AO in the MP jet.

Part 3: The Effects of Atomic Oxygen on the High Temperature

Oxidation of Transition Metals and Carbides

a. Background

Hypersonic vehicle leading-edge component materials will be exposed to ultra-high temperature, AO containing environments during flight. Given the established importance of oxidation on the lifetime of leading-edge components, it is critical to understand how AO present in the environment will impact the oxidation behavior of candidate materials. Significantly less work has been done evaluating the oxidation behavior of materials in atomic oxygen compared to molecular oxygen. Rosner and Allendorf showed for both Mo and W [30] and carbon [31] that oxidation attack is significantly increased in AO as compared to MO. The oxides MO_3 , WO_3 and CO/CO_2 are volatile and leave behind a fresh metal surface after oxidation occurs. However, very little literature exists which demonstrates the effect on oxidation when a condensed phase oxide is present on the surface of the material. In hypersonic-relevant materials, an oxide is certain to be present on the outer surface of the material. Therefore, understanding the interactions of AO with materials forming condensed phase oxides is critical to successful development of hypersonic-ready components.

Balat et al. studied the oxidation of SiC in MO and microwave-generated AO and observed the passive to active transition (SiO_2 to $\text{SiO}(\text{g})$) occurs at a lower P_{O_2} for AO as compared to MO [8]. Thus, SiC retains a passivating scale at higher temperatures in AO than in MO and could survive in highly oxidizing environments longer if the environment contains AO. They observed this effect to be contradictory to thermodynamic predictions and suggested that kinetics must play a large role in the active-to-passive transition in SiC. This effect could not be predicted and shows that it

is critical to conduct experimental evaluation of oxidation in AO as a part of the hypersonics materials design process.

The oxidation of ZrB_2 and ZrB_2 -SiC, which form glassy borosilicate scales has been investigated in AO containing environments. Monteverde and Savino explored ZrB_2 -SiC at temperatures up to 2000°C in an arc-jet and found ZrB_2 -SiC to have largely non-catalytic behavior and good survivability during re-entry condition testing but reported no specific effects of AO on oxidation [127]. Marshall et al. compared ZrB_2 -SiC oxidation in a plasmatron to oxidation in a traditional box furnace from 1250 - 1575°C [128]. They reported faster SiO_2 growth and slower volatilization and also found an increased passive regime of the borosilicate glass in dissociated oxygen, in good agreement with Balat's results for SiC. Li et al. qualitatively showed that the oxidation rate of ZrB_2 -SiC at 1500°C is largely pressure dependent and increases when AO is present [129].

The exothermic recombination of AO to MO is catalyzed on the surface of many materials and has been shown to have non-negligible effects on surface temperatures of highly catalytic materials, increasing surface temperatures by more than 200°C in some cases [36], [130]. Marschall et al. investigated the oxidation behavior of ZrB_2 -SiC in a plasmatron facility and found that the recombination of dissociated gas species, including AO, caused the temperature of their material to increase by up to 400°C degrees Celsius [130]. This temperature rise came after the loss of the protective SiO_2 scale, leaving only ZrO_2 behind. This temperature increase is likely to be much higher than would be experienced in a purely MO and AO environment because the plasmatron environment also contained atomic nitrogen, which is even more exothermic than AO upon recombination [131]. Regardless, Marschall et al.'s work suggests that a non-negligible degree of surface heating can occur on ZrO_2 during oxidation in AO-containing environments.

However, as previously discussed, the complexity of the environments in plasmatrons and arc-jets make it impossible to completely isolate and distinguish the effects of AO from the high pressures, high temperatures, high velocity, and high heat flux present in these systems. The MRHS described in Part 2 of this document provides a new, alternative technique to isolate AO as a variable in high temperature oxidation which can be switched on or off during experiments to better show its effects on oxidation kinetics and/or mechanisms.

A few studies involving the metals of interest in this work in AO have been conducted. Rosner et al. investigated the oxidation of Ta in AO at 2000K and P_{O_2} between 1×10^{-4} and 5×10^{-4} torr by measuring Ta wire resistance versus oxidation time and observed an increased oxidation rate when AO is an oxidant compared to MO; however, in these conditions, Ta oxides volatilize at rapid rate such that the metal surface is bare during oxidation [132]. Gusakov et al. studied Ta oxidation in AO between 500-1300°C and P_{O_2} between 6.8×10^{-5} and 5.3×10^{-4} torr [133]. In these conditions, solid oxide forms on the Ta but the low pressures increased conductivity in the oxide such that oxygen diffusion through the scale was not the rate limiting step. A similar study was conducted by Raspopov et al. for the oxidation of Zr in AO from 600-850°C at P_{O_2} between 7.5×10^{-5} and 7.5×10^{-4} torr, though they stopped their experiments prior to solid oxide formation [134]. To the author's present knowledge, no investigation of the oxidation of Hf, in AO environments have been conducted.

Very few studies have been conducted regarding the oxidation of the transition metal carbides in AO. Liu et al. investigated TaC as protective coating against AO damage for C-C composites in low earth orbit, but their material was maintained at room temperature while high energy AO bombarded the sample [135]. Similar studies were conducted by Liu et al. for ZrC coatings [136] and Luan et al. for HfC coatings [137], all near room temperature. No studies are known that

evaluate the isolated effects of AO on the high temperature oxidation behavior of any of the materials of interest here, especially in conditions in which a solid oxide scale is formed and retained on the material surface. The effects that AO exposure could have on the oxidation kinetics of transition metal and metal carbides are unknown, so studies isolating the differences between AO and MO oxidation kinetics are needed.

b. Methods

High temperature oxidation of the same M and MC materials (M = Zr, Hf, Ta) were conducted in the MRHS using select temperature and time ranges based on the results from Part 1. Each experiment was conducted twice, one with MO only as a baseline, and one with MO+AO to identify any differences. Samples were ramped to temperature at up to 5°C/s in 65 Torr background pressure of pure Ar. The background Ar pressure required for MP operation was maintained in both MO only and MO+AO exposed samples to minimize differences. For experiments with a MO+AO environment, the MP was energized before temperature ramp and while the sample was still in a pure Ar environment. In some cases, the sample material was coated on the pyrometer-facing surface (opposite of the MP-facing surface) with temperature-resistant, high-emissivity paint to help ensure accurate temperature readings from the pyrometer. No reactions between the sample and paint were noted. SEM was used to characterize the samples in plan view and in cross section. Oxide thickness data points represent the average obtained from at least two samples with 10-20 points measured from the middle third of the oxide facing the MP capillary on each sample (measured via ImageJ [101]). Reported error bars represent one standard deviation. Additional micrograph analysis was conducted via image thresholding in ImageJ [101].

Material used in these studies was acquired from the same sources as those described in Part 1: sheets of Ta, Zr, and Hf were made into RHS dogbone specimens via EDM, then subsequently polished to remove EDM residue. Three-inch pucks of TaC, ZrC, and HfC produced by HIP were acquired and diamond machined into RHS dogbone specimens. The HfC material used for this study was found to contain a high concentration of excess free carbon, ~42.5 vol%, shown in more detail in section *h*.

c. Oxidation of Ta in Atomic Oxygen

i. Results

Ta was oxidized in the MRHS at 1300°C, 1400°C, and 1500°C for 2.5 min and 5 min. Figure 5.1 shows example temperature versus time and resistive current versus time for Ta samples oxidized at 1300°C and 1500°C in the MRHS in MO only and in MO+AO. The temperature versus time data shows slight deviations from the set temperature when oxygen was first introduced, which then stabilizes to within $\pm 30^\circ\text{C}$. The slope of the resistive current data shows that, despite

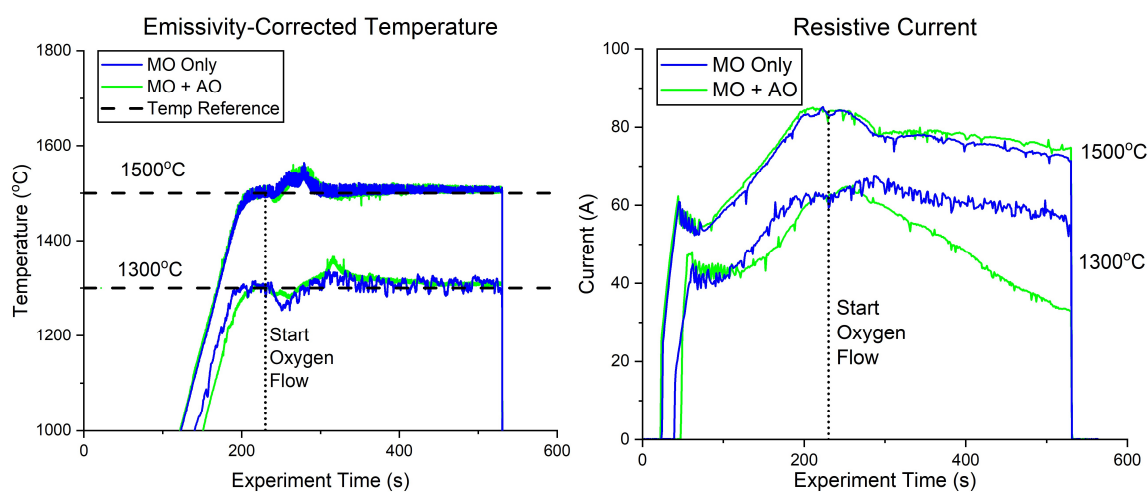


Figure 5.1: Temperature and resistive current data from the MRHS for Ta oxidation. Ta exposed to MO+AO at 1300°C has a much steeper slope in resistive current (i.e. higher oxidation rate) than observed in the MO only environment at roughly the same oxidation temperature. Ta oxidized at 1300°C and 1500°C for 5min in a 100 sccm flow of 1% O₂-Ar, 65 Torr Ar background.

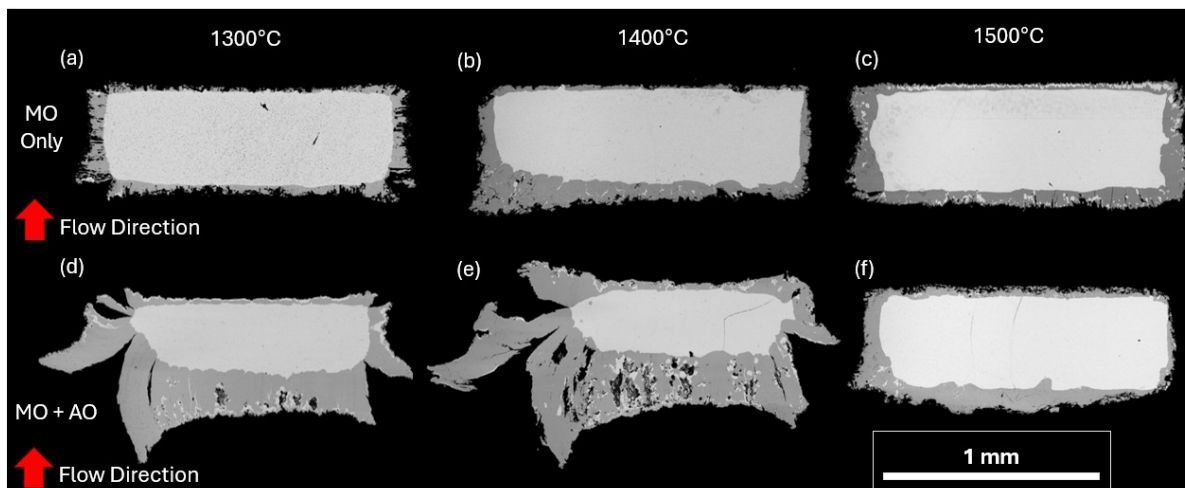


Figure 5.2: Polished backscatter cross section micrographs of Ta oxidized in (a-c) MO only and in (d-f) MO+AO in the MRHS. Oxidized for 5min at (a,d) 1300°C, (b,e) 1400°C, and (c,f) 1500°C in 1% $O_2 - Ar$ (total oxygen content). Flow rate from MP capillary for both MO only and MO+AO is 100 sccm to the bottom of the sample as indicated by the red arrows.

the temperatures being the same for oxidation in MO and MO+AO, the current needed to maintain 1300°C decreases more when AO is present in the chamber. The resistive current data for 1500°C oxidation in MO only and MO+AO are very similar.

Figure 5.2 shows a series of polished, cross-section micrographs of Ta after 5min oxidation in (a-c) MO only and (d-f) MO+AO environments, at (a, d) 1300°C, (b, e) 1400°C, and (c, f) 1500°C. ‘Maltese Cross’ morphologies are formed by oxide at the corners of (a), (d) and (e). This morphology is not observed for Ta oxidation conducted at 1500°C in either environment. Fig. 5.3

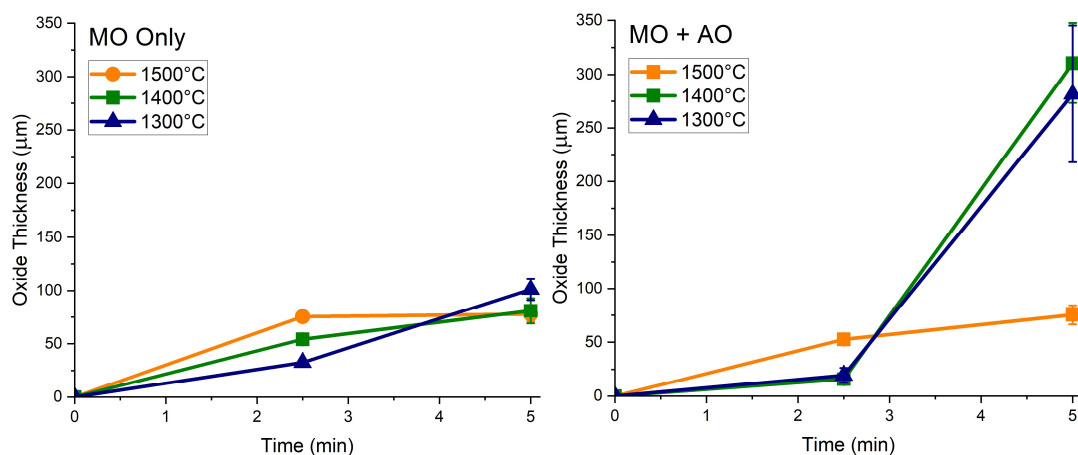


Figure 5.3: Oxide thicknesses after Ta oxidation in MO only and MO+AO environments. Error bars represent one standard deviation. Some error bars smaller than the size of the data points.

shows the oxide thickness measurements versus time for Ta oxidation in MO only and MO+AO environments. After 2.5 min, the oxides formed in MO and MO+AO containing environments are very similar in thickness and thicken slightly as temperature increases. After 5 min in MO only, this trend inverts, with the thickest oxide observed after 1300°C oxidation, and the thinnest oxide observed after 1500°C oxidation. After 5 min in MO+AO, both Figures 5.2 and 5.3 indicate large increases in oxide thickness after oxidation at 1300°C and 1400°C, while the oxide thickness after the 1500°C exposure is similar to the MO only exposure.

Figure 5.4 shows a series of higher magnification, polished, cross-section micrographs of the oxide formed on Ta in MO only. After 2.5 minutes (not shown), the oxides appear dense and adherent at all temperatures. After 5 min, oxide cracking is visible after oxidation at 1300°C and 1400°C. After 5 min of oxidation at 1500°C, little to no cracking is visible. Some unreacted Ta metal can be found in the oxide at all temperatures as observed in prior experiments in Part 1. Fig. 5.5 shows a series of high magnification, polished, cross-section micrographs of the oxide formed

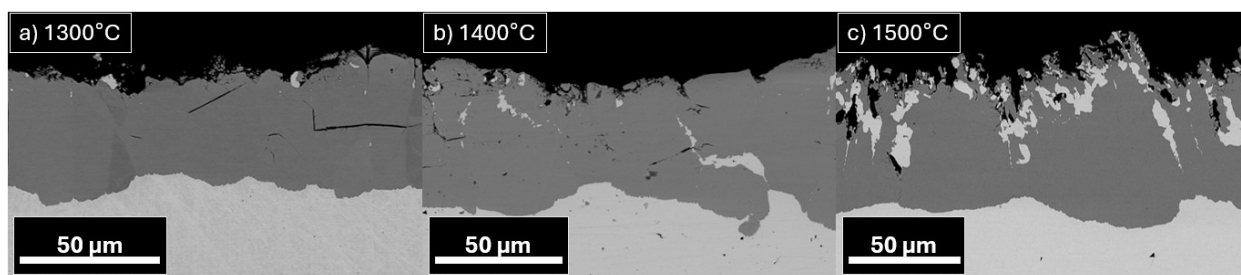


Figure 5.4: Backscatter SEM micrographs of polished cross-sections of Ta oxidized in 100sccm 1%O₂-Ar, MO only for five minutes at (a) 1300°C, (b) 1400°C, and (c) 1500°C. The oxides grown at 1500°C are notably less cracked than those grown at lower temperatures.

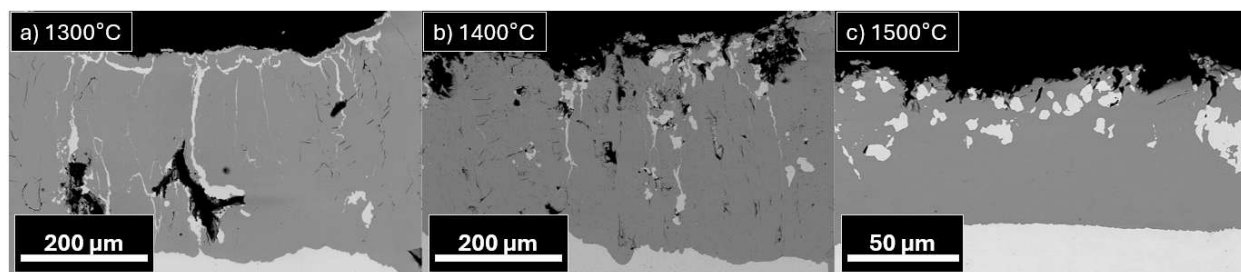


Figure 5.5: Backscatter SEM micrographs of polished cross-sections of Ta oxidized in 100sccm 1%O₂-Ar, MO+AO for five minutes at (a) 1300°C, (b) 1400°C, and (c) 1500°C. The oxides grown at 1500°C are notable less cracked than those grown at lower temperatures. Note the larger scale bar in (a) and (b).

on Ta in MO+AO. After 2.5min (not shown), the oxides are similar to their MO only counterparts. However, after 5min, the oxides formed after exposure to 1300°C and 1400°C are significantly thicker. The oxide formed after 1500°C exposure in MO+AO looks similar to its MO only counterpart.

ii. Discussion

XRD (not shown) indicates that the oxides formed above and below the oxide phase transformation temperature (1360°C) are identical for samples exposed to MO only or MO+AO. Thus, all effects of AO on oxidation rate are related to the greater reactivity of AO and of the microstructural features of the thermally grown oxide.

The slopes in resistive current versus time plot (Fig. 5.1) are indicative of oxidation rate. The amount of Joule heating is indirectly proportional to the cross-sectional area of the substrate. Thus, as the sample oxidizes, the cross-sectional area decreases, and the amount of current required to maintain a constant temperature decreases. It can clearly be seen that the Ta sample exposed to MO+AO at 1300°C has a much steeper slope than the sample exposed to MO only at 1300°C. This implies a greater oxidation rate when AO is present, which is also reflected in the kinetic data shown in Figure 5.3 and the oxide microstructures in Figure 5.5. The resistive current data for Ta oxidation at 1500°C indicates insignificant differences in oxidation rate between MO only and MO+AO exposures, also reflected in Figures 5.3 and 5.5.

The oxygen transport mechanism during the oxidation of Ta in the MRHS is consistent with the results in Part 1. In Figure 3.6, it was shown that Ta exposed at 1300°C and 1400°C undergoes breakaway oxidation earlier than observed at 1500°C. In Figure 5.2, the oxides grown at these temperatures are also shown to form a Maltese cross. Both of these microstructural features

likely allowed for rapid ingress of oxygen to the underlying Ta during oxidation. At 1500°C, the oxide has much less cracking than those formed at the lower temperatures. The corners of the sample are also much more intact, with no ‘Maltese cross’ morphology forming. Both the thinner oxide and some stress relief mechanism prevent the oxide from cracking and forming the typical ‘Maltese cross’ morphology. Similar to the results found in Part 1, the metal inclusions found in the scale were found to vary widely with temperature, environmental conditions, and time. No correlation was found between the amount and shape of these inclusions to any experimental conditions, and no good explanation for this phenomenon has been found.

The cracked oxides formed on Ta when exposed to 1300°C and 1400°C grow significantly thicker when oxidation occurs in an AO-containing environment. It is proposed that significant amounts of AO travel through the cracks without recombining to MO and react with the base Ta. This can be seen especially in Figure 5.2e, where one corner of the base Ta has been completely consumed. In contrast, the oxide grown at 1500°C shows nearly identical oxides in both MO only and MO+AO exposures. This is attributed to the formation of a dense, more protective oxide scale at 1500°C that prevents rapid oxygen ingress through the scale. Cracks are either smaller or entirely absent so AO cannot reach the surface of the metal without recombining to MO or adsorbing to the oxide. As such, AO can be used as a “leak detector”, showing when the oxide formed on Ta is protective or non-protective by finding cracks in the oxide.

d. Oxidation of TaC in Atomic Oxygen

i. Results

TaC was oxidized in the MRHS at 1300°C, 1400°C, and 1500°C for 2.5 min and 5 min. Figure 5.6 shows the measured thickness of the oxide after the experiments. In MO only, 1300°C

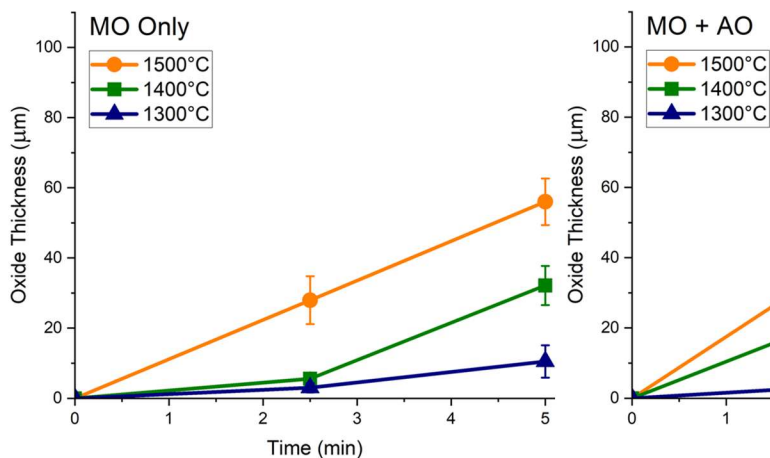


Figure 5.6: Oxide thicknesses after TaC oxidation in MO only and MO+AO environments. Error bars represent one standard deviation. Some error bars are smaller than the size of the data points.

and 1400°C exhibit a slower growth up to 2.5 min, followed by an increased rate up to 5 min. At 1500°C, the oxide growth rate is completely linear. In MO+AO, only 1300°C shows the slower growth rate up to 2.5 min, while both 1400°C and 1500°C show completely linear oxide growth rates. A slightly higher growth rate is found in MO+AO.

Figures 5.7 and 5.8 show polished, backscatter micrographs of the oxides grown on TaC in MO only and MO+AO, respectively. The oxides contain small pores and larger voids. As temperature increases, portions of the scale become less porous near the carbide/oxide interface, such as visible in Figure 5.8c. The larger voids were observed at all temperatures. At 1500°C, much larger voids sometimes formed at the carbide/oxide interface and caused delamination of the scale. Additionally, unreacted carbide grains can be seen throughout the oxide scales. At the oxide/carbide interface, oxide forms in the grain boundaries. An increasing amount of unreacted carbide grains are found in the oxide as temperature increases. This effect is amplified in MO+AO, with a greater area fraction of carbide grains found in the oxide scale when AO is present. The area fraction of the carbide grains in the oxide across the center third of each sample was quantified

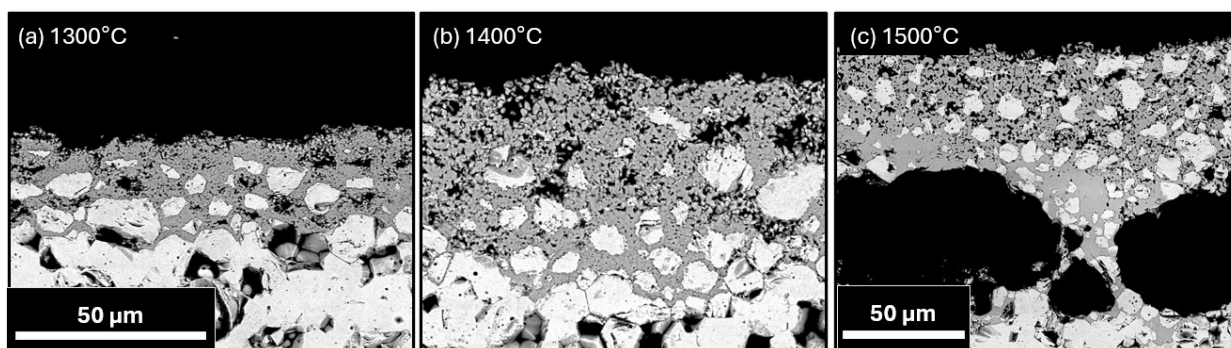


Figure 5.8: Backscatter SEM micrographs of polished cross-sections of TaC oxidized in 100sccm 1%O₂-Ar, MO+AO for five minutes at (a) 1300°C, (b) 1400°C, and (c) 1500°C. More carbide grains can be seen lifted out into the oxide scale as compared to MO only. Large void formation visible in (c).

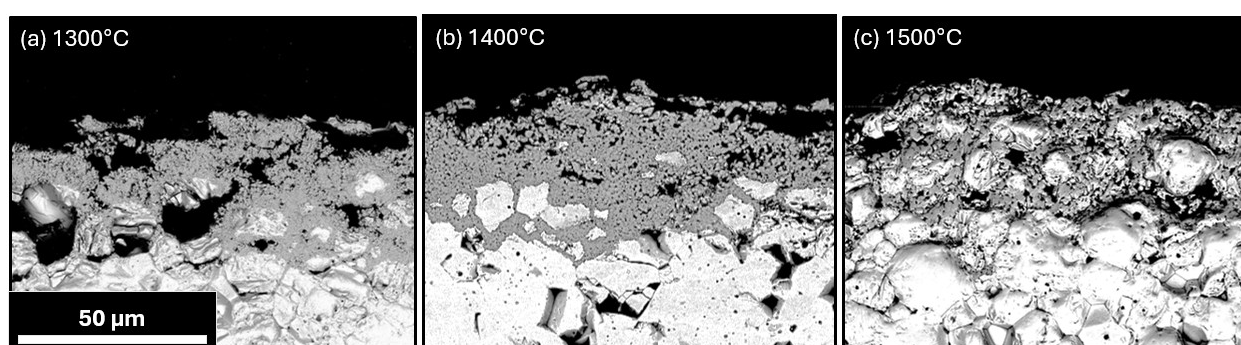


Figure 5.7: Backscatter SEM micrographs of polished cross-sections of TaC oxidized in 100 sccm 1%O₂-Ar, MO only for five minutes at (a) 1300°C, (b) 1400°C, and (c) 1500°C.

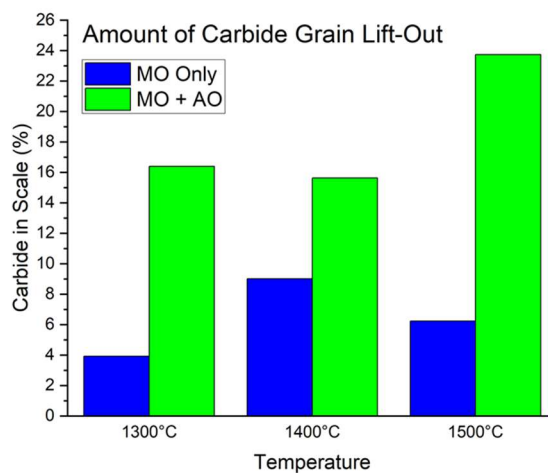


Figure 5.9: Area fraction of the oxide scales grown on TaC occupied by carbide grains after 5 min of oxidation. Data points are the average of at least two samples. Measured by image thresholding.

ii. Discussion

In Part 1, the oxidation kinetics of TaC were shown to be linear at all temperatures. Here, Figure 5.6 shows an increasing oxidation rate after a short incubation period at 1300°C and 1400°C. The oxide is generally very porous and has large voids throughout, so oxidation is almost certainly governed by diffusion through large defects in the scale (Table 2.3.2). Figure 5.8c shows very large voids which formed during oxidation in MO+AO at 1500°C for 5 min. A less porous oxide (not including the large voids) is observed near the carbide/oxide interface at 1500°C. However, the large voids in the scale provide fast-paths through the oxide. Therefore, AO ingress is not slowed and the oxidation rate still increases while this less porous scale is grown. This matches the trends observed in Part 1. The increase in oxidation rate in the MO+AO environment also suggests that AO is able to diffuse through the large voids in the oxide scale formed on TaC without recombining to MO and without exchanging with the oxide network. As such, it is likely that AO is transporting to the underlying base carbide through the large voids in the scale. The enhanced oxidation rate at higher temperatures and in MO+AO will yield a greater amount of CO(g) upon carbon oxidation. The reduced porosity in the scale causes the CO(g) to build up near the carbide/oxide interface. This results in the large voids and delamination visible in Figure 5.8c.

The solubility of oxygen in TaC is very low, so the incubation period is not likely to be oxygen diffusion into the substrate, as was observed for Zr and Hf metals. It is suggested that oxygen diffusion into the grain boundaries of the carbide is responsible for this delay. This was not observed in Part 1 but may be explained by the difference in oxygen flow rate in the RHS (1000 sccm) vs the MRHS (100 sccm). Oxygen will diffuse through the sample via grain boundaries until the P_{O_2} is high enough such that significant oxide formation begins. The higher flow rate of oxygen causes this point to be reached more quickly, so no incubation period was observed.

Grain boundary oxidation becomes increasingly important in TaC oxidation as temperature increases from 1300°C to 1500°C and when AO is introduced to the environment. In MO only exposures, the incubation period is found during oxidation at 1300°C and 1400°C but is absent at 1500°C. In MO+AO exposures, the incubation period was only observed at 1300°C, while 1400°C and 1500°C exposures followed highly linear growth rates. The degree of carbide grain liftout also increased significantly during MO+AO exposures, as shown in Figure 5.9, suggesting that increased grain boundary oxidation occurs when AO is present.

e. Oxidation of Zr in Atomic Oxygen

i. Results

Zr was oxidized in the MRHS in MO only and MO+AO at 1400°C for 3, 5, and 7 min. The same oxidation products were observed as in Part 1. An oxide scale is grown which contains a cracked ZrO_2 and/or a two-phase α -Zr(O)+ ZrO_2 layer. When formed, the two-phase layer always forms adjacent to the metal/oxide interface, with a ZrO_2 only layer observed at the oxide/gas interface. Below the oxide scale, an oxygen-stabilized alpha-case (a.k.a. α -Zr(O)) layer is formed. At the center of the remaining metal is a two-phase α + β Zr region (see Figure 2.1). Figure 5.10 shows the growth rate of the full oxide scale, the two-phase oxide layer, and the alpha-case layer of α -Zr(O) after MO only and MO+AO exposure. For MO only exposures, the oxide growth rate is highly linear. In MO+AO, the oxide scale grows according to a cubic rate law. An ideal cubic growth rate is also plotted on the oxide scale plot, for reference. In the MO only environment, the two-phase layer is not initially present at 3 min, then grows with time, while in MO+AO it initially dominates most of the scale and grows thinner with time. The growth of the alpha case layer is

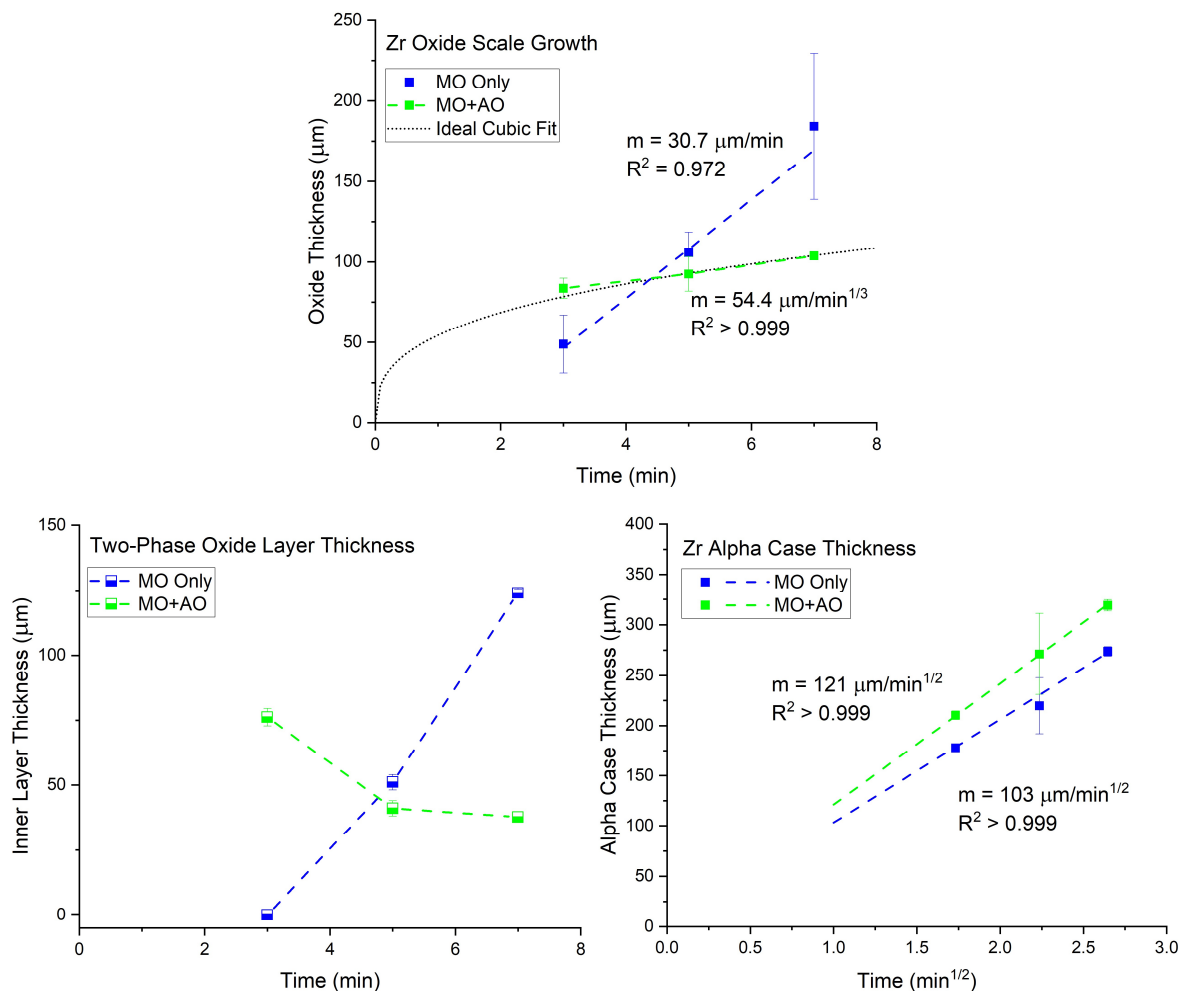


Figure 5.10: (Top) Total oxide growth rate, (bottom left) inner layer growth rate, and (bottom right) alpha case growth rate on Zr exposed to 1400°C in MO only and MO+AO environments. Error bars represent one standard deviation.

shown to grow parabolically over all measured times. In MO+AO environments, the alpha-case layer is initially thicker than and grows slightly faster than the alpha-case layer grown in MO only environments.

Oxide microstructures from Zr oxidized for 3 minutes in MO only and MO+AO environments are shown in Figure 5.11. The oxide grown in MO+AO is comprised of primarily the two-phase α -Zr(O)+ZrO₂ microstructure. The α -Zr(O) phase is found as large streaks in the oxide, as well as smaller, highly acicular precipitates within the oxide. The outer edge of this oxide

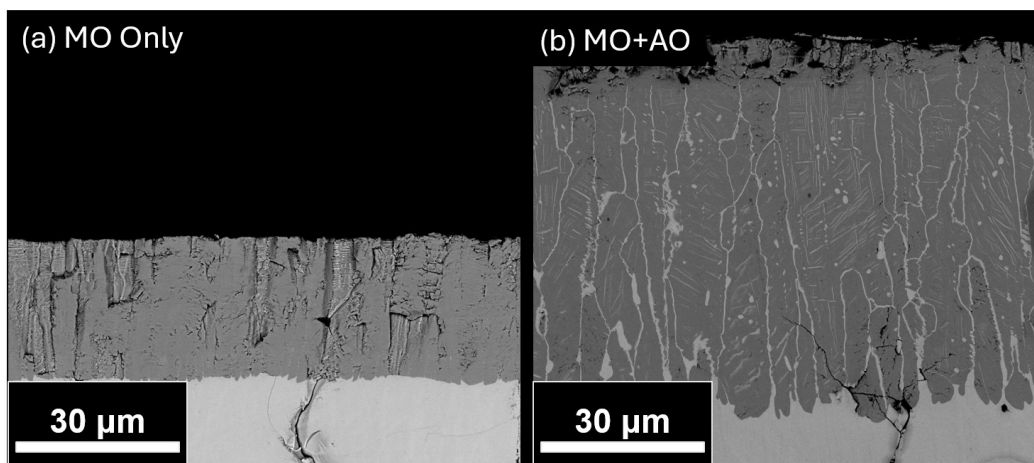


Figure 5.11: Backscatter SEM cross sections of the oxides grown after being exposed to (a) MO only and (b) MO+AO environments at 1400°C for 3 min.

also shows a cracked morphology. The oxide grown in MO only is single phase ZrO_2 and shows a full cracked morphology after 3 min of oxidation.

The full cross sections of Zr oxidized for 5 min at 1400°C in MO and MO+AO are shown in Figure 5.12. Appreciable cracking of the Zr metal is shown in both samples, especially on the lower half of the sample where oxygen impingement and oxide growth take place. On the sample grown in MO+AO, the width of these cracks is larger. Crack width versus oxidation time is reported in Figure 5.13. Crack width in the underlying Zr is consistently larger when oxidized in MO+AO environments as compared to MO only environments. Crack growth in MO+AO is shown to follow a cubic rate, while crack growth in MO only followed a linear rate.

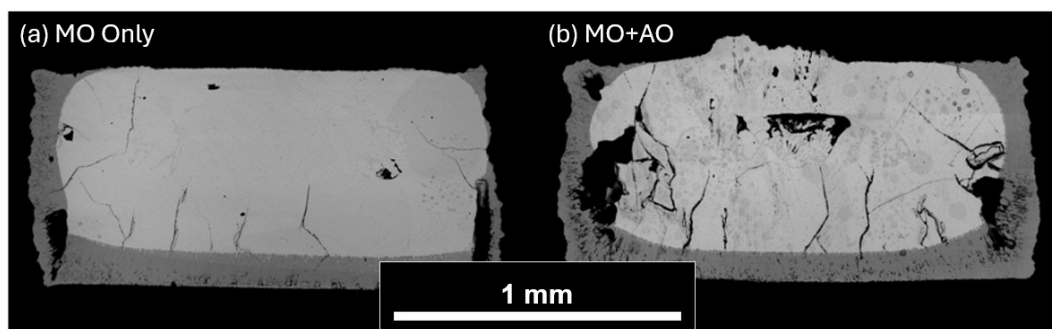


Figure 5.12: Backscatter SEM cross sections of the full sample after being exposed to (a) MO only and (b) MO+AO environments at 1400°C for 5 min. Cracks are visible in the Zr metal just inside the metal/oxide interface.

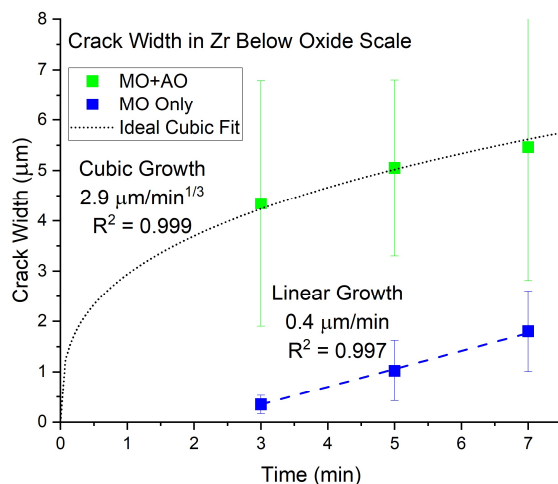


Figure 5.13: Difference in crack width in the Zr below the oxide scale after oxidation. Cracking is consistently more severe after MO+AO exposure than after MO only exposure. Cracking growth rates also follow the same trends as the oxidation kinetics. Error bars represent one standard deviation.

ii. Discussion

In MO+AO, Zr oxidation at 3 min is clearly more rapid than for MO only environments (Figure 5.10). AO has been shown to adsorb more readily on the surface of Zr than MO [134]. As such, the surface of the metal will saturate with oxygen more quickly in AO-containing environments, starting oxide growth sooner. This enhanced adsorption rate also affects the growth of the alpha-case Zr. Solid-state diffusion is driven by differences in chemical potential, which is often denoted as differences in concentration, such as in Fick's 2nd Law:

$$\frac{\partial c_i}{\partial t} = D_i \frac{\partial^2 c_i}{\partial x^2} \quad (5.1)$$

where c_i is the concentration of species i . The diffusivity D_i follows an Arrhenius trend, given by:

$$D_i = D_o e^{-\frac{\Delta G_M}{RT}} \quad (5.2)$$

where D_0 is a pre-exponential coefficient and ΔG_M is the free energy barrier to lattice migration, both of which depend on the diffusing species, oxygen in this case. MO will dissociate upon chemisorption to the metal surface and subsequently diffuse through the metal as the atomic species, regardless of dissociation state prior to adsorption. It is assumed that D_0 and ΔG_M remain unchanged for oxygen dissolution in Zr between the MO only and MO+AO environments because the pre-adsorption state of the oxidant will have no effect on the diffusing species.

Assuming the diffusivity of oxygen interstitials D_i in Zr is unchanged between the MO only and MO+AO environments, it follows that differences in the diffusion rate must be driven by changes to the concentration gradients in the bulk. In the case of MO+AO oxidation, the increased adsorption rate drives the surface oxygen concentration to increase to saturation more quickly, creating a steeper chemical potential gradient and driving more rapid diffusion through the Zr metal. Figure 5.10 shows that the α -Zr(O) is measured to be slightly thicker and grow slightly more rapidly in MO+AO environments than in MO only environments. However, the difference in growth rates is statistically insignificant (<50% confidence interval from t table).

As previously discussed in Part 1, the oxide grown on Zr grows in compression, evident from the oxide rumpling and delamination (see Figure 3.14c and 3.17). Oxide cracking as a result of stress gradients in the scale is the initiating mechanism of the breakaway oxidation behavior for Zr. The lack of cracking in the oxide and the slower sub-parabolic oxide growth in MO+AO between 3-5 min indicates that the oxidation sequence is pre-breakaway onset. The increased reactivity of AO is evident from the growth kinetics of the two-phase oxide layer in MO+AO, which decreases in thickness with time.

However, breakaway oxidation reportedly begins when the oxide thickness exceeds a critical value which can be calculated based on growth stress mechanics [69]. It is counterintuitive that breakaway oxidation would be delayed for an oxide scale which is initially thicker as demonstrated in the MO+AO case. Despite the lower oxide growth rate, oxide cracking is shown to occur in thinner oxides in MO only environments in Figure 5.11. The oxide grown in MO only is cracked at all observed times, i.e. it is post-breakaway onset, explaining the highly linear growth rate shown in Figure 5.10. The only variable which was changed in these experiments is the presence of AO, and so the mechanism change must be connected to AO introduction, as described next.

The oxide scale grown on Zr in MO+AO grows according to a cubic growth rate. In Part 1, Zr was reported to exhibit a parabolic recession rate, but a parabolic rate law does not fit this data from Part 3 well. Zr has been commonly reported as having a cubic growth rate [58], [138], [139]. A cubic kinetic rate law has been shown to occur in scales which grow simultaneously with grain growth in the oxide [140], [141]. However, no evidence of significant changes in grain size was observed. Evans et al. developed a model for cubic oxide growth based on defect chemistry and vacancy diffusion in an oxide scale growing under stress [142]. Their model showed that compressive stresses created at the metal/oxide interface will decrease vacancy concentrations and diffusivity throughout the oxide scale. Oxygen vacancies are known to be the primary defect in ZrO_2 , especially at reduced oxygen pressures, and are responsible for oxygen diffusion through the scale [143], [144], [145]. Thus, compressive stresses in an oxide scale can lead to an apparent cubic oxidation rate. This model was found to fit experimental Zircaloy oxidation data (pre-breakaway), including observing the mechanism change from parabolic to cubic as the oxide and compressive stresses grow.

As discussed in Part 1, El Kadiri et al. reported that the critical oxide thickness for breakaway oxidation onset is dependent on the lateral stresses at the metal/oxide interface [69]. An explanation is, therefore, required to discern when compressive growth stresses in the oxide lead to a cubic oxidation rate law or to breakaway oxidation. One mechanism proposed to explain delayed breakaway oxidation for Zr in MO+AO which fits all the currently observed trends, is a decrease in the stress gradient in the oxide as a result of embrittled substrate cracking. As a result of growth, the more voluminous oxide will be in compression at this interface, while the underlying metal will be in tension. Cracking of the underlying Zr can be seen in Figure 5.12. This cracking results in stress relief at the metal/oxide interface. During oxidation in MO+AO, the average width of these cracks is observed to be greater at all times than those found in MO only oxidation (Figure 5.13). This is also true after 5 min of oxidation when the grown oxides are roughly the same thickness, suggesting oxide thickness alone does not contribute to the difference in cracking. The same applies to the thickness of the two-phase layer in the oxide, so it also does not contribute to this effect.

Zr is well known to undergo a ductile-to-brittle transition at high dissolved oxygen contents at high temperature [146], [147], [148]. It is suggested that these cracks form during oxidation, similar to that observed by Hózer et al [147], as a result of the growth stresses putting increased tension on the brittle α -Zr(O). The greater fraction of embrittled α -Zr(O) metal created by enhanced AO adsorption/diffusion plus the initial rapid oxide growth shown in the MO+AO environment causes the critical stress of the metal to be reached early in the oxidation process, and cracking of the substrate occurs before cracking of the oxide. These cracks then expand with time according to the same rate laws which the oxide growth follows, further suggesting the formation of these cracks are tied to oxidation stresses. These observations are made in comparison to the

MO only exposure case, where slower oxygen saturation limits cracking the underlying Zr, causing the oxide to crack to accommodate the stresses created during growth. In this way, oxidation in MO+AO delayed the onset of breakaway oxidation, despite the more severe initial oxide growth. Computational or experimental evidence of stress states in the substrate and oxide is needed to support this mechanism; however, the microstructural and kinetic observations are all consistent with the proposed mechanism.

f. Oxidation of ZrC in Atomic Oxygen

i. Results

ZrC was oxidized in the MRHS at 1600°C for 2, 5, and 7 min and at 1800°C for 5 min. in both MO and MO+AO containing environments. Figures 5.14 shows the oxide scale growth rate of the full scale and of both the individual layers. The outer scale was found to grow with linear kinetics, while the inner scale was found to grow with parabolic kinetics. The full scale is also shown to grow with parabolic kinetics. The total growth rate shows an increase when AO is present. The inner carbon-rich layer is shown to have a nearly identical growth rate in both MO only and AO+MO environments. The outer carbon-free layer, however, shows a significant increase in growth rate when AO is present in the system, accounting for all the measured difference in growth between the MO only and AO+MO environments.

Figure 5.15 shows polished, backscatter SEM micrographs depicting an example oxide microstructure after ZrC oxidation at 1600°C for 7 min in an MO only and an MO+AO environment. The two-layered oxide scale is visible in both images. The thickness of the outer, carbon-free layer is much greater in the MO+AO environment than the MO only environment,

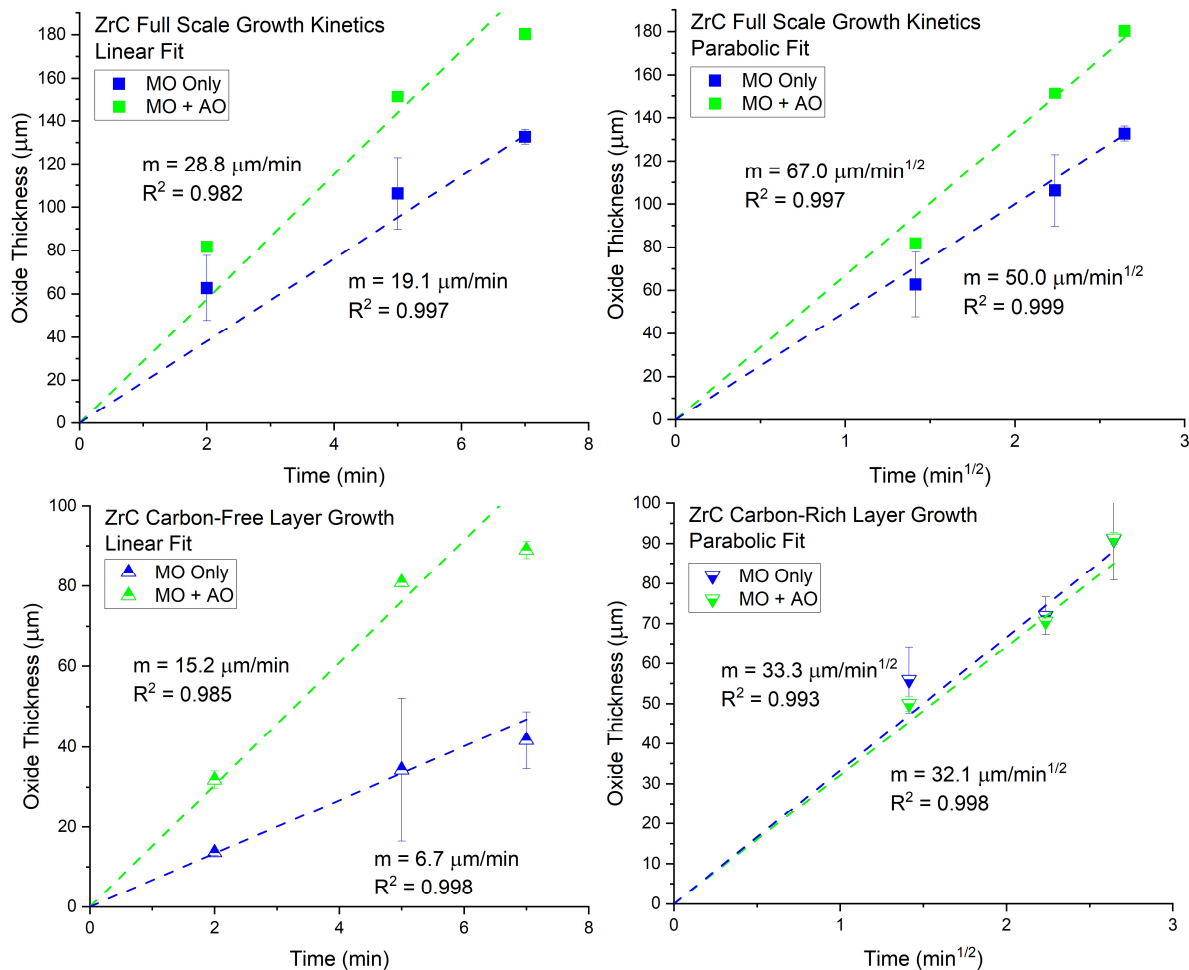


Figure 5.14: The growth rate of the oxide scales grown on ZrC. Full scale growth shown versus t and $t^{1/2}$. Individual layers shown for the rate law fit best. All trend lines constrained through the origin. Error bars represent one standard deviation.

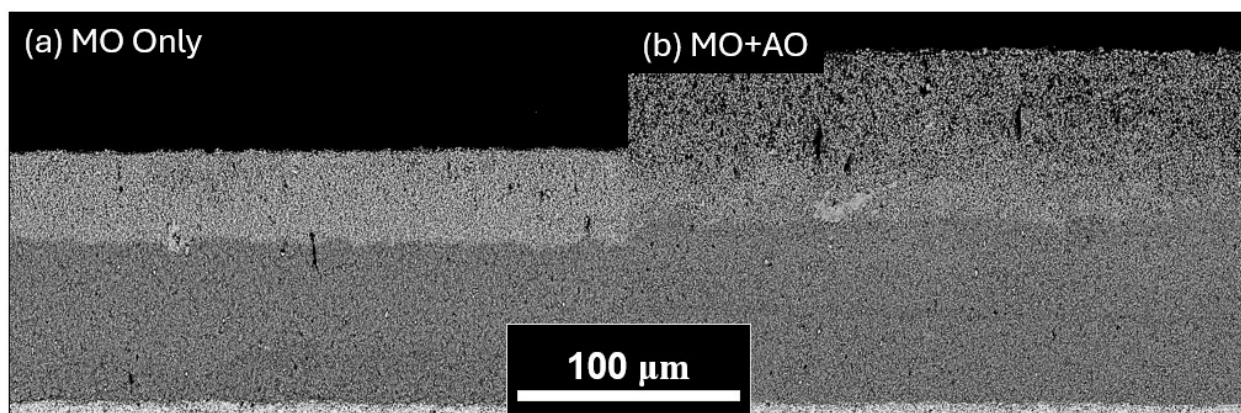


Figure 5.15: Backscatter cross-section SEM micrographs of ZrC oxidized in (a) MO and (b) MO+AO environments at 1600°C. A two-layered oxide scale is observed. MO gas is 1% O_2 -Ar, MO+AO gas is 0.7% O_2 -0.6%O-Ar

while the inner, carbon-rich layer thickness is approximately the same. Figure 5.16 shows polished, backscatter SEM micrographs of the oxide grown on ZrC after oxidation at 1800°C for 5 min in a MO only and a MO+AO environment. A single-layer oxide scale is visible in both images. The oxide scale is much thicker in the MO+AO environment than in the MO only environment.

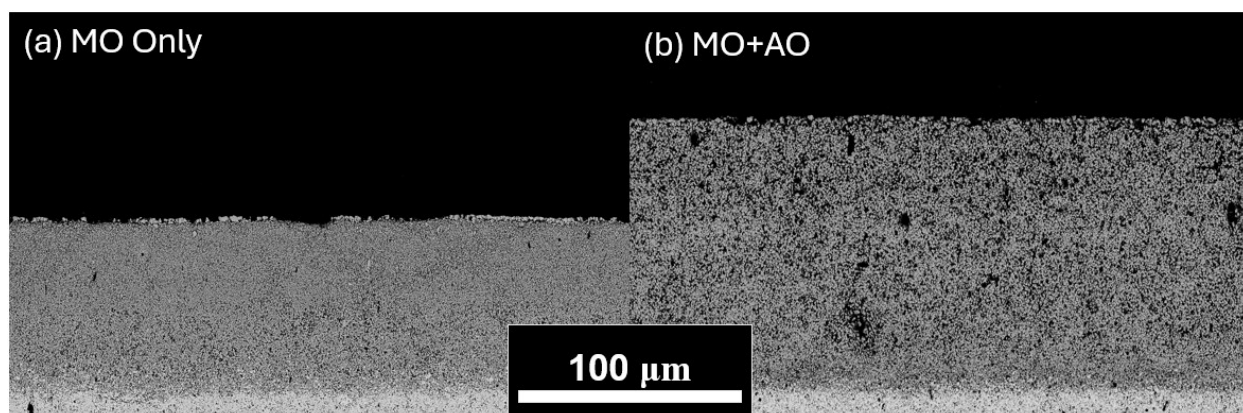
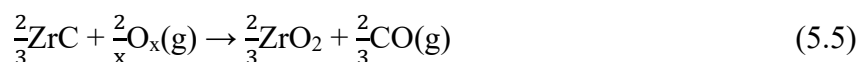


Figure 5.16: Backscatter cross-section SEM micrographs of ZrC oxidized in (a) MO and (b) MO+AO environments at 1800°C. Only a single-layered porous oxide scale is observed. MO gas is 1% O₂-Ar, MO+AO gas is 0.7%O₂-0.6%O-Ar

ii. Discussion

The oxidation kinetics shown in Figure 5.14 can be explained by the microstructures of the formed oxides. The outer oxide grows with linear kinetics because of the porous structure of the oxide, which allows rapid oxygen ingress through the layer (Table 2.3.2). The inner oxide layer is observed to grow with parabolic kinetics, indicating either gas-phase diffusion through a growing porous oxide (Table 2.3.3) or solid-state diffusion through a growing dense oxide (Table 2.3.4). The TEM/EDS data from Part 1 showed that the inner layer is a dense layer of ZrO₂+C, suggesting that this parabolic rate is driven by solid-state diffusion. The overall parabolic growth rate indicates that the overall oxidation rate is controlled by the growth of the inner layer.

Understanding that the inner layer is created by the preferential oxidation of Zr, the ZrC oxidation reactions in either MO or AO are listed below. Oxidation to form $\text{CO}_2(\text{g})$ is not considered here, as $\text{CO}(\text{g})$ formation was shown to be much more favorable in Part 1 (Figure 3.27).



Here, $x = 1$ or 2 for AO or MO, respectively. Thermodynamic equilibrium calculations were made using FactSage and the FactPS database [109] for each reaction. Following the predominance diagram shown by Scott, He, and Lipke for HfC [26], Gibbs free energy values were calculated via Equation (5.6) to determine the equilibrium constant as a function of temperature:

$$\Delta G = -RT \ln K \quad (5.6)$$

These calculations were then repeated, replacing $\text{O}_2(\text{g})$ with $2\text{O}(\text{g})$ to represent an AO containing environment. $2\text{O}(\text{g})$ was used to maintain the number of oxygen atoms participating in the reaction. The equilibrium constants will approximately be:

$$K \cong \frac{1}{P_{\text{O}_2}} \quad (5.7)$$

$$K \cong \frac{1}{P_{\text{O}}^2} \quad (5.8)$$

Assuming the $\text{CO}(\text{g})$ partial pressure is equivalent in each case. Figure 5.17 shows the calculated equilibrium constants for ZrC oxidation reactions as a function of temperature for both MO and AO environments. These graphs can be read as a phase diagram, indicating what the stable

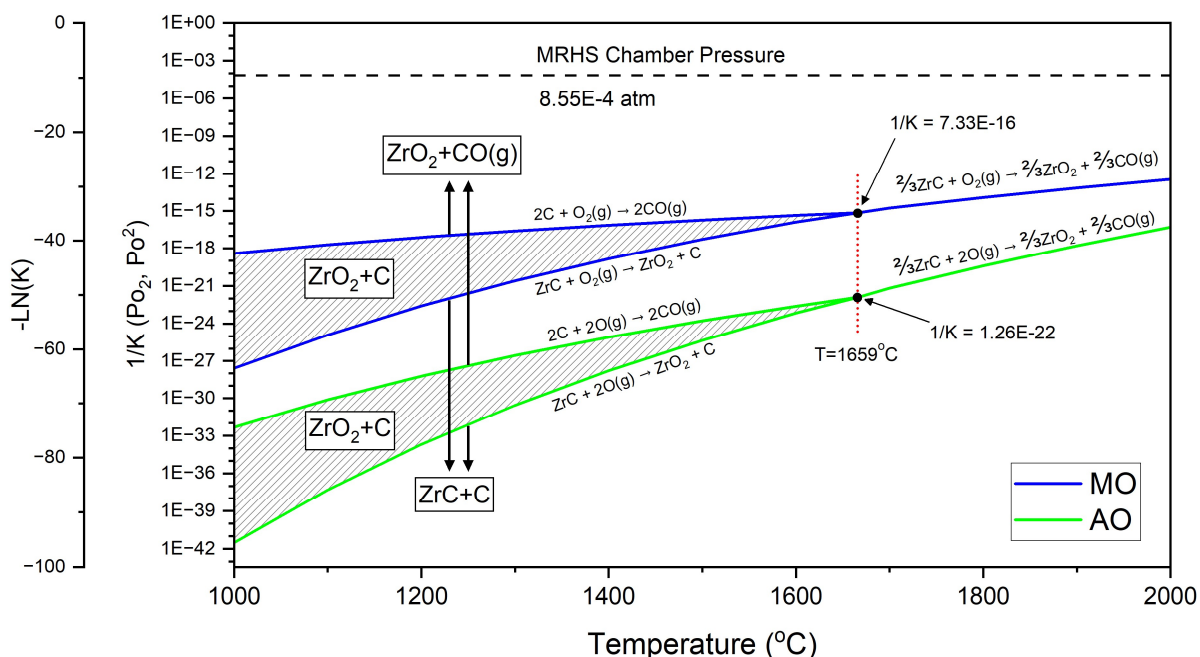


Figure 5.17: Calculated oxidation stability diagram for the $\text{ZrC} + \text{O}_2/2\text{O}$ system. The reactions marked for each line proceed at conditions above the line.

oxidation products would be at the given conditions. There are three regions for each system: 1) $\text{ZrC} + \text{C}$ is stable, no oxidation takes place; 2) $\text{ZrO}_2 + \text{C}$ is stable, only oxidation of Zr takes place; and 3) $\text{ZrO}_2 + \text{CO}(\text{g})$ is stable, carbon is oxidized to $\text{CO}(\text{g})$ and leaves the system. Above the temperature where the equilibrium constants intersect (1659°C), preferential Zr oxidation (region 2) is no longer stable, and oxidation of both Zr and carbon happens at all oxygen pressures above this temperature. The partial pressure of oxygen used for these experiments in the MRHS (1% O_2 at 65 torr total pressure) is also marked on the diagram by a horizontal dashed line.

The shape of Figure 5.17 greatly resembles the predominance diagram reported by Scott, He, and Lipke for the HfC system [26], and indicates that oxidation of ZrC is six orders of magnitude less stable in AO than MO environments. The greater reactivity of AO reduces the equilibrium partial pressure for the reaction using AO as an oxidant as compared to MO. The greater reactivity of AO drives further reaction with carbon at the interface between the carbon-rich and carbon-free oxide layers where the Po_2 would be too low in MO.

The inner layer growth is still governed by solid-state diffusion as shown in parabolic oxidation Figure 5.14. MO dissociation at the oxidation front (pre-requisite to oxidation) must be rapid, as oxidation reactions which are rate-limited by reactions grow with linear kinetics (Table 2.3.1). Solid-state diffusion occurs as the atomic species in either MO or AO, so the initial dissociation state of the oxygen does not affect transport through the diffusion-limited layer and the inner layer does not change thickness when introduced to AO. The effect of AO on the thicknesses of the oxide formed on ZrC is shown schematically in Figure 5.18.

The ZrC shown in Figure 5.16 was oxidized at 1800°C, which is above the temperature where the CO(g) formation is favored over free carbon formation (Figure 3.27 and Figure 5.17). According to the thermodynamic calculations, the temperature for CO(g) favorability is found to remain the same whether AO or MO is the oxidant. In this case, as discussed in Part 1, the inner, carbon-rich layer is no longer found in the oxide scale. The outer, carbon-free layer of the scale is

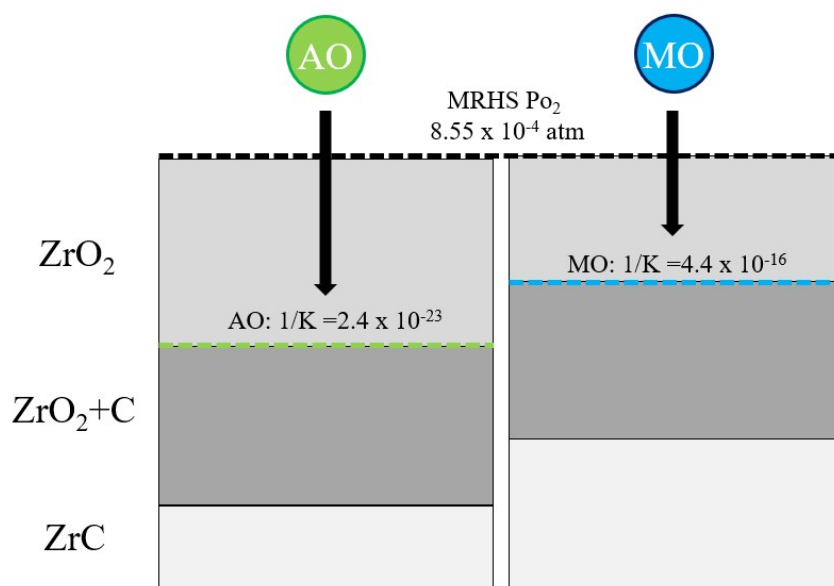


Figure 5.18: Schematic diagram of the effect of AO reactivity on ZrC oxidation. Diffusivity through the scale layers will be approximately equal, but the increased reactivity of AO progresses the reaction of carbon to CO(g) which would be in equilibrium in MO. The thickness of the outer ZrO₂ layer is increased in AO, while the inner layer thickness is unchanged. Greater carbide recession is observed in AO.

highly porous. Thus, the removal of a diffusion-limiting layer from the oxide scale allows rapid oxygen ingress to the underlying material resulting in increased oxidation rates. AO has a direct path to the underlying ZrC, which has significantly increased reactivity with AO as described in Figure 5.17. The micrographs shown in Figure 5.16 clearly indicate a thicker oxide scale after 5 min of oxidation at 1800°C in MO+AO environments (137.3 μm) over MO only environments (88.4 μm) because of the lack of the inner, carbon-rich layer to act as a diffusion barrier.

g. Oxidation of Hf in Atomic Oxygen

a. Results

Hf was oxidized at 1600°C for 2, 5, and 7 min in 1% O₂ – bal. Ar MO only and MO+AO environments. The oxide growth is plotted versus time in Figure 5.19. For MO only exposures, the oxide growth rate is highly linear with respect to time. In MO+AO oxidation, the oxide grows

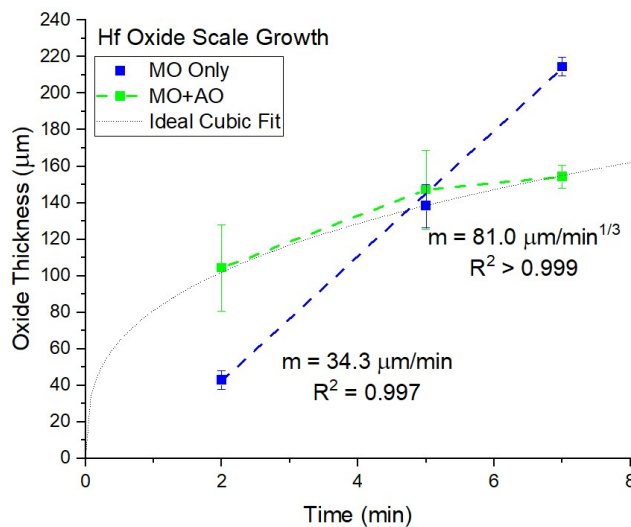


Figure 5.19: Total oxide growth rate for Hf exposed to 1600°C in MO only and MO+AO environments. Error bars represent one standard deviation.

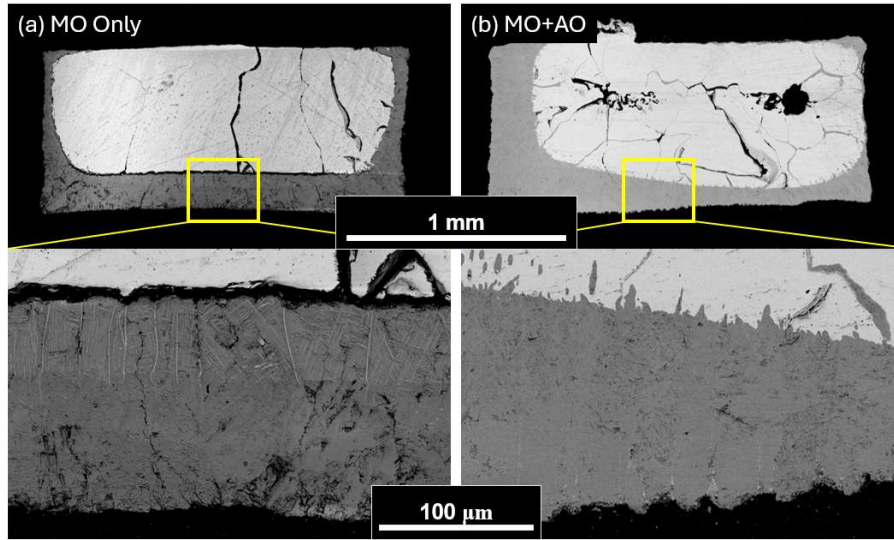


Figure 5.20: Backscatter SEM micrographs after Hf oxidation at 1600°C for 5 min in (a) MO only and (b) MO+AO environments. Bottom row is higher magnification of the oxide scales. Cracking can be seen in the Hf metal. Less cracking is observed in the MO only case, but the oxide has completely delaminated from the metal across the width of the sample.

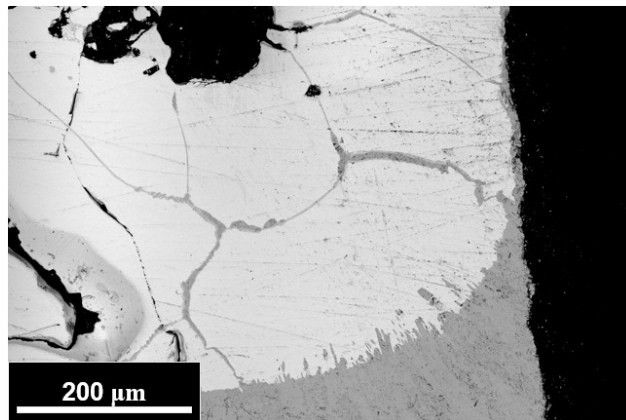


Figure 5.21: Backscatter SEM micrographs after Hf oxidation at 1600°C for 5 min in an MO+AO environment showing grain boundary or crack oxidation throughout the metal.

according to a cubic rate law. An ideal cubic growth rate is also plotted on the oxide scale plot, for reference. Oxide thickness at short times (2 min) is significantly thicker in MO+AO exposures, whereas oxide thickness at longer times (7 min) is significantly thicker in MO only exposures.

The same oxidation products were observed as in Part 1: a HfO_2 scale which contains cracked oxide and/or a two-phase $\alpha\text{-Hf}+\text{HfO}_2$ layer. Example microstructures are shown in Figure 5.20. The two-phase region is observed here to grow in MO only exposures. In MO+AO exposures,

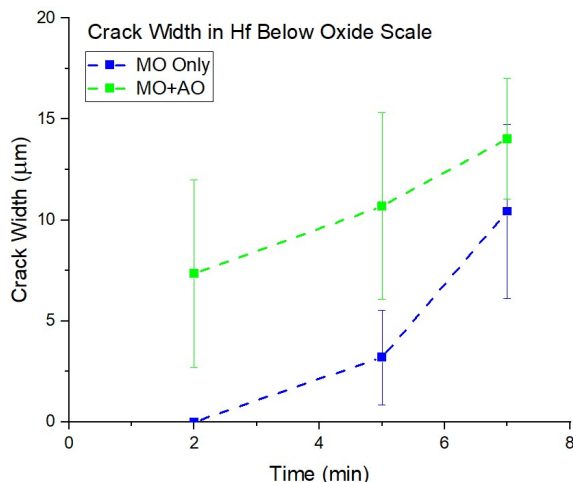


Figure 5.22: Crack width in the Hf after exposure to 1600°C in MO only and MO+AO environments. Error bars represent one standard deviation.

the oxide is uniformly HfO_2 . The oxide scale is generally adherent, but is sometimes observed to have delaminated from the underlying Hf. Cracking in the Hf substrate is also observed. In MO+AO exposures oxide is found filling some of the cracks throughout the bulk Hf, shown in Figure 5.21 indicating the cracks were present at the exposure temperature. Crack width growth versus time is shown in Figure 5.22 to follow similar kinetics in MO only and MO+AO exposures, though the average width in MO+AO is slightly larger than the average in MO only. In cases where MO only crack width exceeded MO+AO crack width, the oxide scale is also found to have delaminated from the metal.

b. Discussion

As previously noted in Part 1, the oxidation behavior of Zr and Hf are similar. The oxide growth rates follow identical kinetic trends to Zr oxidation in MO only versus MO+AO environments: Hf oxidation was post-breakaway onset in MO only exposures and pre-breakaway onset in MO+AO exposures for the oxidation times used in this study. The cubic growth rate law

exhibited by oxidation in MO+AO environments indicates that the oxide growth rate is driven by either grain growth in the oxide scale [140], [141] or stress gradients in the oxide scale [69], [142]. No evidence for grain growth in the oxide scale is observed, leading to the hypothesis that a reduction in the oxide stress gradient may be responsible for the cubic oxidation rate and for the change in breakaway behavior.

The crack width measurements made in the Hf beneath the oxide scale yield similar, but less clear, trends as were found in Zr. Cracking in MO+AO experiments was consistently higher than in MO only experiments, though the differences are statistically not significantly different. After oxidation at 5 min, in MO+AO the oxide thickness is shown in Figure 5.19 to be very similar, so differences in crack width are not solely due to oxide thickness. Thus, it is hypothesized that the Hf oxidized in MO+AO environments is cracking at earlier times due to increased embrittlement of the Hf metal at high temperature and dissolved oxygen content. This provides stress relief to the oxide and prevents breakaway oxidation. In MO+AO, oxide can be seen filling the cracks in the Hf substrate in Figure 5.21. Upon formation of the oxide in the cracks, the corresponding volume expansion may also help alleviate stresses in the oxide scale. In Figure 5.20, the oxide grown on Hf after 5 min exposure to MO only is shown to be completely delaminated across the width of the sample. This is another form of stress relief for the oxide and may explain the decreased crack width of the Hf at those conditions. While these observations align with the presented hypothesis, computational or experimental evidence of stress states in the substrate and oxide is needed to support this mechanism.

h. Oxidation of HfC with Excess Carbon in Atomic Oxygen

a. Results

HfC was oxidized at 1600°C for 2, 5, and 7 min in MO only and MO+AO environments. Figure 5.23a and b show polished, backscatter micrographs of examples of HfC+C oxidized at 1600°C in MO only and MO+AO, respectively. The darker areas throughout the base material are the aforementioned excess free carbon, occupying approximately 42.5 vol% of the bulk HfC+C. The darker areas in the oxide scale are voids filled with epoxy which were created by oxidation of the excess carbon. A two-layered oxide scale is observed, as previously described in Part 1. The outer layer is the carbon-free HfO₂ layer and the inner layer is the carbon-rich HfO₂+C layer. The inner layer has a non-uniform thickness across the length of sample, as similarly seen in Part 1.

Figure 5.24 shows the growth kinetics of the individual oxide layers and of the full oxide scale. Kinetic measurements were made on areas of the sample which are largely HfC and which have intact oxide scales. The outer scale can be fit to either a linear or parabolic growth rate versus

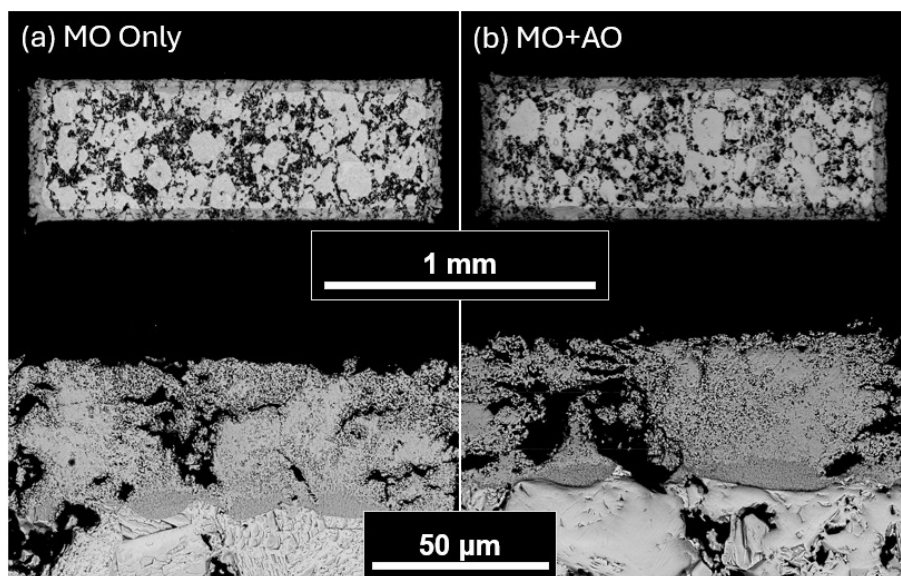


Figure 5.23: Backscatter cross section micrographs of HfC+C samples post-oxidation at 1600°C for 7 min. The dark patches throughout the sample are excess carbon. The bottom row of images are higher magnification micrographs of the above samples.

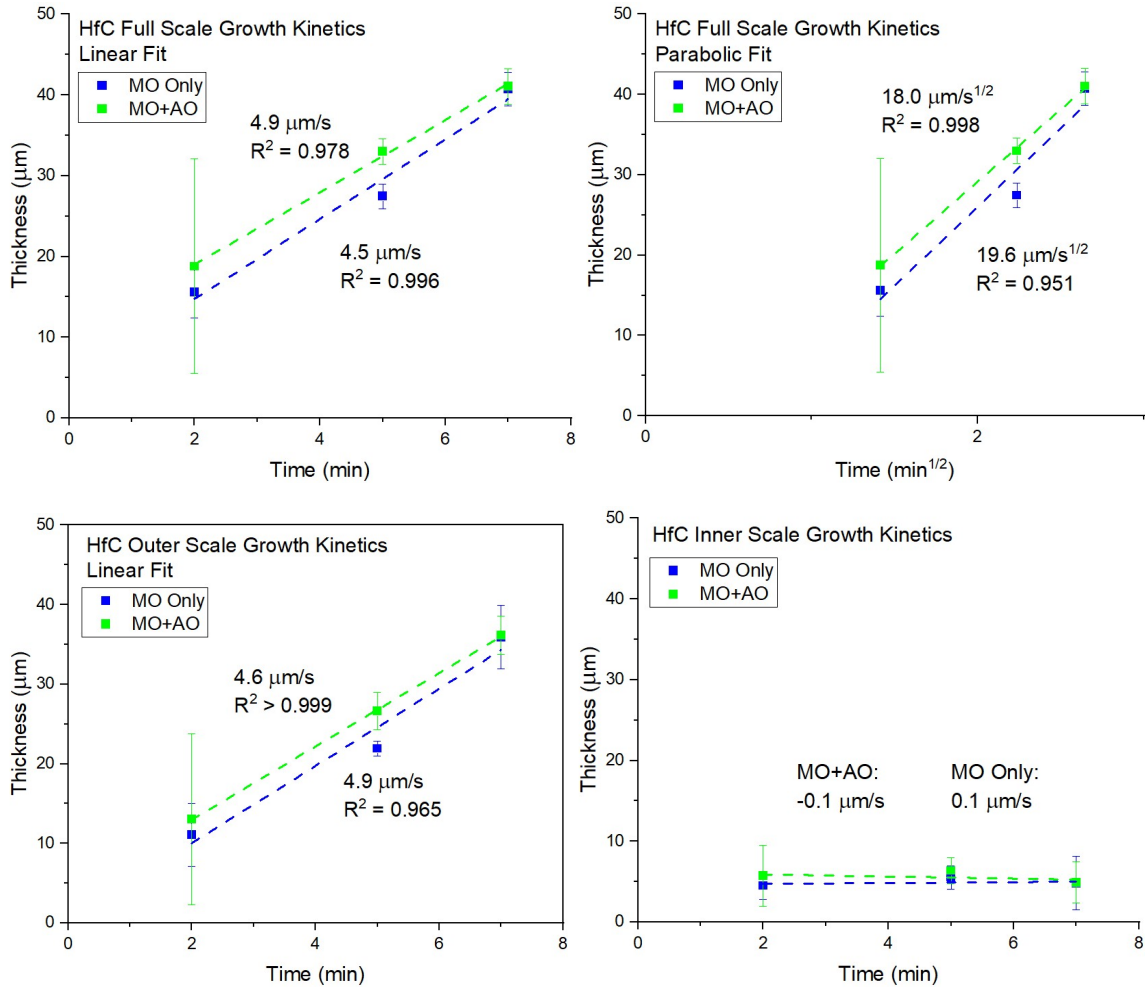


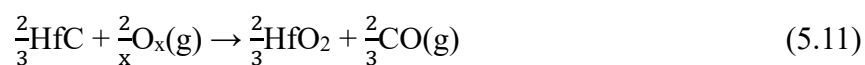
Figure 5.24: Oxidation kinetics of HfC at 1600°C in MO only and MO+AO environments. Kinetics shown for (top left) the full scale versus t , (top right) the full scale versus $t^{1/2}$, (bottom left) the outer scale versus $t^{1/2}$, and (bottom right) the inner scale versus t .

time. The inner scale is shown to have a nearly constant thickness throughout the measured oxidation durations, about $5.3 \pm 0.9 \mu\text{m}$ thick. The overall scale growth rate is found to be best described as parabolic. The thickness of all layers is measured to be slightly thicker in MO+AO environments than in MO only environments, but there is very little difference between these measurements. All data points are within one standard deviation of one another, and no significant difference between the oxide growth rates in MO only and MO+AO environments is observed.

b. Discussion

The overall scale growth rate following a parabolic trend follows most literature reports for HfC oxidation kinetics [17], [24], [27], [80], [81]. The oxide scale is very porous, so a parabolic oxidation rate would be due to gas-phase diffusion through a growing porous oxide (Table 2.3.3). Following a parabolic oxidation rate, the measured oxidation rate of $18.0 - 19.2 \mu\text{m}/\text{min}^{1/2}$ is in excellent agreement with recent oxidation data and models for the oxidation of stoichiometric HfC [80], despite the high carbon content of the material. However, the oxide microstructure shows large voids and the defects in the scale. These features would ordinarily suggest that oxidation should follow a linear rate (Table 2.3.2), similar to the linear oxidation rates observed for oxidation of TaC to form Ta_2O_5 containing large voids. A linear rate is in better agreement with the results presented in Part 1. The oxidation rate shown in Figure 3.33 was approximately $6.3 \mu\text{m}/\text{s}$. The average growth rate found here $4.7 \mu\text{m}/\text{s}$ is slightly lower than what was observed in Part 1, consistent with the lower flow rate of oxygen between these studies (1000 sccm in Part 1, 100 sccm in Part 3). The limited data with large uncertainty prevent a conclusive determination of the oxidation kinetics rate law.

A similar oxidation stability diagram as shown for ZrC is shown in Figure 5.25 for HfC after the example put forth by Scott, He, and Lipke [26]. The following reactions were used to calculate stability use Equation 5.6:



Because of the similar shape of the stability diagram to ZrC and the similarities between ZrC and HfC previously discussed, the changes in oxidation behavior between MO only and MO+AO environments for HfC were expected to be similar to those reported previously for ZrC. Therefore, a significant increase in the thickness of the outer, porous oxide scale was expected for HfC oxidation in MO+AO.

However, no change in the thickness of the oxide layers is observed for HfC+C between the MO only and MO+AO environments. This was expected for the inner layer thickness because this layer is reported to grow via solid-state diffusion (Table 2.3.2) and diffusivities of oxygen through the scale are not dependent on the dissociation state of the gas. The relatively constant outer layer thickness in the presence of AO was unexpected. The thermodynamic predictions are therefore inappropriate for the material containing excess carbon used here. As previously discussed for TaC oxidation, observations of increased AO reaction with grain boundaries was

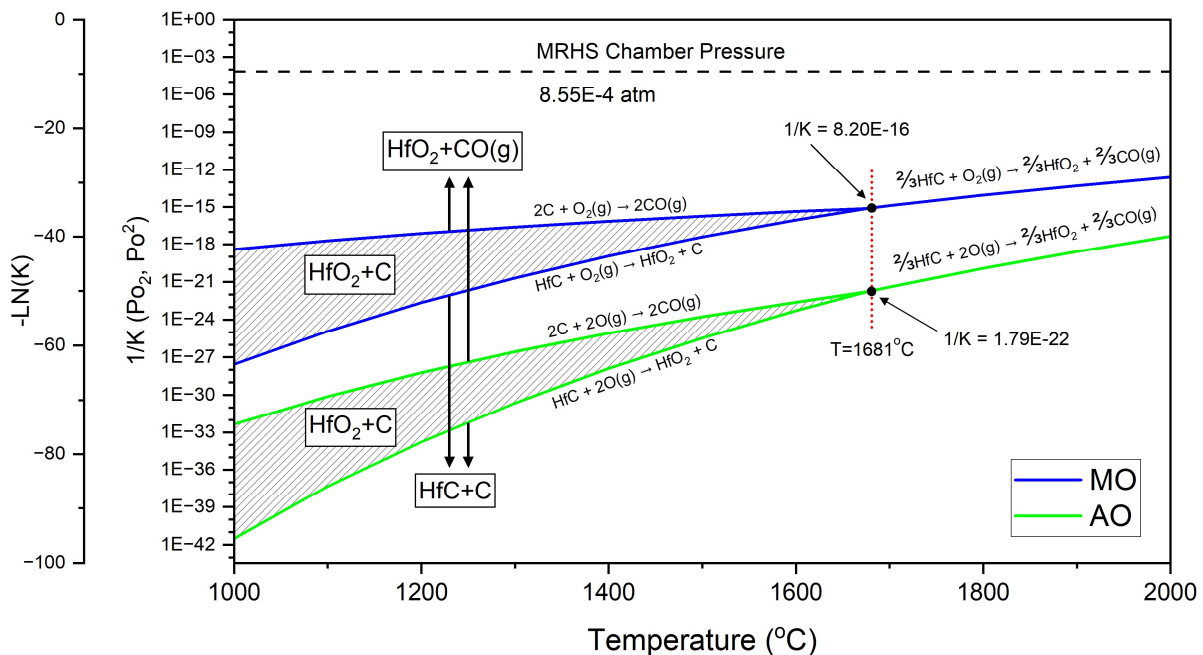


Figure 5.25: Calculated oxidation stability diagram for the HfC + O₂/2O system. The reactions marked for each line proceed at conditions above the line.

attributed to preferential reaction with high energy sites. Given the high carbon activity in the

HfC+C system, it is also possible that the AO may be preferentially reacting with the large carbon deposits, changing the outcome of the oxidation as compared to expectations for pure HfC. The total oxide thicknesses grown on HfC from Part 1 are compared to the HfC+C results in Figure 5.26. The purer HfC material shows a greater oxide growth rate than the HfC+C material, even without AO. This could either be the result of the excess carbon consuming oxygen and slowing oxidation in the HfC+C, or it could be due to the higher flow rate of oxygen used in Part 1 to study the HfC. This shows the importance of one-to-one comparisons in identifying the correct high temperature oxidation mechanisms.

While these results may not provide a very clear indication of the oxidation behavior of HfC in AO, it does indicate that material phase assemblage plays a large role in determining AO oxidation behavior. Materials with more than one primary constituent, such as composites, where the activity of constituents are changed may experience a greater AO attack on one constituent over another. For example, exposing composites materials, such as C-SiC or ZrB₂-SiC, to AO may

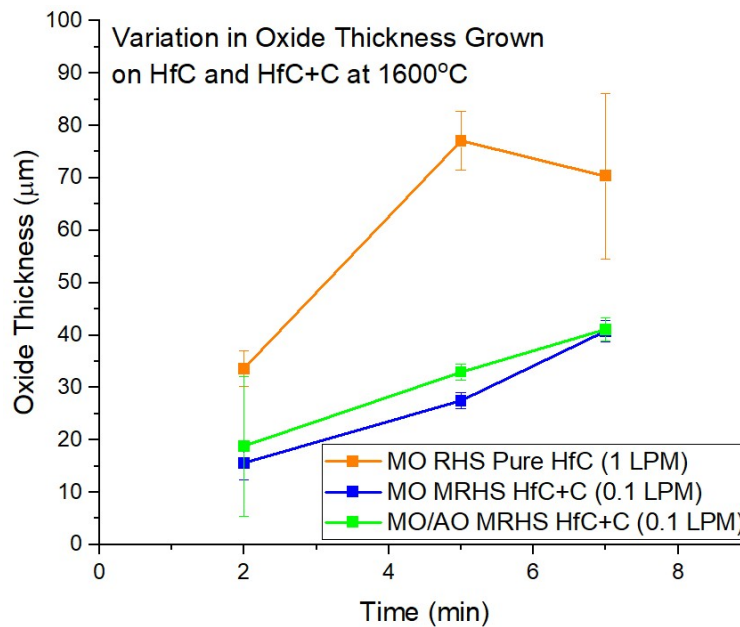


Figure 5.26: Comparison of HfC oxidation (Part 1) to HfC+C oxidation (Part 3). Both variation in oxygen flow rate or material purity could be responsible for the observed differences.

result in enhanced oxidation of one of the constituent materials over another. Significantly more work is needed to advance the understanding of AO oxidation on multi-phase materials.

i. Conclusions

The oxidation of M and MC (M = Zr, Hf, Ta) in atomic oxygen (AO) containing environments has been explored using a novel microplasma-equipped resistive heating system (MRHS). The results from Part 1 were used as a baseline understanding for the oxidation behavior of these materials in molecular oxygen (MO). Summarized, it was found that the effects of AO are as follows:

- 1) Enhanced AO adsorption on metal surfaces increases the amount of oxygen dissolved in the metal surface at early oxidation times. In MO, dissociation followed by dissolution of interstitial oxygen into the material is the rate limiting step during oxidation and oxide growth is delayed while the material reaches the solubility limit. In AO, surfaces saturate with interstitial oxygen more quickly and oxide growth begins earlier. This can cause significantly earlier onset for oxide growth as compared to oxidation in MO for materials such as Zr and Hf which have a high oxygen solubility. In addition, more rapid embrittlement from oxygen dissolution and resultant cracking of the underlying metals affects stress states at the metal/oxide interface.
- 2) AO greatly increases the oxidation rate of materials which exhibit linear oxidation kinetics, i.e. the rate-limiting step is gas-phase diffusion through an oxide scale with large defects. This implies while AO is diffusing through such a scale, it does not appreciably exchange

with the oxide or recombine with other AO atoms to form MO. For example, the oxide growth rate on Ta increased by orders of magnitude when AO was introduced.

- 3) AO will prefer to react with sites in the material that are higher energy than the bulk substrate surface. For example, in TaC, preferential grain boundaries oxidation was enhanced when AO was used as the oxidant.
- 4) For layers which are governed by parabolic growth kinetics, i.e. the rate-limiting step is solid-state diffusion through a dense oxide scale, oxidation rates are not significantly affected. For example, the thickness of the dense inner oxide layer grown on ZrC was shown to not change when AO was introduced, while the porous outer oxide layer grew appreciably.

j. Future Work

Similar to Part 1, this work would benefit tremendously from additional data to more concretely understand the oxidation behavior of the studied materials. Oxide growth induced stresses should also be analyzed to understand how AO affects the inconclusive change in mechanism observed in Zr and Hf. Reducing the partial pressure of oxygen to further slow oxidation would also help more accurately identify features which were overlooked in this study because of rapid oxidation rates.

Following the desired future work from Part 2, variation of the dissociation fraction of oxygen during these oxidation studies would also provide additional insight into how oxidation mechanisms may change in different hypersonic flight trajectories.

This work represents an initial attempt to understand how AO affects the oxidation behavior of materials which could be used as constituents in materials design for hypersonic vehicles. Significantly more work investigating the AO oxidation behavior of hypersonic-relevant materials should be investigated, including ZrB₂-SiC and C-C composites.

Overall Impact of this Work

The first goal of this work was to identify the effects of carbon on oxidation mechanisms by comparing oxidation of transition metals and metal carbides to address a long-standing knowledge gap in high temperature oxidation science. The first impact this work has is bringing to light the complexity of the oxidation reaction with carbon. The effect of carbon on the oxidation mechanism is not simply that a porous scale is formed. Rather, the addition of carbon to a transition metal carbide affects the oxidation rate through its impact on both the substrate and the oxide. In the substrate, carbon can affect the melting temperature, oxygen solubility, stiffness, and drive grain boundary oxidation. In the oxide, carbon can create pores, form additional layers, and improve the oxide's ability to withstand growth stresses. These factors can completely change the oxidation mechanism as compared to its complementary transition metal. In this regard, we show here that the formation of a porous scale during oxidation is not always deleterious, and that the effects that oxidation may have on a carbon-containing material are complex. This work aims to aid oxidation-resistant materials design for high temperature environments, adding one-to-one kinetic and mechanistic oxidation comparisons to the toolset of materials designers.

Secondly, this work is also a response to the rapidly developing field of hypersonic materials. Many researchers are restricted in their ability to study the hypersonic environment because of the high cost of arc-jets, plasmotrons, or other similar facilities. To effectively identify potential candidate materials for this application, as well as study the fundamental behavior of materials in such environments, new tools allowing for lower cost and higher throughput materials evaluation are needed. The construction of a new resistive heating system capable of isolating dissociated oxygen as an environmental variable during high temperature oxidation is unprecedented and presents a new direction for materials qualification in a hypersonic

environment. However, atomic oxygen is also found in other environments, including low earth orbit and fusion reactors. With this system operational, doors may be opened for many other researchers to evaluate the oxidation behavior of more materials in atomic oxygen. As shown in Part 3 of this work, the effects of AO are complex. Complete changes in oxidation mechanisms may be observed which could catastrophically affect the underlying material. This work represents a first step in addressing the immense lack of fundamental understanding of oxidation mechanisms in atomic oxygen containing environments.

Publication Status of this Work

As of writing this dissertation, the following journal articles are planned to be published in the near future:

- Stephens, C. J., Donaldson, S. K., Richwine, M. N., Recupero, C. J., Opila, E. J. (2025). Oxidation Mechanisms of Tantalum in High Temperature Molecular and Dissociated Oxygen. *Submitted to Materialia 2025, Under Revision.*
- Stephens, C. J., Recupero, C. J., Heinrich, H.H., Opila, E. J. (2025). Thermal Oxidation of ZrC and HfC in High Temperature Atomic Oxygen. *In Preparation.*
- Stephens, C. J., Richwine, M. N., Zhou, C., Opila, E. J. (2025). The Oxidation of Ta and TaC in High Temperature Molecular and Atomic Oxygen. *In Preparation.*
- Stephens, C. J., Recupero, C. J., Richwine, M. N., Heinrich, H. H., Zhou, C., Opila, E. J. (2025). The Role of Carbon in the Oxidation Mechanisms of Select Transition Metal Carbides. *In Preparation*

Appendix A: Additional Micrographs

To keep this dissertation concise, the data collected from thousands of micrographs was condensed into the work presented. However, it is the opinion of the author that having additional micrographs will greatly aid in understanding this work. As such, select micrographs are presented here which can serve as visual aid for the oxidation results in Parts 1 and 3.

- Additional Micrographs from Part 1:
 - o Oxidation of Ta and TaC

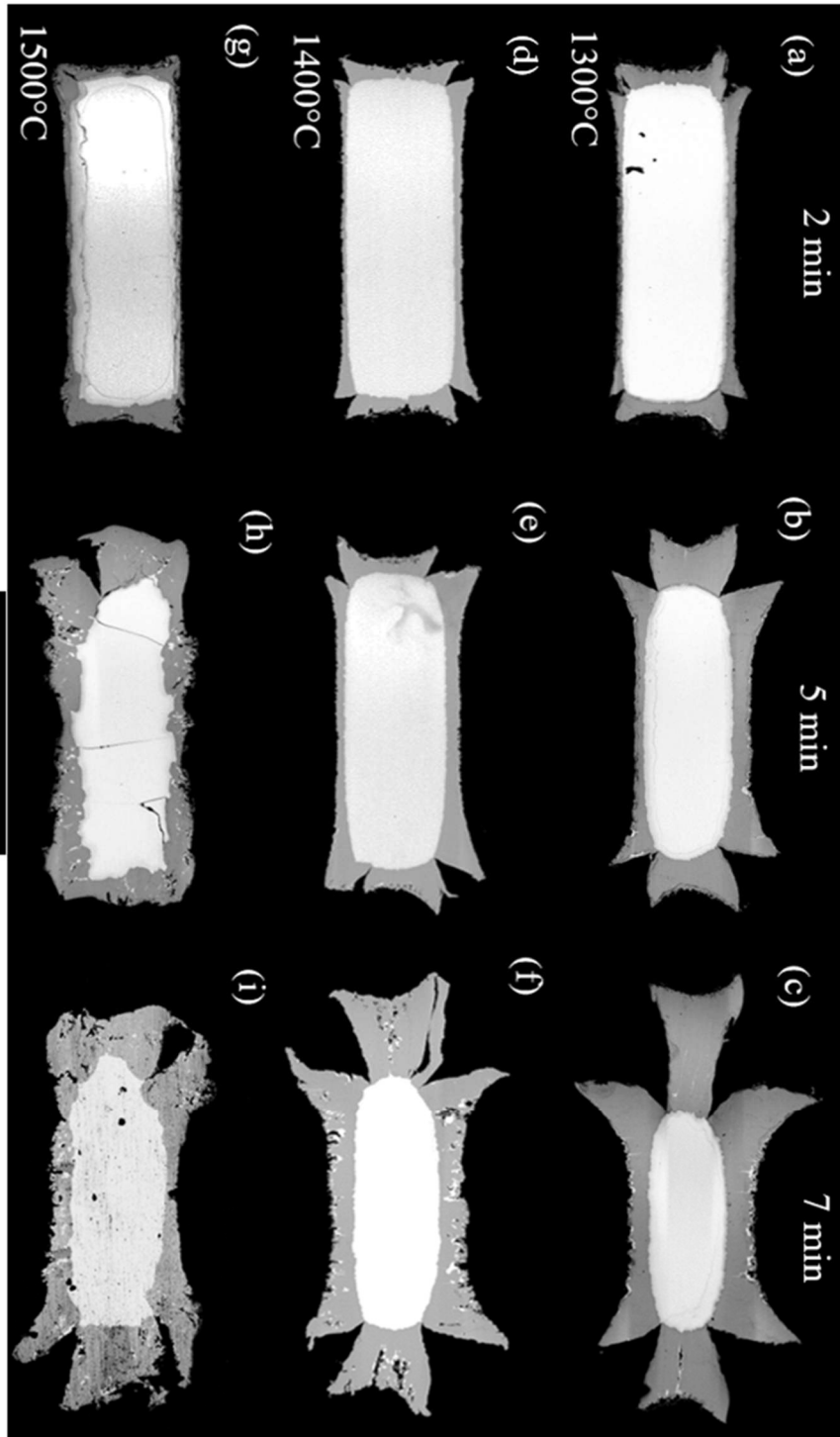


Figure A.1: Backscatter SEM polished cross section micrographs of Ta post-oxidation. Samples oxidized at (a-c) 1300°C, (d-f) 1400°C, and (g-i) 1500°C for (a,d,g) 2 minutes, (b,e,h) 5 minutes, and (c,f,i) 7 minutes. All samples oxidized in 1% O₂ – Ar.

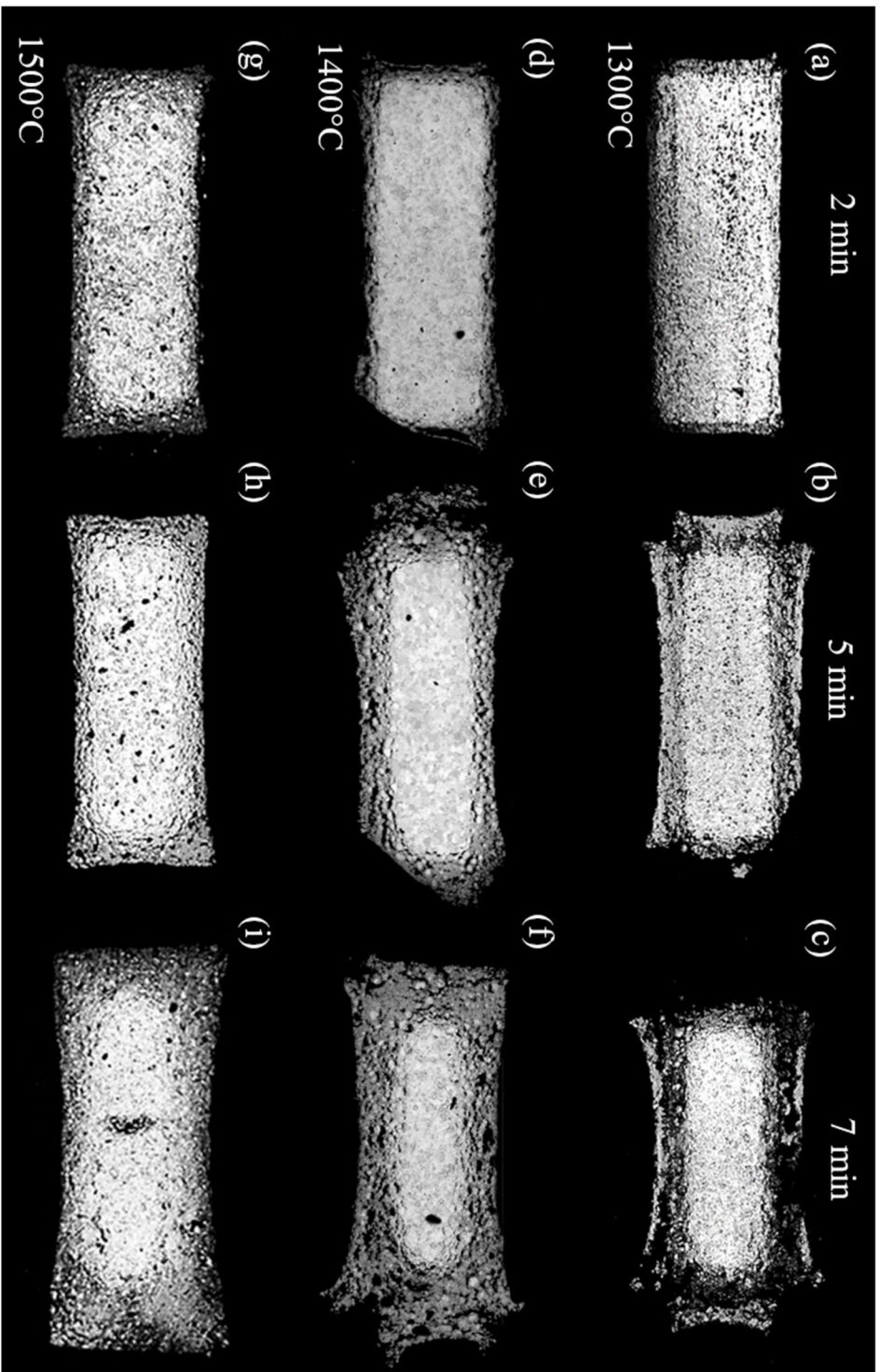


Figure A.2: Backscatter SEM polished cross section micrographs of TaC post-oxidation. Samples oxidized at (a-c) 1300°C, (d-f) 1400°C, and (g-i) 1500°C for (a,d,g) 2 minutes, (b,e,h) 5 minutes, and (c,f,i) 7 minutes. All samples oxidized in 1% O₂-Ar.

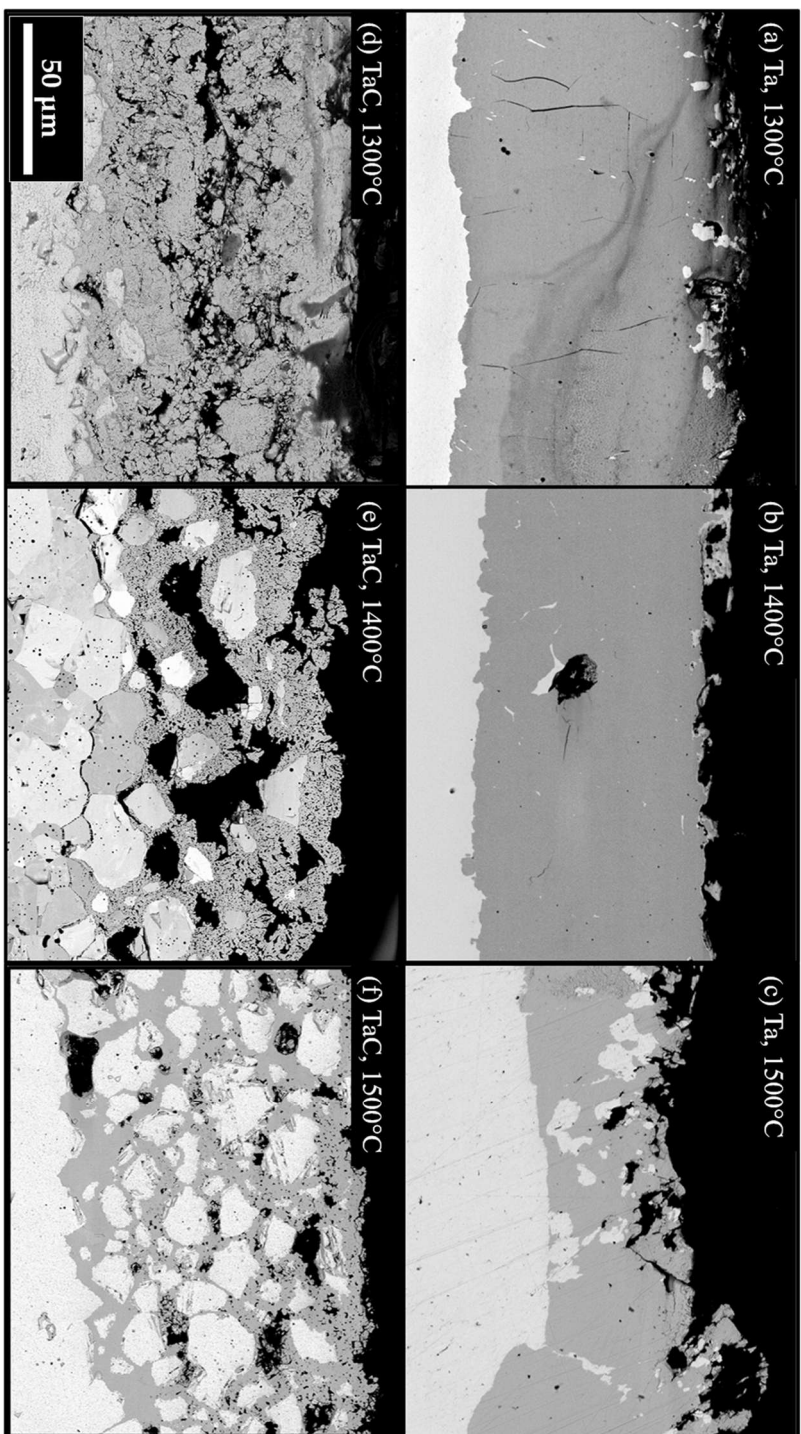


Figure A.3: Polished oxide cross sections for (a-c) Ta and (d-f) TaC after oxidation for 5 minutes in 1%O₂-Ar.

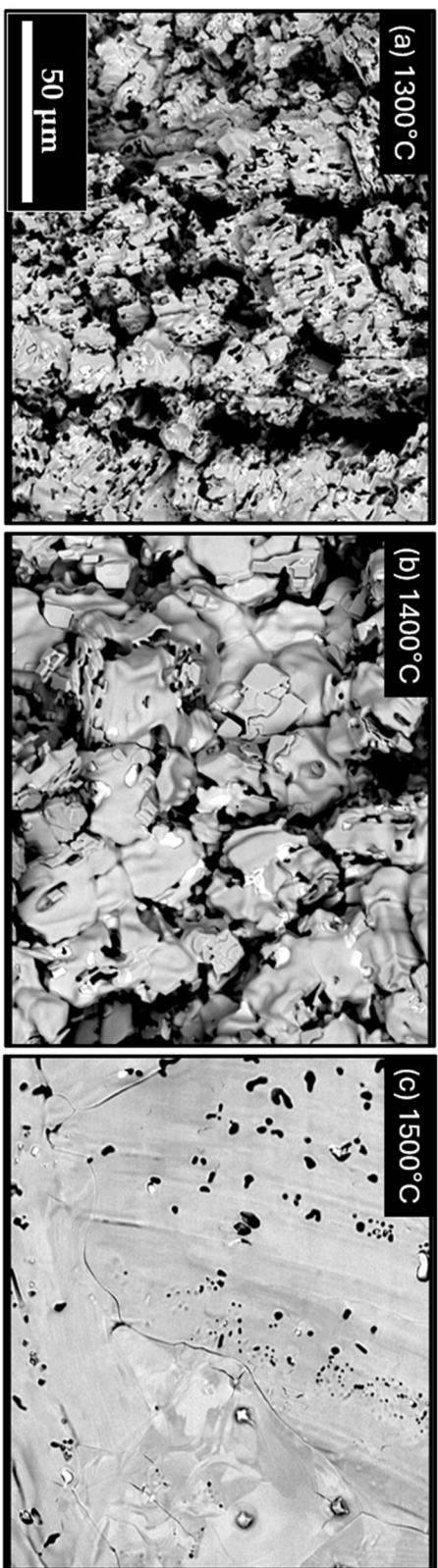


Figure A.4: Backscatter SEM micrographs in plan view of the oxide grown on Ta for 5 minutes in 1%O₂-Ar.

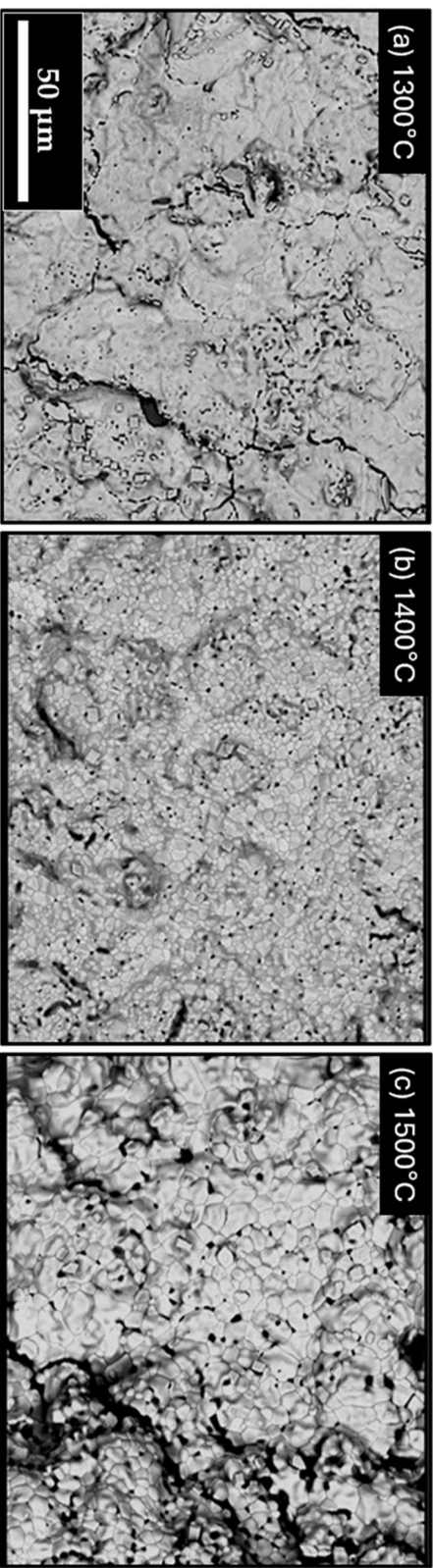


Figure A.5: Backscatter SEM micrographs in plan view of the oxide grown on TaC for 5 minutes in 1%O₂-Ar.

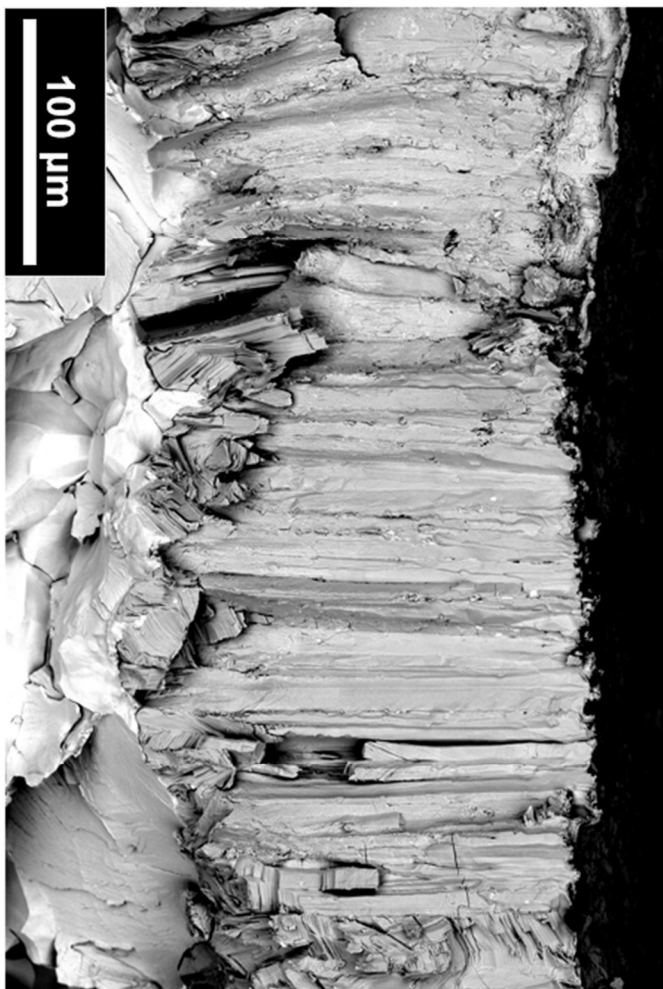


Figure A.6: Fracture section of Ta oxidized at 1300°C for 7 min, showing that the oxide grows completely columnar.

- Oxidation of Zr and ZrC

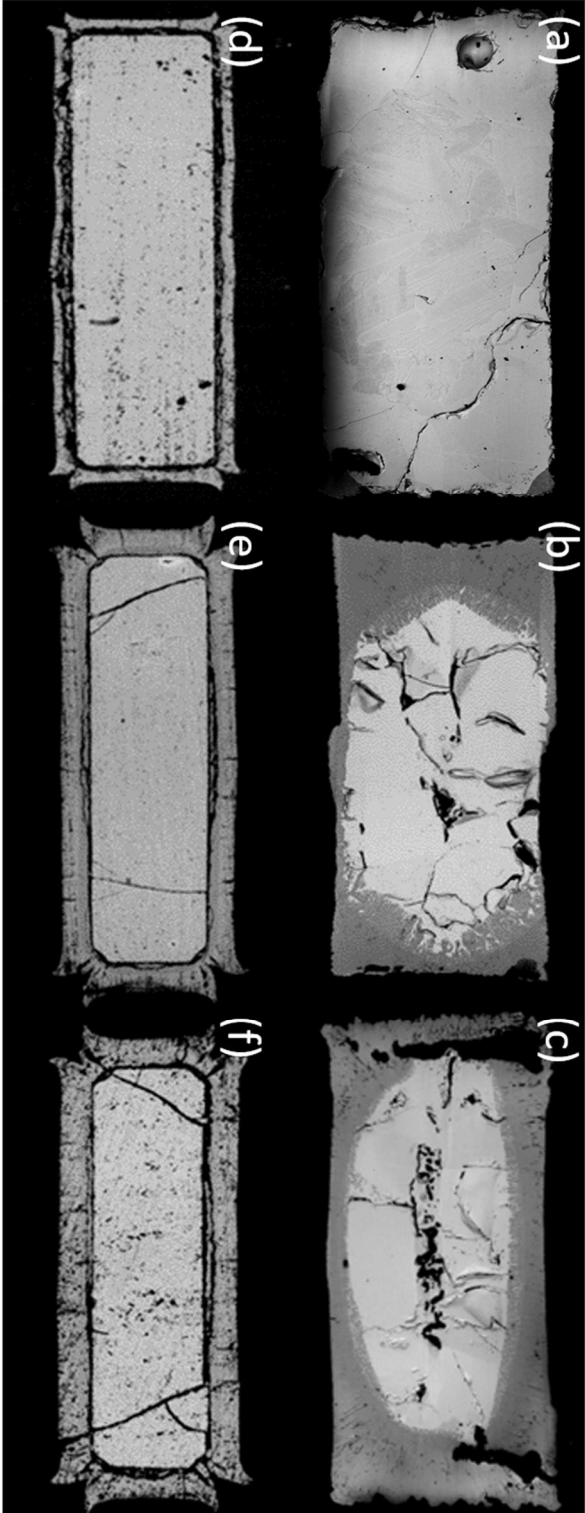


Figure A.7: Polished cross section backscatter micrographs of Zr (top row) and ZrC (bottom row) after (a,d) 2 min, (b,e) 5 min, and (c,f) 7 min exposure times at 1400°C in 1%O₂-Ar.

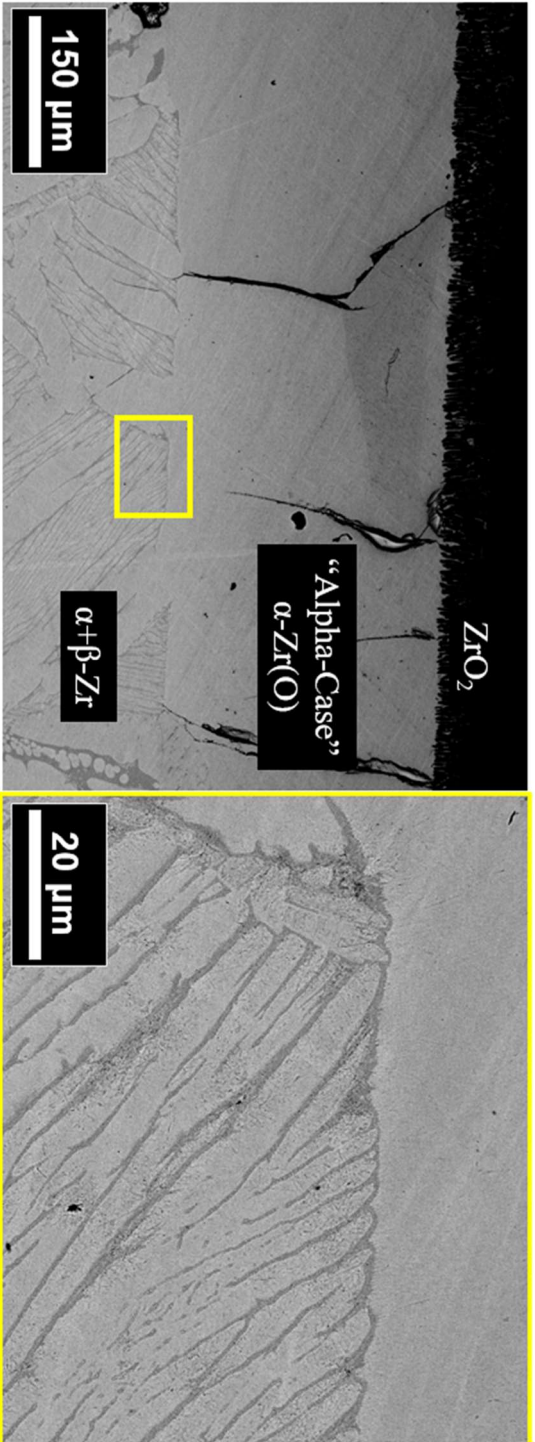


Figure A.8: Polished cross section backscatter micrographs of Zr after 5 min exposure at 1400°C in 1%O₂-Ar. The two-phase α+β-Zr region observed deep into the metal and is shown in better clarity on the right.

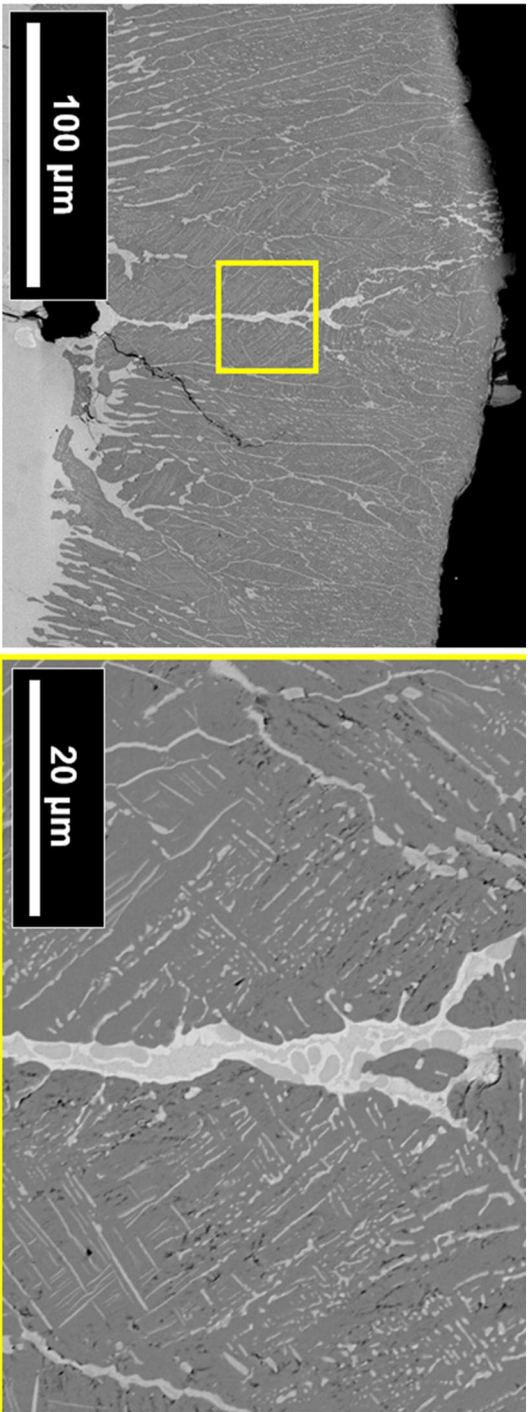


Figure A.9: Polished cross section backscatter micrographs of Zr after 10 min exposure at 1400°C in 1%O₂-Ar. The two-phase α-Zr(O)+ZrO₂ region observed in the oxide is shown in better clarity on the right.

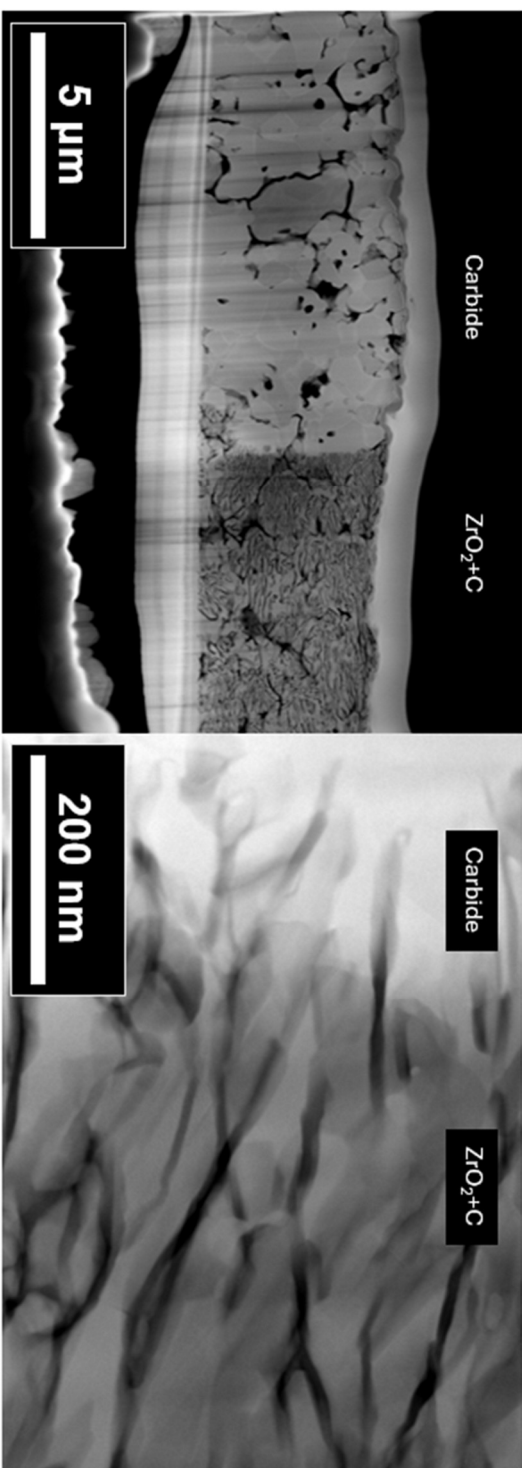


Figure A.10: TEM micrographs of a FIB liftout taken from the carbide/oxide interface of ZrC oxidized at 1600°C for 7 min.

○ Oxidation of Hf and HfC

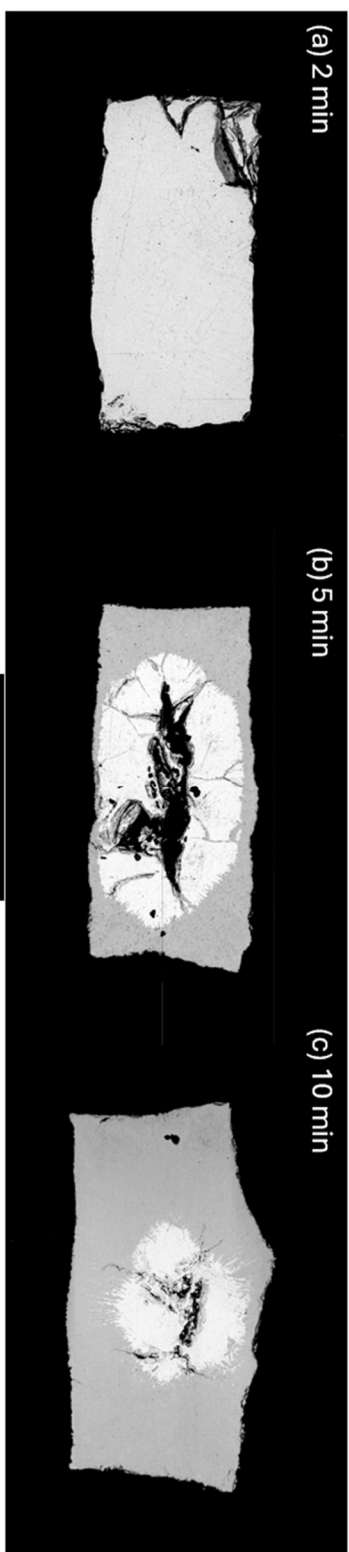


Figure A.11: Backscatter SEM micrographs of Hf oxidized at 1600°C for 2, 5, and 10 min in 1% O₂ – Ar.

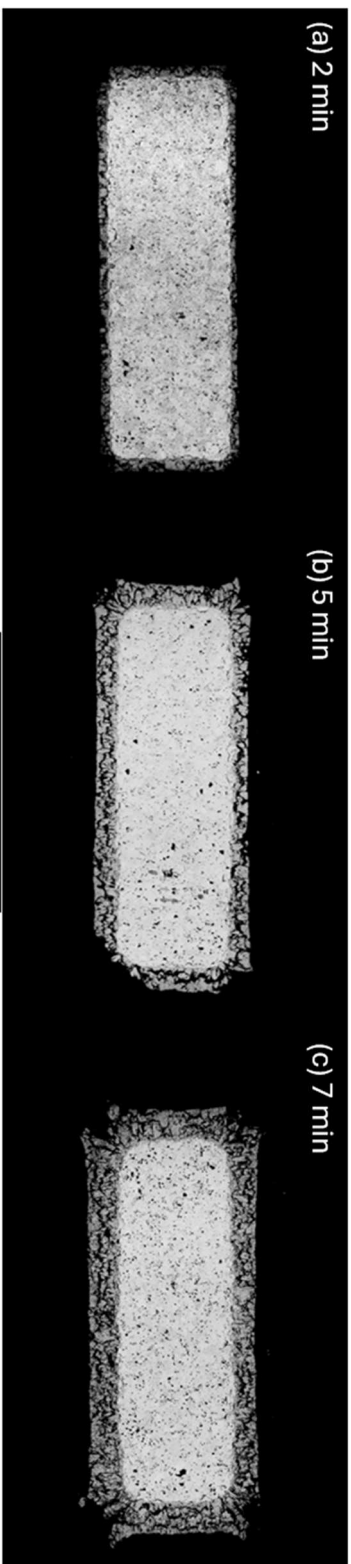


Figure A.12: Backscatter SEM micrographs of HfC oxidized at 1600°C for 2, 5, and 7 min in 1% O₂ – Ar.

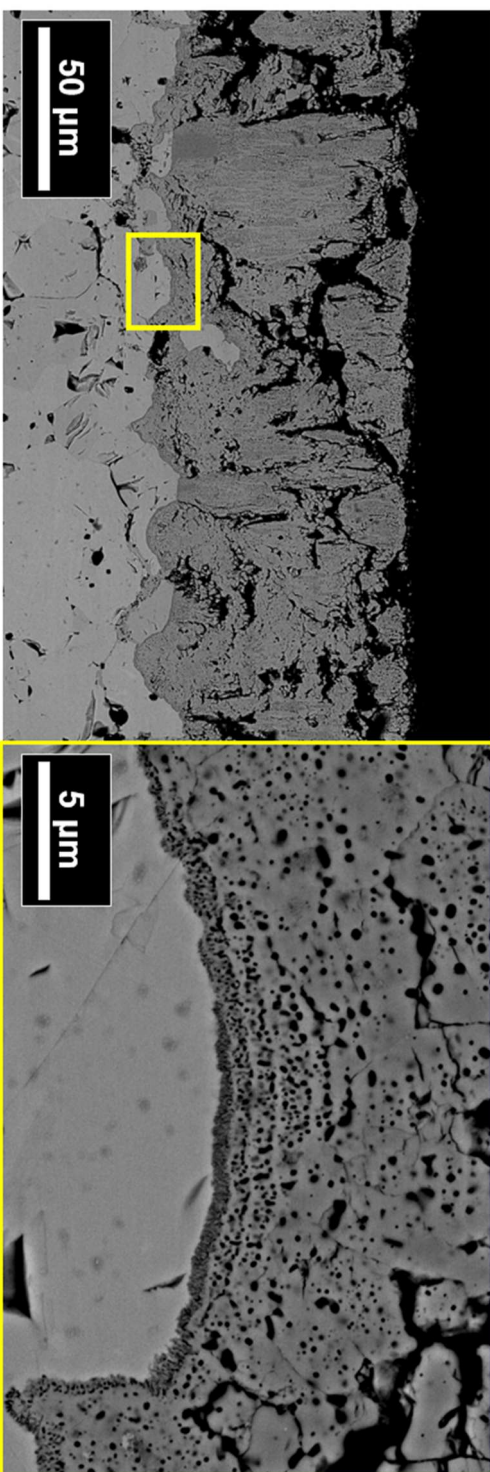


Figure A.13: Backscatter SEM micrograph of HfC oxidized at 1600°C for 7 min. The inner layer and the layered porous structure found at the interface are magnified on the right.

- Additional Micrographs from Part 3:
 - o Oxidation of Ta in MO Only and MO+AO

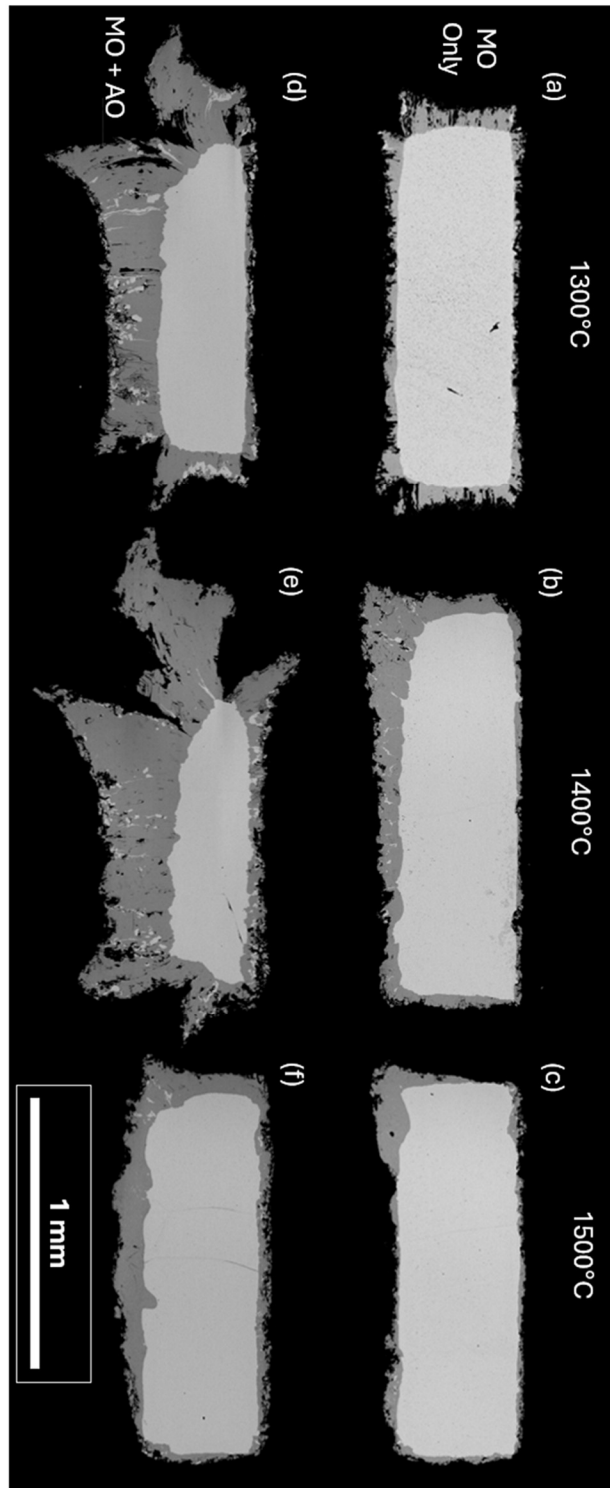


Figure A.14: Backscatter SEM micrographs of cross sections of Ta oxidized for 5 min at 1300-1500°C in MO only and MO+AO 1% O₂-Ar environments.

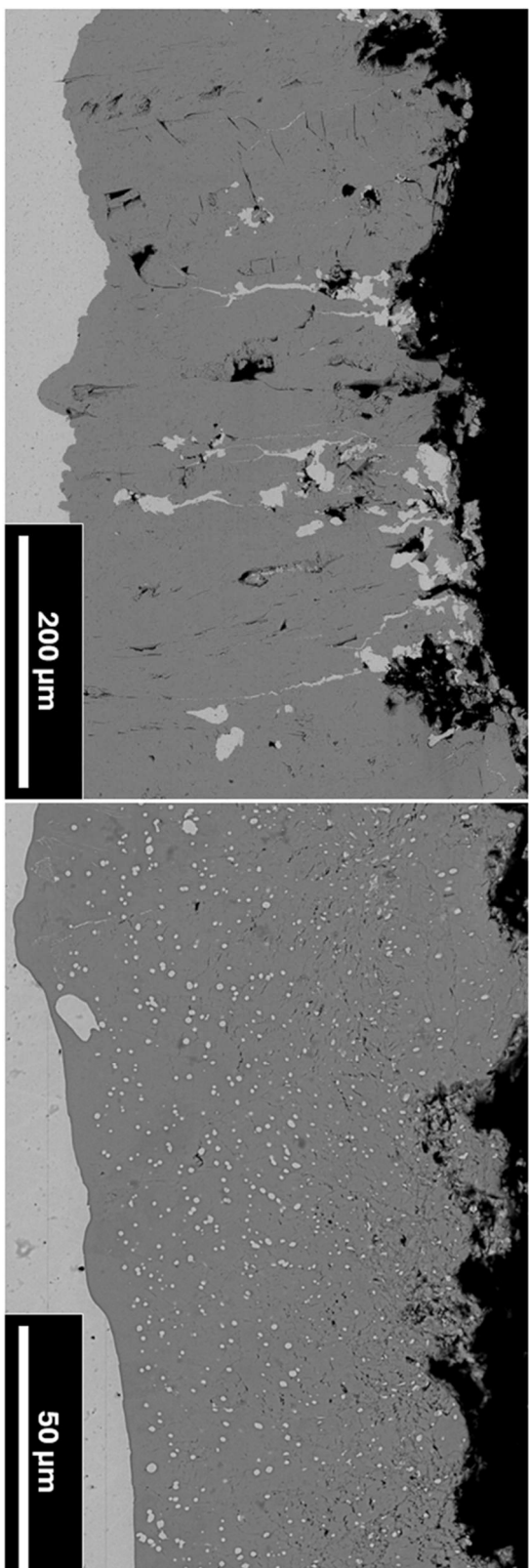


Figure A.15: Backscatter SEM micrograph of Ta oxidized at 1300°C and 1500°C for 5 min. Fewer cracks are visible in the 1500°C sample.

- Oxidation of TaC in MO Only and MO+AO

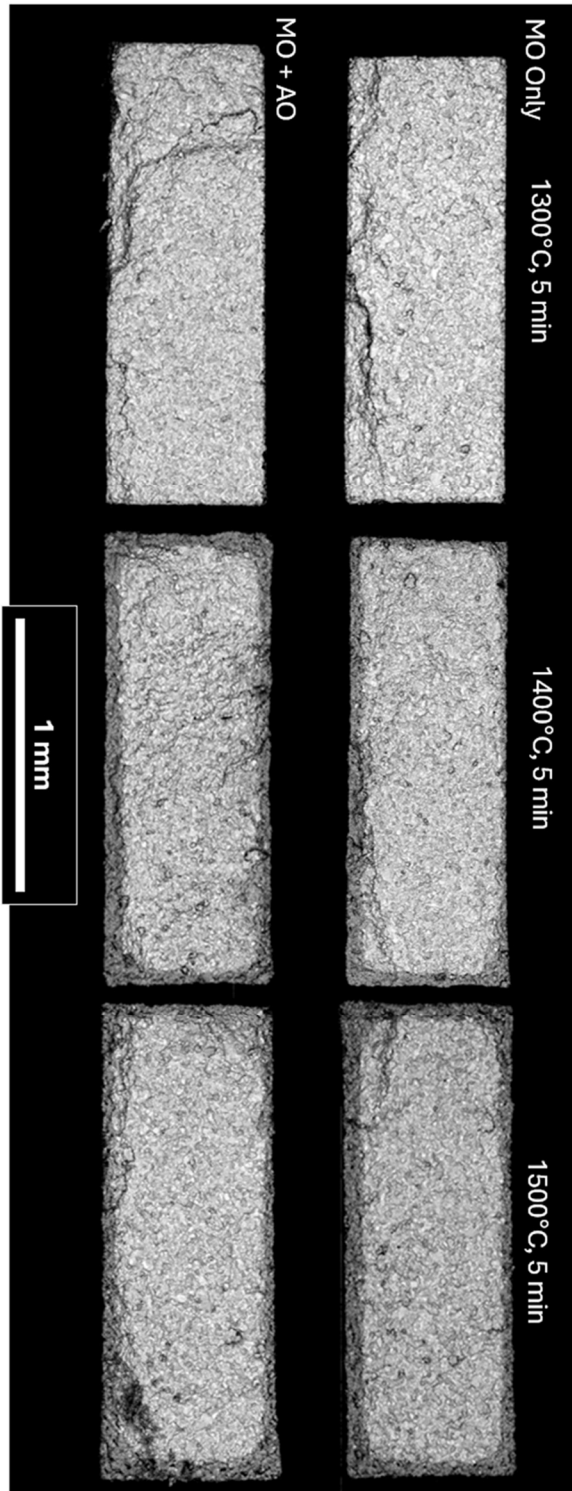


Figure A.16: Backscatter SEM micrographs of cross sections of TaC oxidized for 5 min at 1300-1500°C in MO only and MO+AO 1% O₂-Ar environments.

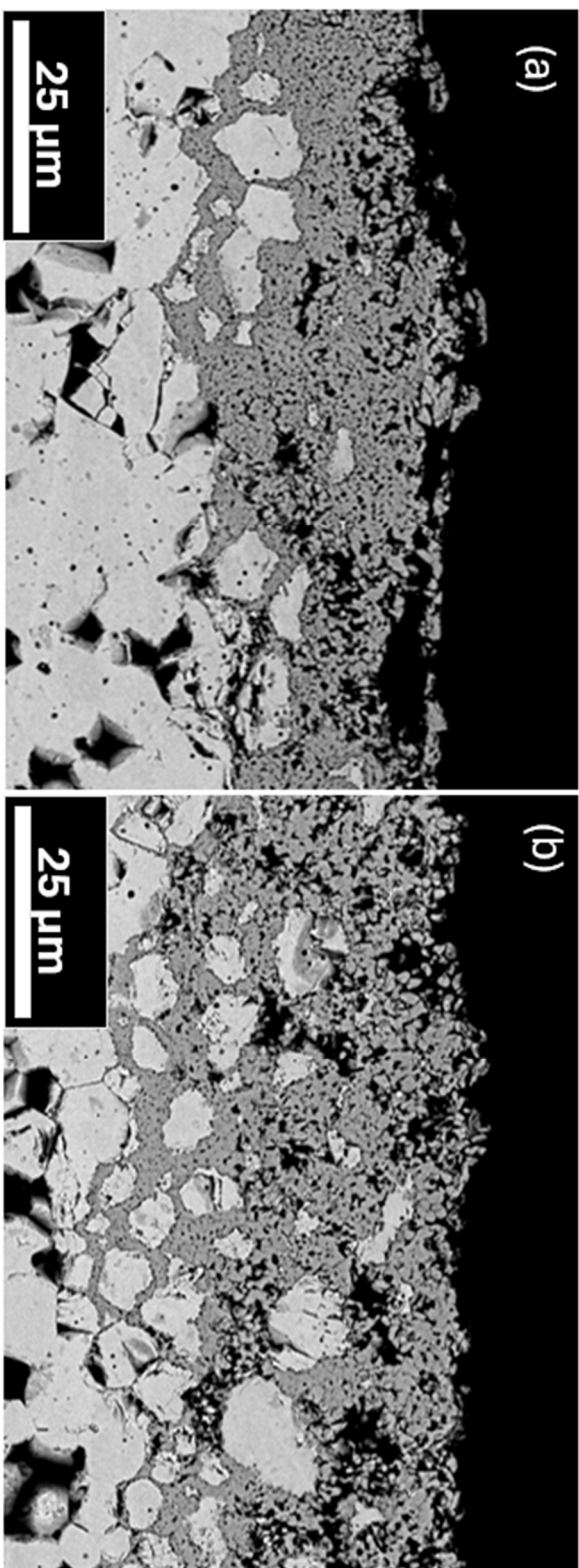


Figure A.17: Backscatter SEM micrograph of TaC oxidized at 1400°C for 5 min in (a) MO only and (b) MO+AO environments. Additional grain liftout and grain boundary oxidation are visible in the MO+AO sample.

- Oxidation of Zr in MO Only and MO+AO

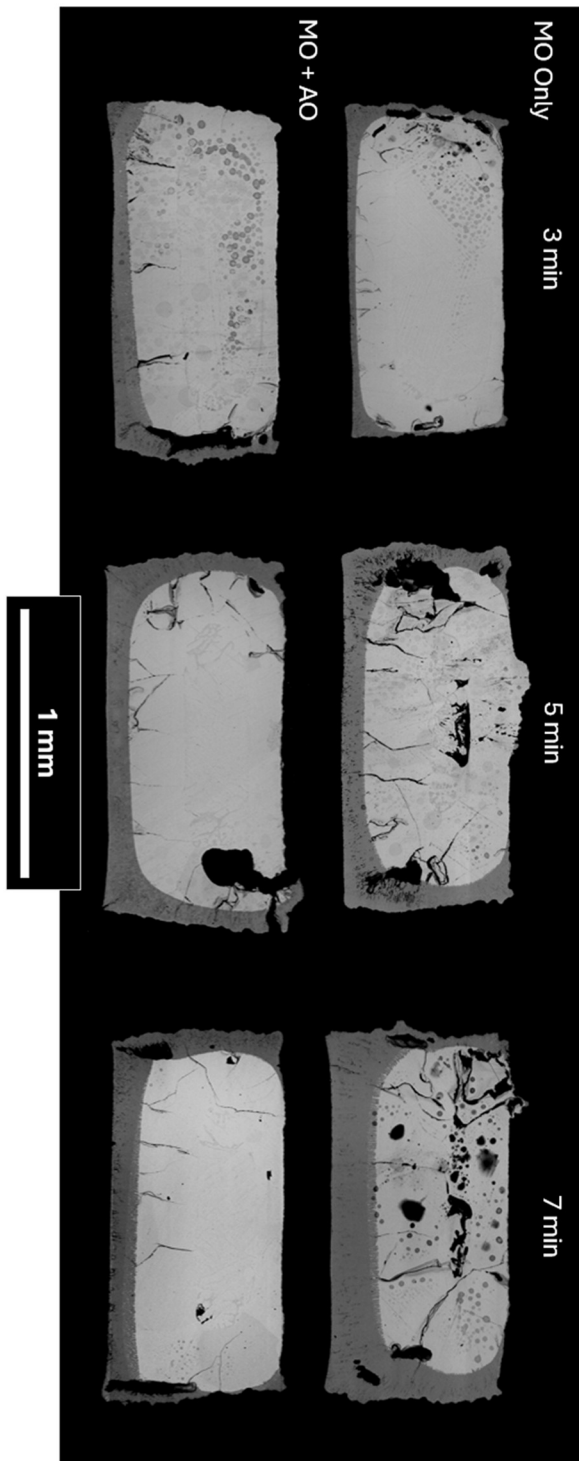


Figure A.18: Backscatter SEM micrographs of cross sections of Zr oxidized at 1400°C in MO only and MO+AO 1% O₂-Ar environments for 3, 5, and 7 min.

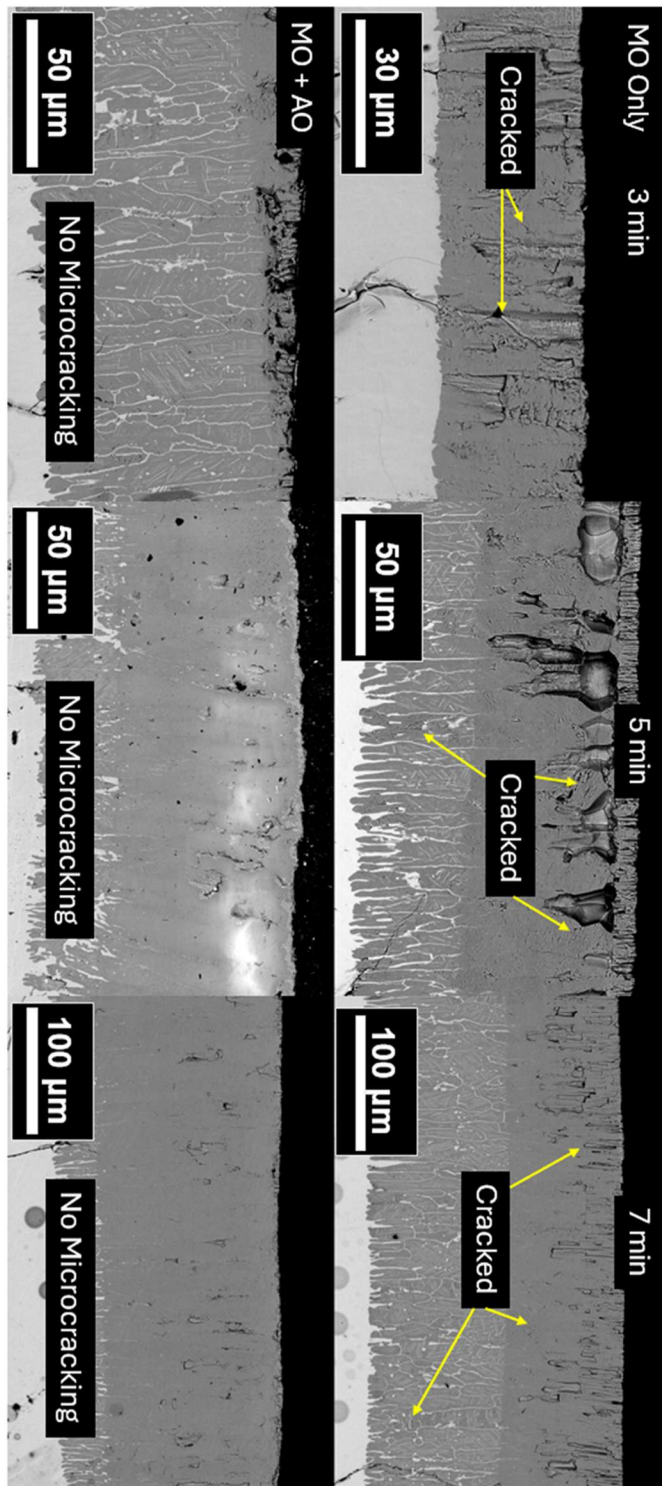


Figure A.19: Backscatter SEM micrographs of cross sections of Zr oxidized at 1400°C in MO only and MO+AO 1% O₂-Ar environments for 3, 5, and 7 min.

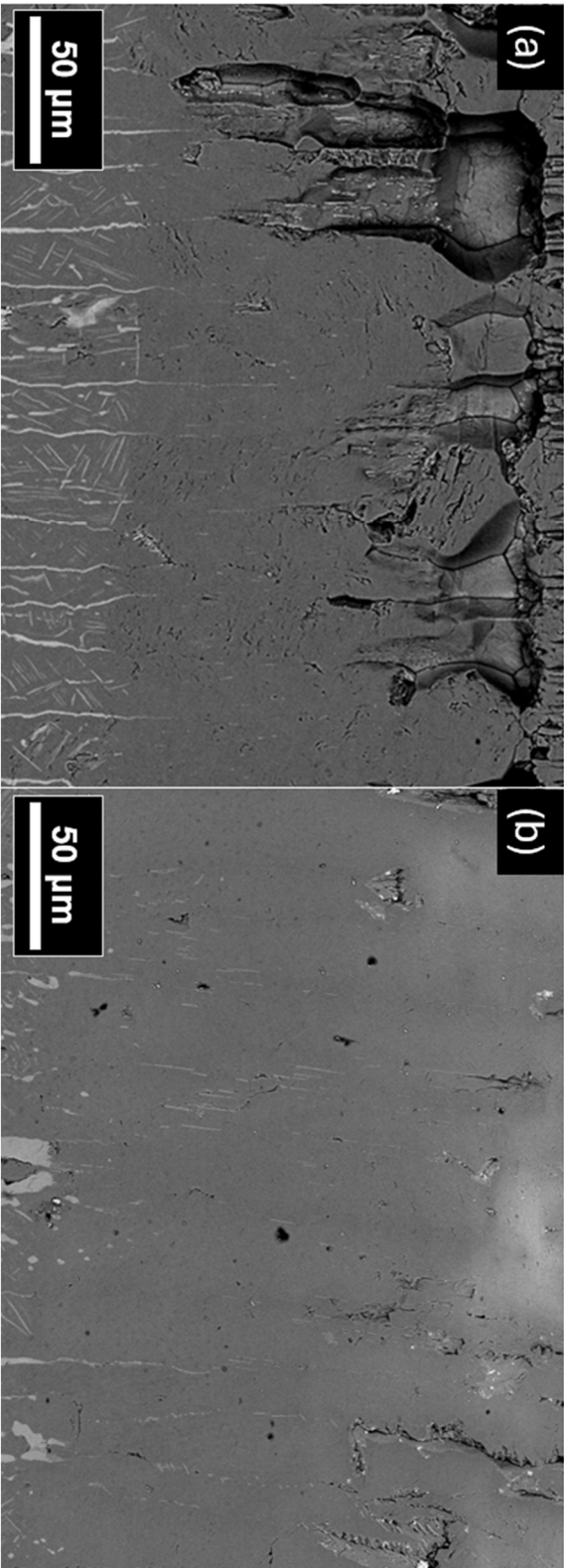


Figure A.20: Backscatter SEM micrograph of Zr oxidized at 1400°C for 5 min in (a) MO only and (b) MO+AO environments. The small radial cracks are responsible for breakaway oxidation. They are much more present in the oxide grown in MO than the oxide grown in MO+AO.

- Oxidation of ZrC in MO Only and MO+AO

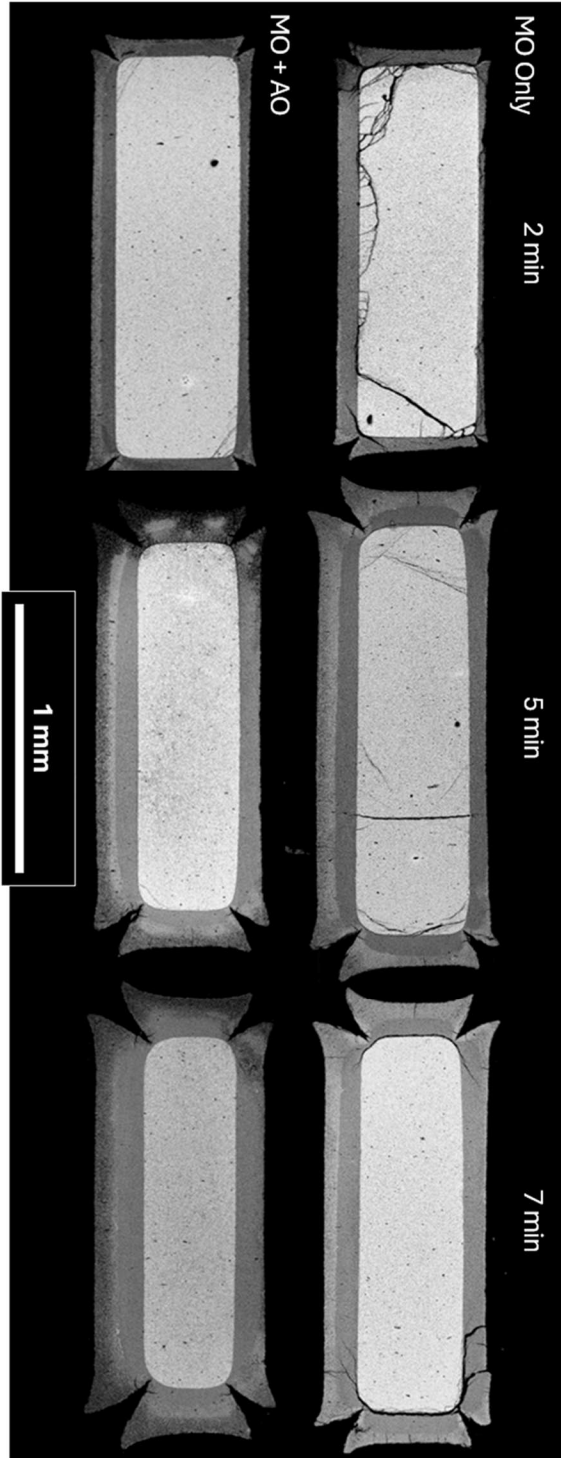


Figure A.21: Backscatter SEM micrographs of cross sections of ZrC oxidized at 1600°C in MO only and MO+AO 1% O₂-Ar environments for 2, 5, and 7 min.

- Oxidation of Hf in MO Only and MO+AO

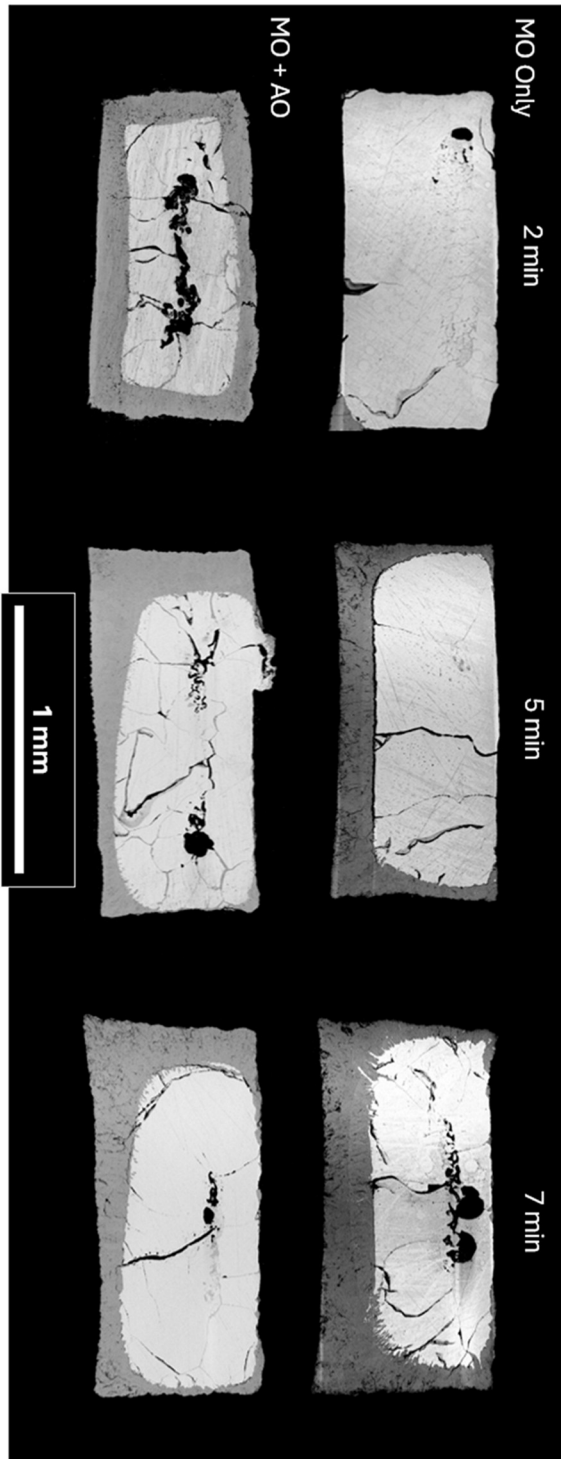


Figure A.22: Backscatter SEM micrographs of cross sections of Hf oxidized at 1600°C in MO only and MO+AO 1% O₂-Ar environments for 2, 5, and 7 min.

- Oxidation of HfC in MO Only and MO+AO

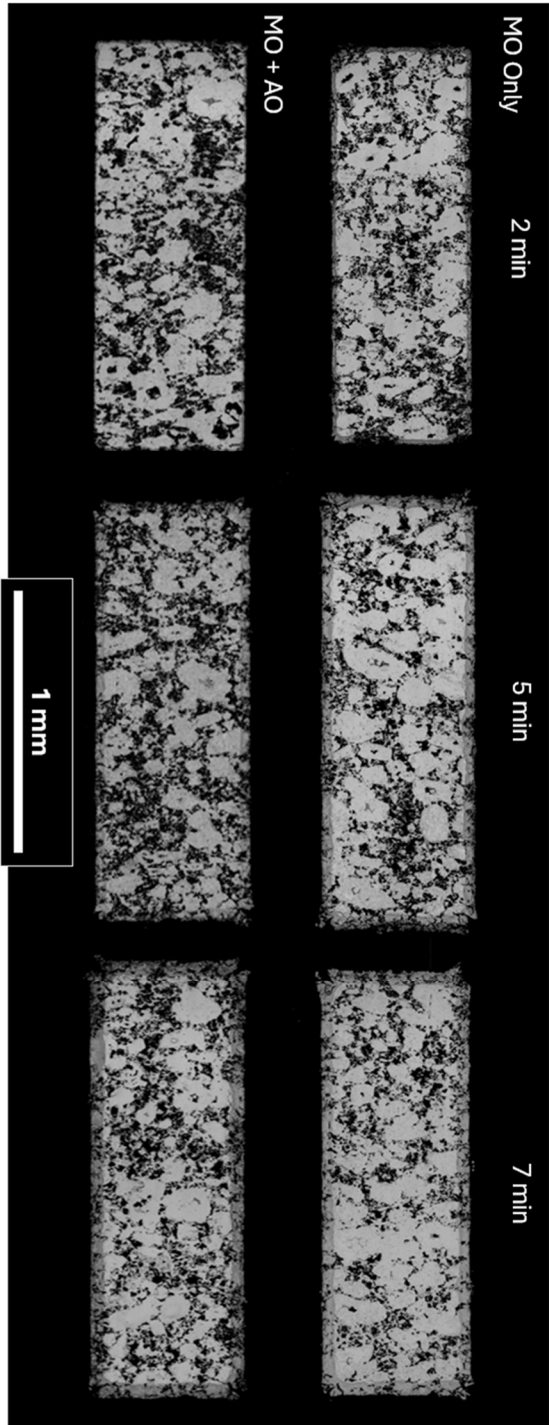


Figure A.23: Backscatterer SEM micrographs of cross sections of HfC oxidized at 1600°C in MO only and MO+AO 1% O₂-Ar environments for 2, 5, and 7 min.

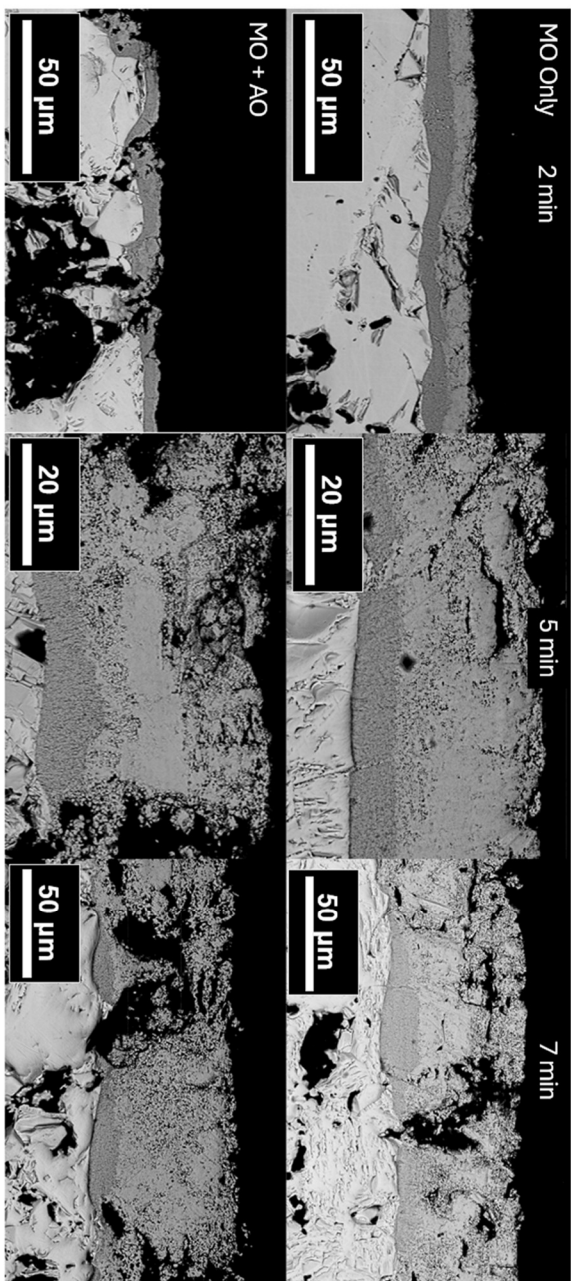


Figure A.24: Backscatterer SEM micrographs of cross sections of the oxide scale grown on HfC oxidized at 1600°C in MO only and MO+AO 1% O₂-Ar environments for 2, 5, and 7 min.

Appendix B: Ti and TiC

In the materials selection chapter of this work, it was shown that four of the most stable early transition metals oxides melt at a higher temperature than the melting point of SiO_2 ($\sim 1723^\circ\text{C}$): TiO_2 , ZrO_2 , HfO_2 , and Ta_2O_5 . Originally, it was planned that all eight of the associated metals and carbides would be investigated for this work. However, Ti and TiC presented unexpected experimental difficulties. Oxidation was much slower than the other materials of interest and experiments needed to run up to 10x longer to see appreciable oxide growth. Oxidation experiments could not be conducted much above 1300°C because the low melting temperature of Ti would cause sample sagging. Additionally, the TiC samples were very sensitive to the material heating rate and would quickly fail during the ramp-up stage of the experiments. When samples survived, the oxide scales would often spall off of both materials, making characterization difficult. As such, these materials were put aside, and only preliminary oxidation studies of Ti and TiC were conducted. Those preliminary results are presented here. Each data point only represents one sample which survived oxidation with the oxide scale intact.

a. Preliminary Results

Oxidation of Ti and TiC was conducted in the RHS at 1300°C for up to 60 min in 1% O_2 – Ar. Figure B.1 and B.2 shows the cross sections of these materials after 10, 20, and 60 min of

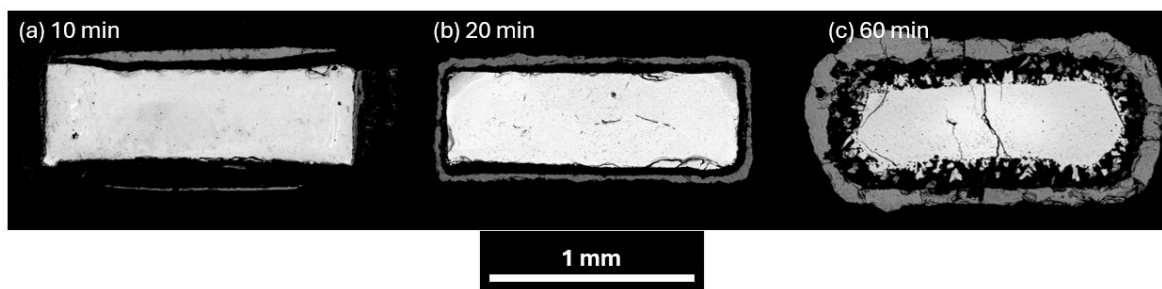


Figure B.1: Backscatter cross section micrographs of Ti post-oxidation at 1300°C in 1% O_2 – Ar for 10, 20, and 60 minutes.

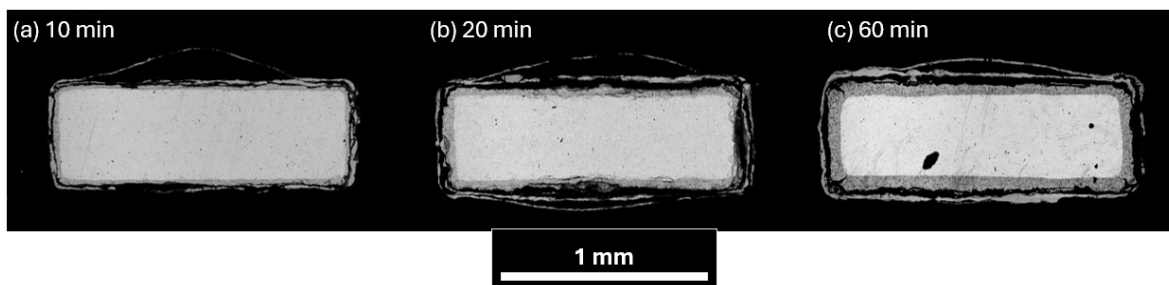


Figure B.2: Backscatter cross section micrographs of TiC post-oxidation at 1300°C in 1% O₂ – Ar for 10, 20, and 60 minutes.

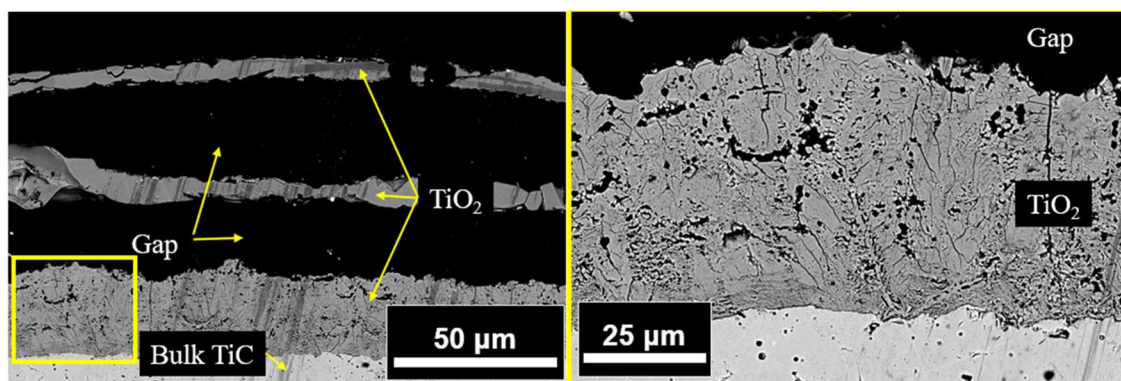


Figure B.3: Backscatter cross section micrographs of TiC after 60 min oxidation at 1300°C in 1% O₂ – Ar.

oxidation time. Figure B.3 shows a zoomed image of the oxide scale grown on TaC after 60 min. The scales that are grown on Ti are completely delaminated around the entirety of the sample. For TiC, a multi-layered oxide scale is grown, with the innermost remaining adherent to the TiC. The remaining layers are delaminated from the innermost oxide layer and from each other. Significant bowing of the oxide scale on TiC is observed, whereas the scale grown on Ti remains mostly rectangular except at the corners. A FIB liftout and HRTEM image of inner oxide layer is shown in Figure B.4. The white areas in the right image of Figure B.4 are holes in the scale. No retention of free carbon in TiC is noted via TEM.

The recession kinetics of Ti and TiC after oxidation at 1300°C are shown in Figure B.5. The material recession between the two materials is very similar. Both show an initially more rapid

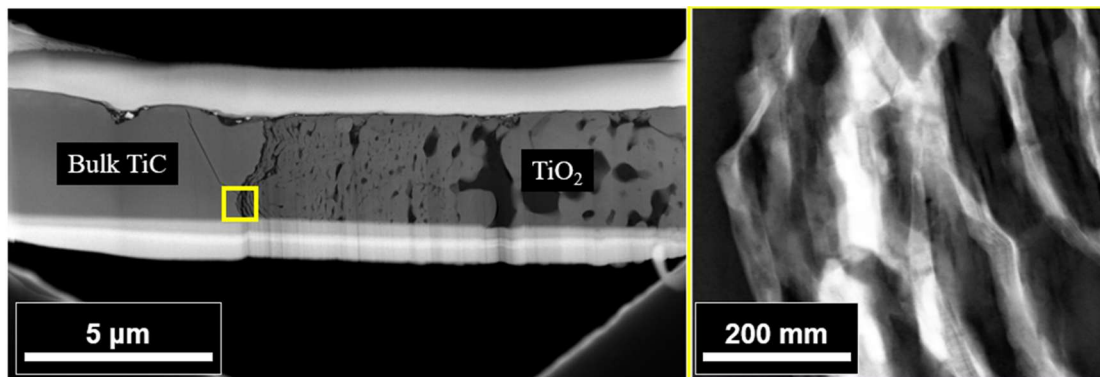


Figure B.4: TEM micrographs of TiC after 60 min oxidation at 1300°C in 1% O₂ – Ar. No carbon was found at the carbide/oxide interface.

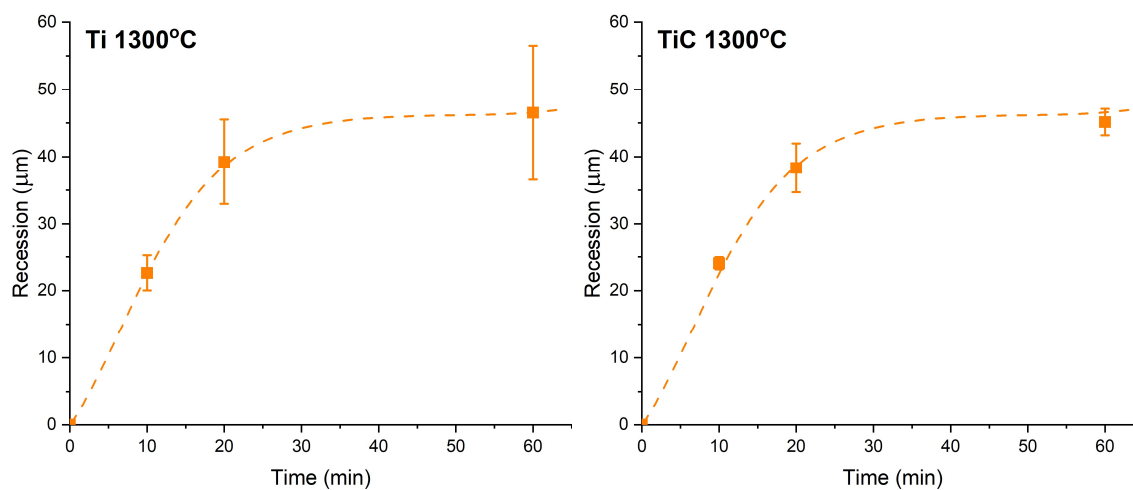


Figure B.5: Recession kinetics of Ti and TiC at 1300°C. The recession rate is very similar between the two materials. The dashed line is a spline fit.

recession rate, then level off at $\sim 45 \mu\text{m}$ of recession. When fitting the data, the early oxidation stage kinetics do not fit to the same rate law as the later oxidation stage. Rather, the data is better fit to a combination of rate laws at different times during oxidation. Early oxidation appears parabolic, but then slows to almost a complete stop. The later period is extremely sub-parabolic (approximately a quartic rate law).

b. Discussion

The recession rate due to oxygen dissolution in Ti is apparently negligible at the time scale studied here because the oxidation rates of Ti and TiC are nearly identical, despite the very large solubility of oxygen in Ti. It is unusual for Ti and TiC to exhibit the same oxidation rate. Carbon oxidation is expected to create CO(g) which creates a porous oxide and breaks up the scale, allowing rapid oxygen ingress. Indeed, the inner oxide layer formed on TiC is highly porous, but the outer layers are comparatively dense. The oxidation rate suggests that the scale formed on TiC is highly protective, like on Ti, so these outer layers must be the diffusion limiting scales.

The HRTEM image in Figure B.4 shows large holes at the carbide/oxide interface, where the carbon would be expected to be from previous TEM results. This suggests that carbon is removed from the system very quickly. Both the oxides which form delaminate very quickly from the underlying substrate. This appears to be a stress effect, given that the oxides formed on TiC are buckled so strongly. Stringer addressed the oxidation of Ti and also observed layered oxide buckle, such as observed here [149]. It is possible that rapid CO(g) formation and build up could be contributing to the excess buckling observed by the oxide formed on TiC. Another possible mechanism is that the Ti metal accommodates more of the growth stresses created, so buckling is less severe on Ti. The oxides on TiC could buckle more strongly because of the greater stiffness of the substrate, then separate from the carbide and remain in the observed morphology. However, because the oxidation rates of Ti and TiC are identical, it appears that carbon has negligible effects on the oxidation transport mechanism. Because there is no residual carbon remaining to investigate, it is not feasible with the limited data presented to make claims about the role of carbon in this material system.

Appendix C: Unsuccessful Experiments

During the course of this work, many experiments were unsuccessful as a result of several factors, including intrinsic flaws in the material, improper experimental setup, and failure to consider material properties when designing the experiment. It is the opinion of the author that some information regarding these failed experiments could provide useful information to future research conducted on these materials.

The most common failure mode identified in this work was sample cracking due to additional undesirable forces on the sample. These were most commonly encountered when clipping the sample into the RHS or MRHS. High temperatures created during previous experiments sometimes caused the copper leads to sag, and so when clipping samples in, additional bending forces were introduced. When the copper leads were not properly adjusted, the more brittle carbide samples failed almost every time. If this correction was ever neglected for the metals, the higher ductility of those materials was able to accommodate these forces without causing sample failure. Proper leveling of the conductive leads was critical to ensuring consistent, successful experiments.

The lower temperature and higher ductility of the metals caused them to sag at higher temperatures. This eliminated a level measurement surface for the pyrometer, causing experimental failure. Identifying the temperature range where materials remain structurally sound is also critical for successful experiments in the RHS or MRHS.

Finally, small cracks or defects in the original materials often caused excessive heating in the sample by reducing the cross-sectional area of the sample and driving increased Joule heating in the sample. While this type of error is harder to prevent, additional consideration for sample defects and quality should be given.

Bibliography

- [1] M. M. Opeka, I. G. Talmy, and J. A. Zaykoski, "Oxidation-based materials selection for 2000°C + hypersonic aerosurfaces: Theoretical considerations and historical experience," *J Mater Sci*, vol. 39, no. 19, pp. 5887–5904, 2004, doi: 10.1023/B:JMISC.0000041686.21788.77.
- [2] E. Wuchina, E. Opila, M. Opeka, B. Fahrenholtz, and I. Talmy, "UHTCs: Ultra-High Temperature Ceramic Materials for Extreme Environment Applications," *Electrochem Soc Interface*, vol. 16, no. 4, p. 30, 2007, doi: 10.1149/2.F04074IF.
- [3] K. A. Kane, B. A. Pint, D. Mitchell, and J. A. Haynes, "Oxidation of ultrahigh temperature ceramics : kinetics , mechanisms , and applications," *J Eur Ceram Soc*, no. May, 2021, doi: 10.1016/j.jeurceramsoc.2021.05.055.
- [4] X. Zhang, X. Luo, J. Han, J. Li, and W. Han, "Electronic structure, elasticity and hardness of diborides of zirconium and hafnium: First principles calculations," *Comput Mater Sci*, vol. 44, no. 2, pp. 411–421, Dec. 2008, doi: 10.1016/j.commatsci.2008.04.002.
- [5] H. O. Pierson, "The Refractory Carbides," in *Handbook of refractory carbides and nitrides : properties, characteristics, processing, and applications*, William Andrew Publishing/Noyes, 1996, ch. 2.
- [6] M. G. Bothara, S. J. Park, R. M. German, and S. V. Atre, "Spark plasma sintering of ultrahigh temperature ceramics," in *Advances in Powder Metallurgy and Particulate Materials - 2008, Proceedings of the 2008 World Congress on Powder Metallurgy and Particulate Materials, PowderMet 2008*, 2008, pp. 9264–9270. doi: 10.1007/978-3-030-05327-7_13.
- [7] N. S. Jacobson, J. L. Smialek, D. S. Fox, and E. J. Opila, "Durability of silica-protected ceramics in combustion atmospheres," United States: American Ceramic Society, Westerville, OH (United States), 1995. [Online]. Available: <https://www.osti.gov/biblio/135752>
- [8] M. Balat, G. Flamant, G. Male, and G. Pichelin, "Active to passive transition in the oxidation of silicon carbide at high temperature and low pressure in molecular and atomic oxygen," *J Mater Sci*, vol. 27, pp. 697–703, 1992.
- [9] P. Kofstad, "The Oxidation Behavior of Tantalum at 700°–1000°C," *J Electrochem Soc*, vol. 110, no. 6, p. 491, 1963, doi: 10.1149/1.2425799.
- [10] P. Kofstad, "Studies of the oxidation of tantalum at 1000°–1300°C," *Journal of the Less Common Metals*, vol. 5, no. 2, pp. 158–170, Apr. 1963, doi: 10.1016/0022-5088(63)90009-2.
- [11] P. Kofstad, "High-temperature oxidation of titanium," *Journal of The Less-Common Metals*, vol. 12, no. 6, pp. 449–464, 1967, doi: 10.1016/0022-5088(67)90017-3.
- [12] P. Kofstad and S. Espevik, "Kinetic study of high-temperature oxidation of hafnium," pp. 382–394, 1967.
- [13] K. Östhagen and P. Kofstad, "Oxidation of Zirconium and Zirconium-Oxygen Alloys at 800°C," *J. Electrochem. Soc*, vol. 109, no. 3, p. 204, Mar. 1962.
- [14] P. Kofstad, K. Hauffe, and H. Kjøllesdal, "Investigation on the Oxidation Mechanism of Titanium," *Acta Chem. Scand.*, vol. 12, no. 2, pp. 239–266, 1958.

- [15] P. Kofstad, P. B. Anderson, and O. J. Krudtaa, "Oxidation of titanium in the temperature range 800-1200°C," *Journal of The Less-Common Metals*, vol. 3, no. 2, pp. 89–97, 1961, doi: 10.1016/0022-5088(61)90001-7.
- [16] J. B. Berkowitz-Mattuck, "High-Temperature Oxidation: IV. Zirconium and Hafnium Carbides," *J Electrochem Soc*, vol. 114, no. 10, pp. 1030–1033, 1967, doi: 10.1149/1.2424178.
- [17] E. L. Courtright, J. T. Prater, G. R. Holcomb, G. R. St. Pierre, and R. A. Rapp, "Oxidation of hafnium carbide and hafnium carbide with additions of tantalum and praseodymium," *Oxidation of Metals*, vol. 36, no. 5–6, pp. 423–437, 1991, doi: 10.1007/BF01151590.
- [18] S. Shimada, F. Yunazar, and S. Otani, "Oxidation of Hafnium Carbide and Titanium Carbide Single Crystals with the Formation of Carbon at High Temperatures and Low Oxygen Pressures," *Journal of the American Ceramic Society*, vol. 77, no. 2, pp. 721–728, 2000.
- [19] C. Gasparini, R. Podor, D. Horlait, R. Chater, and W. E. Lee, "Zirconium Carbide Oxidation: Maltese Cross Formation and Interface Characterization," *Oxidation of Metals*, vol. 88, no. 3–4, pp. 509–519, Oct. 2017, doi: 10.1007/s11085-016-9672-6.
- [20] C. Gasparini, R. J. Chater, D. Horlait, L. Vandeperre, and W. E. Lee, "Zirconium carbide oxidation: Kinetics and oxygen diffusion through the intermediate layer," *Journal of the American Ceramic Society*, vol. 101, no. 6, pp. 2638–2652, Jun. 2018, doi: 10.1111/jace.15479.
- [21] S. Shimada and T. Ishil, "Oxidation Kinetics of Zirconium Carbide at Relatively Low Temperatures," *Journal of the American Ceramic Society*, vol. 73, no. 10, pp. 2804–2808, 1990, doi: 10.1111/j.1151-2916.1990.tb06678.x.
- [22] V. A. Lavrenko, L. A. Glebov, A. P. Pomitkin, V. G. Chuprina, and T. G. Protsenko, "High-Temperature Oxidation of Titanium Carbide in Oxygen," 1975.
- [23] V. B. Voitovich, "Mechanism of the High Temperature Oxidation of Titanium Carbide," *High Temperature Materials and Processes*, vol. 16, no. 4, pp. 243–253, 1997.
- [24] C. B. Barger, R. C. Benson, A. N. Jette, and T. E. Phillips, "Oxidation of Hafnium Carbide in the Temperature Range 1400° to 2060°C," *Journal of the American Ceramic Society*, vol. 76, no. 4, pp. 1040–1046, 1993, doi: 10.1111/j.1151-2916.1993.tb05332.x.
- [25] A. K. Kuriakose and J. L. Margrave, "The Oxidation Kinetics of Zirconium Diboride and Zirconium Carbide at High Temperatures," *J Electrochem Soc*, vol. 111, no. 7, p. 827, 1964, doi: 10.1149/1.2426263.
- [26] J. A. Scott, X. He, and D. W. Lipke, "The role of microstructure on high-temperature oxidation behavior of hafnium carbide," *Journal of the American Ceramic Society*, 2022, doi: 10.1111/jace.18941.
- [27] C. B. Barger, R. C. Benson, R. W. Newman, A. N. Jette, and T. E. Phillips, "Oxidation mechanisms of hafnium carbide and hafnium diboride in the temperature range 1400 to 2100°C," *Johns Hopkins APL Technical Digest (Applied Physics Laboratory)*, vol. 14, no. 1, pp. 29–36, 1993.
- [28] M. Desmaison-Brut, N. Alexandre, and J. Desmaison, "Comparison of the oxidation behaviour of two dense hot isostatically pressed tantalum carbide (TaC and Ta₂C) materials," 1997. doi: 10.1016/s0955-2219(96)00235-x.
- [29] D. M. Van Wie, D. G. Drewry, D. E. King, and C. M. Hudson, "The hypersonic environment: Required operating conditions and design challenges."

- [30] D. E. Rosner and H. D. Allendorf, "Kinetics of the Attack of High-Temperature Molybdenum and Tungsten by Atomic Oxygen," *J Electrochem Soc*, vol. 114, no. 4, p. 305, 1967, doi: 10.1149/1.2426583.
- [31] D. E. Rosner and H. D. Allendorf, "High temperature oxidation of carbon by atomic oxygen," *Carbon N Y*, vol. 3, no. 2, pp. 153–156, 1965, doi: 10.1016/0008-6223(65)90042-4.
- [32] M. J. H. Balat, "Determination of the Active-to-Passive Transition in the Oxidation of Silicon Carbide in Standard and Microwave-Excited Air," 1996.
- [33] M. Balat-Pichelin, J. M. Badie, R. Berjoan, and P. Boubert, "Recombination coefficient of atomic oxygen on ceramic materials under earth re-entry conditions by optical emission spectroscopy," *Chem Phys*, vol. 291, no. 2, pp. 181–194, Jun. 2003, doi: 10.1016/S0301-0104(03)00152-6.
- [34] M. Balat-Pichelin, L. Bedra, O. Gerasimova, and P. Boubert, "Recombination of atomic oxygen on α -Al₂O₃ at high temperature under air microwave-induced plasma," *Chem Phys*, vol. 340, no. 1–3, pp. 217–226, Nov. 2007, doi: 10.1016/j.chemphys.2007.09.019.
- [35] M. J. H. Balat-Pichelin, L. Bedra, J. M. Badie, and P. Boubert, "Atomic oxygen recombination and chemical energy accommodation on alumina at high temperature," in *AIP Conference Proceedings*, May 2005, pp. 941–946. doi: 10.1063/1.1941655.
- [36] M. Balat, M. Czerniak, and J. M. Badie, "Thermal and Chemical Approaches for Oxygen Catalytic Recombination Evaluation on Ceramic Materials at High Temperature," *Appl Surf Sci*, vol. 120, pp. 225–238, 1997.
- [37] G. Primc, R. Zaplotnik, A. Vesel, and M. Mozetic, "Microwave discharge as a remote source of neutral oxygen atoms," *AIP Adv*, vol. 1, no. 2, 2011, doi: 10.1063/1.3598415.
- [38] P. Kofstad, "Low-pressure oxidation of tantalum at 1300°-1800°C," *Journal of The Less-Common Metals*, vol. 7, no. 4, pp. 241–266, 1964, doi: 10.1016/0022-5088(64)90022-0.
- [39] J. P. Pemsler, "Studies on the Oxygen Gradients in Oxidizing Metals: III. Kinetics of the Oxidation of Zirconium at High Temperatures," *J Electrochem Soc*, vol. 112, no. 5, pp. 477–484, 1965.
- [40] J. P. Pemsler, "Studies on the Oxygen Gradients in Oxidizing Metals: IV. Kinetics of the Oxidation of Hafnium at High Temperatures," *J Electrochem Soc*, vol. 113, no. 6, pp. 619–621, 1966.
- [41] M. Schuhmacher and P. Eveno, "Oxygen Diffusion in Titanium Carbide," *Solid State Ion*, vol. 12, pp. 263–270, 1984.
- [42] C. Zhang, "High Temperature Oxidation Study of Tantalum Carbide-Hafnium Carbide Solid Solutions Synthesized by Spark Plasma Sintering," 2016, doi: 10.25148/etd.FIDC001239.
- [43] C. Zhang, B. Boesl, and A. Agarwal, "Oxidation resistance of tantalum carbide-hafnium carbide solid solutions under the extreme conditions of a plasma jet," *Ceram Int*, vol. 43, no. 17, pp. 14798–14806, 2017, doi: 10.1016/j.ceramint.2017.07.227.
- [44] S. Shimada, "Interfacial reaction on oxidation of carbides with formation of carbon," *Solid State Ion*, vol. 141–142, pp. 99–104, 2001, doi: 10.1016/S0167-2738(01)00727-5.
- [45] A. Nisar *et al.*, "Unveiling enhanced oxidation resistance and mechanical integrity of multicomponent ultra-high temperature carbides," *Journal of the American Ceramic Society*, vol. 105, no. 4, pp. 2500–2516, 2022, doi: 10.1111/jace.18281.

- [46] A. Nisar, T. Sakthivel, C. Zhang, B. Boesl, S. Seal, and A. Agarwal, "Quantification of complex protective surface oxide layer formed during plasma jet exposure of multicomponent ultra-high temperature carbides," *Appl Surf Sci*, vol. 592, no. February, p. 153247, 2022, doi: 10.1016/j.apsusc.2022.153247.
- [47] A. Paul, J. G. P. Binner, B. Vaidhyanathan, A. C. J. Heaton, and P. M. Brown, "Oxyacetylene torch testing and microstructural characterization of tantalum carbide," *J Microsc*, vol. 250, no. 2, pp. 122–129, 2013, doi: 10.1111/jmi.12028.
- [48] A. Lashtabeg, M. Smart, D. Riley, A. Gillen, and J. Drennan, "The effect of extreme temperature in an oxidising atmosphere on dense tantalum carbide (TaC)," *J Mater Sci*, vol. 48, no. 1, pp. 258–264, Jan. 2013, doi: 10.1007/s10853-012-6740-4.
- [49] K. Shugart, B. Patterson, D. Lichtman, S. Liu, and E. Opila, "Mechanisms for variability of ZrB₂-30 vol% SiC oxidation kinetics," *Journal of the American Ceramic Society*, vol. 97, no. 7, pp. 2279–2285, 2014, doi: 10.1111/jace.12911.
- [50] G. Östberg, "Metallographic Study of the Isothermal Transformation of Beta Phase in Zircaloy-2," *Aktiebolaget Atomenergi*, vol. AE-30, 1960.
- [51] A. R. Massih, T. Andersson, P. Witt, M. Dahlbäck, and M. Limbäck, "Effect of quenching rate on the β -to- α phase transformation structure in zirconium alloy," *Journal of Nuclear Materials*, vol. 322, no. 2–3, pp. 138–151, Nov. 2003, doi: 10.1016/S0022-3115(03)00323-4.
- [52] L. G. Ritchie and A. Atrens, "THE DIFFUSION OF OXYGEN IN ALPHA-ZIRCONIUM," 1977.
- [53] O. Fabrichnaya and D. Pavlyuchkov, "Assessment of Experimental Data and Thermodynamic Modeling in the Zr-Fe-O System," *Metall Mater Trans A Phys Metall Mater Sci*, vol. 47, no. 1, pp. 152–159, Jan. 2016, doi: 10.1007/s11661-015-2805-8.
- [54] S. Aronson, "Oxidation and Equilibrium in Nonstoichiometric Zirconium Dioxide Powder," *J. Electrochem. Soc.*, vol. 108, no. 4, pp. 312–316, Apr. 1961.
- [55] R. F. Domagala and D. J. Mcpherson, "System Zirconium-Oxygen," *JOM*, vol. 6, no. 2, pp. 238–246, Feb. 1954.
- [56] R. E. Pawel and J. J. Campbell, "A Comparison of the High Temperature Oxidation Behavior of Zircaloy-4 and Pure Zirconium."
- [57] C. J. Rosa and W. W. Smeltzert, "THE PARABOLIC OXIDATION KINETICS OF BETA-ZIRCONIUM*."
- [58] R. E. Westerman, "High-Temperature Oxidation of Zirconium and Zircaloy-2 in Oxygen and Water Vapor," *J Electrochem Soc*, vol. 111, no. 2, p. 140, 1964, doi: 10.1149/1.2426073.
- [59] X. Ma, C. Toffolon-Masclet, T. Guilbert, D. Hamon, and J. C. Brachet, "Oxidation kinetics and oxygen diffusion in low-tin Zircaloy-4 up to 1523 K," *Journal of Nuclear Materials*, vol. 377, no. 2, pp. 359–369, Jul. 2008, doi: 10.1016/j.jnucmat.2008.03.012.
- [60] C. C. Tang, M. Stueber, H. J. Seifert, and M. Steinbrueck, "Protective coatings on zirconium-based alloys as accident-tolerant fuel (ATF) claddings," *Corrosion Reviews*, vol. 35, no. 3, pp. 141–165, 2017, doi: 10.1515/corrrev-2017-0010.

- [61] S. Leistikow and G. Schanz, "OXIDATION-KINETICS AND RELATED PHENOMENA OF ZIRCALOY-4 FUEL CLADDING EXPOSED TO HIGH-TEMPERATURE STEAM AND HYDROGEN STEAM MIXTURES UNDER PWR ACCIDENT CONDITIONS," *Nuclear Engineering and Design*, vol. 103, no. 1, pp. 65–84, 1987, doi: 10.1016/0029-5493(87)90286-x.
- [62] R. A. Perkins, "OXYGEN DIFFUSION IN ZIRCALOY," *Journal of Nuclear Materials*, vol. 68, pp. 148–160, 1977.
- [63] M. W. Mallett, W. M. Albrecht, and P. R. Wilson, "The Diffusion of Oxygen in Alpha and Beta Zircaloy 2 and Zircaloy 3 at High Temperatures," *J. Electrochem. Soc.*, vol. 106, pp. 181–185, 1959.
- [64] R. E. Pawel, "Oxygen Diffusion in Beta Zircaloy During Steam Oxidation," *Journal of Nuclear Materials*, vol. 50, pp. 247–258, 1974.
- [65] A. T. Motta, A. Couet, and R. J. Comstock, "Corrosion of Zirconium Alloys Used for Nuclear Fuel Cladding," *Annu Rev Mater Res*, vol. 45, pp. 311–343, 2015, doi: 10.1146/annurev-matsci-070214-020951.
- [66] L. Portier, T. Bredel, J. C. Brachet, V. Maillot, J. P. Mardon, and A. Lesbros, "Influence of long service exposures on the thermal-mechanical behavior of Zy-4 and M5 (TM) alloys in LOCA conditions," in *Zirconium in the Nuclear Industry: 14th International Symposium*, vol. 1467, P. Rudling and B. Kammenzind, Eds., W Conshohocken: American Society Testing and Materials, 2005, pp. 896–920. doi: 10.1520/stp37540s.
- [67] J. P. Pemsler, "Studies on the Oxygen Gradients in Oxidizing Metals: I. Zirconium," *J Electrochem Soc*, vol. 111, no. 4, pp. 381–385, 1964.
- [68] J. P. Pemsler, "Studies on the Oxygen Gradients in Oxidizing Metals: V. The Oxidation of Oxygen-saturated Zirconium," *J Electrochem Soc*, vol. 113, no. 12, pp. 1241–1244, 1966.
- [69] H. El Kadiri *et al.*, "Transformations and cracks in zirconia films leading to breakaway oxidation of Zircaloy," *Acta Mater*, vol. 61, no. 11, pp. 3923–3935, Jun. 2013, doi: 10.1016/j.actamat.2013.02.052.
- [70] T. Ahmed and L. H. Keys, "The Breakaway Oxidation of Zirconium and Its Alloys, A Review," *Journal of the Less-Common Metals*, vol. 39, pp. 99–107, Jul. 1975.
- [71] S. Shimada, M. Yoshimatsu, ~ Michio Inagaki~, and S. Otani~, "Formation and Characterization of Carbon at the ZrC/ZrO₂ Interface by Oxidation of ZrC Single Crystals," 1998.
- [72] S. Shimada, "A thermoanalytical study on the oxidation of ZrC and HfC powders with formation of carbon," *Solid State Ion*, vol. 149, pp. 319–26, 2002, [Online]. Available: www.elsevier.com/locate/ssi
- [73] B. Wei *et al.*, "Corrosion kinetics and mechanisms of ZrC_{1-x} ceramics in high temperature water vapor," *RSC Adv*, vol. 8, no. 32, pp. 18163–18174, 2018, doi: 10.1039/c8ra02386g.
- [74] G. A. Rama Rao and V. Venugopal, "Kinetics and mechanism of the oxidation of ZrC," *J Alloys Compd*, vol. 50, no. 12, pp. 686–688, 1999.
- [75] R. N. Keller, "The Lanthanide Contraction as a Teaching Aid," *J. Chem. Edu.*, vol. 18, pp. 312–317, Jun. 1951, [Online]. Available: <https://pubs.acs.org/sharingguidelines>

- [76] L. Xu, Y. Xiao, A. Van Sandwijk, Q. Xu, and Y. Yang, "Separation of zirconium and hafnium: A review," in *Energy Materials 2014, Conference Proceedings*, John Wiley and Sons Inc., 2014, pp. 451–457. doi: 10.1002/9781119027973.ch53.
- [77] D. Shin, R. Arróyave, and Z. K. Liu, "Thermodynamic modeling of the Hf-Si-O system," *CALPHAD*, vol. 30, no. 4, pp. 375–386, Dec. 2006, doi: 10.1016/j.calphad.2006.08.006.
- [78] W. W. Smeltzer and M. T. Simnad, "Oxidation of hafnium," *Acta Metallurgica*, vol. 5, no. 6, pp. 328–334, 1957, doi: 10.1016/0001-6160(57)90045-7.
- [79] J. P. Pemsler, "Studies on the Oxygen Gradients in Oxidizing Metals: II. Hafnium," *J Electrochem Soc*, vol. 111, no. 12, pp. 1339–1342, 1964.
- [80] J. A. Scott, X. He, and D. W. Lipke, "High temperature oxidation regime transitions in hafnium carbide," *Journal of the American Ceramic Society*, vol. 107, no. 11, pp. 7289–7296, Nov. 2024, doi: 10.1111/jace.20008.
- [81] G. R. Holcomb and G. R. S. Pierre, "Application of a counter-current gaseous diffusion model to the oxidation of hafnium carbide at 1200 to 1530°C," *Oxidation of Metals*, vol. 40, no. 1–2, pp. 109–118, 1993, doi: 10.1007/BF00665261.
- [82] G. Sharma, S. V. Ushakov, and A. Navrotsky, "Size driven thermodynamic crossovers in phase stability in zirconia and hafnia," *Journal of the American Ceramic Society*, vol. 101, no. 1, pp. 31–35, Jan. 2018, doi: 10.1111/jace.15200.
- [83] K. J. Meisner, R. Zaman, and B. C. Zhou, "Thermodynamic modeling of the Ta-O system," *CALPHAD*, vol. 76, Mar. 2022, doi: 10.1016/j.calphad.2022.102391.
- [84] R. Bredesen and P. Kofstad, "A REINTERPRETATION OF THE DEFECT STRUCTURE OF L-Ta₂O₅," 1988.
- [85] S. Schmid and V. Fung, "Incommensurate modulated structures in the Ta₂O₅-Al₂O₃ system," *Aust J Chem*, vol. 65, no. 7, pp. 851–859, 2012, doi: 10.1071/CH12080.
- [86] S. Schmid, R. L. Withers, and J. G. Thompson, "The incommensurately modulated(1 - x)Ta₂O₅· xWO₃, 0 ≤ x ≤ 0.267 solid solution," *J Solid State Chem*, vol. 99, no. 2, pp. 226–242, 1992, doi: 10.1016/0022-4596(92)90310-R.
- [87] C. Askeljung, B. O. Marinder, and M. Sundberg, "Effect of heat treatment on the structure of L-Ta₂O₅: A study by XRPD and HRTEM methods," *J Solid State Chem*, vol. 176, no. 1, pp. 250–258, 2003, doi: 10.1016/j.jssc.2003.07.003.
- [88] J. Spyridelis, P. Delavignette, and S. Amelinckx, "On the Superstructures of Ta₂O₅ and Nb₂O₅," *Physica Status Solidi (B)*, vol. 19, no. 2, pp. 683–704, 1967, doi: 10.1002/pssb.19670190220.
- [89] S. Schmid, K. Fütterer, and J. G. Thompson, "X-ray Structure Refinement of (3 + 1)-Dimensional Incommensurate Composite (1 - X)Ta₂O₅·xWO₃, x = 0.1," *Acta Crystallogr B*, vol. 52, no. 2, pp. 223–231, 1996, doi: 10.1107/S0108768195010524.
- [90] N. C. Stephenson and R. S. Roth, "Structural systematics in the binary system Ta₂O₅-WO₃. V. The structure of the low-temperature form of tantalum oxide L-Ta₂O₅," *Acta Crystallogr B*, vol. 27, no. 5, pp. 1037–1044, 1971, doi: 10.1107/s056774087100342x.

- [91] K. Lehovec, "Lattice structure of β -Ta₂O₅," *Journal of The Less-Common Metals*, vol. 7, no. 6, pp. 397–410, 1964, doi: 10.1016/0022-5088(64)90036-0.
- [92] L. A. Aleshina and S. V. Loginova, "Rietveld analysis of X-ray diffraction pattern from β -Ta₂O₅ oxide," *Kristallografiya*, vol. 47, no. 3, pp. 460–465, 2002.
- [93] I. E. Grey, W. G. Mumme, and R. S. Roth, "The crystal chemistry of L-Ta₂O₅ and related structures," *J Solid State Chem*, vol. 178, no. 11, pp. 3308–3314, 2005, doi: 10.1016/j.jssc.2005.08.011.
- [94] B. O. Marinder, "Moser's C-line, the apparent multiplicity m' and modules in descriptions of L-Ta₂O₅ and related structures," *J Solid State Chem*, vol. 160, no. 1, pp. 62–68, 2001, doi: 10.1006/jssc.2001.9191.
- [95] R. S. Roth and J. L. Waring, "Effect of oxide additions on the polymorphism of tantalum pentoxide. III. "Stabilization of the Low Temperature Structure Type," *J Solid State Chem*, vol. 2, no. 3, pp. 485–493, Nov. 1970, doi: 10.6028/jres.074A.038.
- [96] N. C. Stephenson and R. S. Roth, "The Crystal Structure of the High Temperature Form of Ta₂O₅," *J Solid State Chem*, vol. 18, no. 2, pp. 145–153, 1970, doi: 10.1107/s0365110x65000658.
- [97] R. S. Roth, J. L. Waring, and W. S. Brower, "Effect of oxide additions on the polymorphism of tantalum pentoxide. II. "Stabilization" of the high temperature structure type," *J Res Natl Bur Stand A Phys Chem*, vol. 74A, no. 4, p. 477, 1970, doi: 10.6028/jres.074a.037.
- [98] X. Q. Liu, X. D. Han, Z. Zhang, L. F. Ji, and Y. J. Jiang, "The crystal structure of high temperature phase Ta₂O₅," *Acta Mater*, vol. 55, no. 7, pp. 2385–2396, 2007, doi: 10.1016/j.actamat.2006.11.031.
- [99] S. N. Karlsdottir and J. W. Halloran, "Rapid oxidation characterization of ultra-high temperature ceramics," *Journal of the American Ceramic Society*, vol. 90, no. 10, pp. 3233–3238, 2007, doi: 10.1111/j.1551-2916.2007.01861.x.
- [100] L. Backman, K. Graham, M. Dion, and E. Opila, "Analysis of Test Specimen Temperature Gradients Incurred in Resistive Heating System Oxidation Studies of Ultra-High Temperature Ceramics," *High Temperature Corrosion of Materials*, 2024.
- [101] C. Schneider, W. Rasband, and K. Eliceiri, "NIH Image to ImageJ: 25 years of image analysis," *Nat Methods*, vol. 9, pp. 671–675, 2012, doi: <https://doi.org/10.1038/nmeth.2089>.
- [102] B. Lichter, "Precision Lattice Parameter Determination of Zirconium-Oxygen Solid Solution," *TRANSACTIONS OF THE METALLURGICAL SOCIETY OF AIME*, vol. 218, no. 6, pp. 1015–1018, Dec. 1960.
- [103] P. Hofmann *et al.*, "QUENCH-01. Experimental and calculational results," Germany, 1998. doi: <https://doi.org/>.
- [104] V. K. Tolpygo and D. R. Clarke, "Wrinkling of α -Alumina Films Grown by Thermal Oxidation - I. Quantitative Studies on Single Crystals of Fe-Cr-Al Alloy," *Acta mater.*, vol. 46, no. 14, pp. 5153–5166, 1998.
- [105] F. A. Golightly, F. H. Stott, and G. C. Wood, "The Influence of Scale Adhesion Alloy Yttrium Additions on the Oxide-to an Iron-Chromium-Aluminum," 1976.
- [106] F. N. Rhines and J. S. Wolf, "The Role of Oxide Microstructure and Growth Stresses in the High-Temperature Scaling of Nickel," *Metallurgical Transactions*, vol. 1, pp. 1701–1710, 1970.

- [107] J. H. Baek and Y. H. Jeong, “Breakaway phenomenon of Zr-based alloys during a high-temperature oxidation,” *Journal of Nuclear Materials*, vol. 372, no. 2–3, pp. 152–159, Jan. 2008, doi: 10.1016/j.jnucmat.2007.02.011.
- [108] R. C. Garvie, “The Occurrence of Metastable Tetragonal Zirconia as a Crystallite Size Effect,” *J. Phys. Chem.*, vol. 69, no. 4, pp. 1238–1243, Apr. 1965, [Online]. Available: <https://pubs.acs.org/sharingguidelines>
- [109] C. W. Bale *et al.*, “FactSage thermochemical software and databases, 2010–2016,” *Calphad*, vol. 54, pp. 35–53, 2016, doi: <https://doi.org/10.1016/j.calphad.2016.05.002>.
- [110] F. Adar, “Use of Raman Spectroscopy to Qualify Carbon Materials,” *Spectroscopy*, vol. 37, no. 6, pp. 11–15, Jun. 2022, [Online]. Available: www.analytik-jena.us
- [111] S. Guilbert *et al.*, “Hafnium Oxidation at High Temperature in Steam,” *Journal of Nuclear Materials*, vol. 550, pp. 1–14, Apr. 2021, doi: 10.1016/j.jnucmat.2021.152901i.
- [112] M. Balat-Pichelin, M. Passarelli, and A. Vesel, “Recombination of atomic oxygen on sintered zirconia at high temperature in non-equilibrium air plasma,” *Mater Chem Phys*, vol. 123, no. 1, pp. 40–46, Sep. 2010, doi: 10.1016/j.matchemphys.2010.03.059.
- [113] M. Balat-Pichelin, J. Iacono, and P. Boubert, “Recombination coefficient of atomic oxygen on ceramic materials in a CO₂ plasma flow for the simulation of a Martian entry,” *Ceram Int*, vol. 42, no. 2, pp. 2761–2769, Feb. 2016, doi: 10.1016/j.ceramint.2015.11.007.
- [114] L. Bedra, M. Rutigliano, M. Balat-Pichelin, and M. Cacciatore, “Atomic oxygen recombination on quartz at high temperature: Experiments and molecular dynamics simulation,” *Langmuir*, vol. 22, no. 17, pp. 7208–7216, Aug. 2006, doi: 10.1021/la060032l.
- [115] D. Mariotti and R. M. Sankaran, “Microplasmas for nanomaterials synthesis,” *J Phys D Appl Phys*, vol. 43, no. 32, 2010, doi: 10.1088/0022-3727/43/32/323001.
- [116] T. L. Koh, E. C. O’Hara, and M. J. Gordon, “Microplasma-based synthesis of vertically aligned metal oxide nanostructures,” *Nanotechnology*, vol. 23, no. 42, 2012, doi: 10.1088/0957-4484/23/42/425603.
- [117] A. C. Pebley, A. Peek, T. M. Pollock, and M. J. Gordon, “Microplasma-based growth of biphasic NiFe₂O₄/NiO nanogranular films for exchange bias applications,” *Chemistry of Materials*, vol. 26, no. 20, pp. 6026–6032, 2014, doi: 10.1021/cm502929m.
- [118] T. L. Koh, E. C. O’Hara, and M. J. Gordon, “Growth of nanostructured CuO thin films via microplasma-assisted, reactive chemical vapor deposition at high pressures,” *J Cryst Growth*, vol. 363, pp. 69–75, 2013, doi: 10.1016/j.jcrysgro.2012.10.005.
- [119] J. Benedikt, K. Focke, A. Yanguas-Gil, and A. Von Keudell, “Atmospheric pressure microplasma jet as a depositing tool,” *Appl Phys Lett*, vol. 89, no. 25, pp. 2004–2007, 2006, doi: 10.1063/1.2423233.
- [120] T. L. Koh and M. J. Gordon, “Spray deposition of nanostructured metal films using hydrodynamically stabilized, high pressure microplasmas,” *Journal of Vacuum Science & Technology A: Vacuum, Surfaces, and Films*, vol. 31, no. 6, p. 061312, 2013, doi: 10.1116/1.4825129.
- [121] V. Raballand, J. Benedikt, S. Hoffmann, M. Zimmermann, and A. Von Keudell, “Deposition of silicon dioxide films using an atmospheric pressure microplasma jet,” *J Appl Phys*, vol. 105, no. 8, 2009, doi: 10.1063/1.3108541.

- [122] T. L. Koh and M. J. Gordon, "Thin-film deposition with high pressure capillary micro-discharges under different supersonic flow and shock regimes," *J Phys D Appl Phys*, vol. 46, no. 49, 2013, doi: 10.1088/0022-3727/46/49/495204.
- [123] D. M. Buczala, A. L. Brunsvold, and T. K. Minton, "Erosion of Kapton® H by hyperthermal atomic oxygen," *J Spacecr Rockets*, vol. 43, no. 2, pp. 421–425, 2006, doi: 10.2514/1.16402.
- [124] D. Paul, M. Mozetic, R. Zaplotnik, G. Primc, D. Đonlagić, and A. Vesel, "A Review of Recombination Coefficients of Neutral Oxygen Atoms for Various Materials," Mar. 01, 2023, *MDPI*. doi: 10.3390/ma16051774.
- [125] A. Viviani and G. Pezzella, *Aerodynamic and Aerothermodynamic Analysis of Space Mission Vehicles*. 2015. doi: 10.1007/978-3-319-13927-2.
- [126] K. Niemi, V. Schulz-Von Der Gathen, and H. F. Döbele, "Absolute atomic oxygen density measurements by two-photon absorption laser-induced fluorescence spectroscopy in an RF-excited atmospheric pressure plasma jet," *Plasma Sources Sci Technol*, vol. 14, no. 2, pp. 375–386, May 2005, doi: 10.1088/0963-0252/14/2/021.
- [127] F. Monteverde and R. Savino, "Stability of ultra-high-temperature ZrB₂-SiC ceramics under simulated atmospheric re-entry conditions," *J Eur Ceram Soc*, vol. 27, pp. 4797–4805, 2007.
- [128] J. Marschall *et al.*, "Oxidation of ZrB₂-SiC Ultrahigh-Temperature Ceramic Composites in Dissociated Air," *J Thermophys Heat Trans*, vol. 23, no. 2, pp. 267–278, 2009, doi: 10.2514/1.39974.
- [129] N. Li, P. Hu, X. Zhang, Y. Liu, and W. Han, "Effects of oxygen partial pressure and atomic oxygen on the microstructure of oxide scale of ZrB₂-SiC composites at 1500°C," *Corros Sci*, vol. 73, pp. 44–53, Aug. 2013, doi: 10.1016/j.corsci.2013.03.023.
- [130] J. Marschall, D. A. Pejaković, W. G. Fahrenholtz, G. E. Hilmas, F. Panerai, and O. Chazot, "Temperature jump phenomenon during plasmatron testing of ZrB₂-SiC ultrahigh-temperature ceramics," *J Thermophys Heat Trans*, vol. 26, no. 4, pp. 559–572, 2012, doi: 10.2514/1.T3798.
- [131] P. Kolodziej and D. A. Stewart, "Nitrogen recombination on high-temperature reusable surface insulation and the analysis of its effect on surface catalysis," in *AIAA 22nd Thermophysics Conference, 1987*, American Institute of Aeronautics and Astronautics Inc, AIAA, 1987. doi: 10.2514/6.1987-1637.
- [132] D. E. Rosner, H. M. Chung, and H. H. Feng, "Resistance Relaxation Studies of Gas/Metal Reactions Leading to Simultaneous Dissolution and Gasification. The Dissociated Oxygen/Tantalum System Above 2000 K Part 1.-Methodology and the Role of Atomic Oxygen," *J Chem Soc*, pp. 842–857, 1974.
- [133] A. G. Gusakov, S. A. Raspopov, A. A. Vecher, and A. G. Voropayev, "Interactions of tantalum with diatomic and atomic oxygen at low pressures," *J Alloys Compd*, vol. 201, pp. 67–72, Mar. 1993.
- [134] S. A. Raspopov *et al.*, "Kinetics of zirconium oxidation by atomic and molecular oxygen at low pressures," *J. Chem. Soc., Faraday Trans*, vol. 93, no. 11, pp. 2113–2116, 1997.
- [135] G. Liu, L. Cheng, K. Li, Z. Chen, G. Yao, and X. Luan, "Atomic oxygen damage behavior of TaC coating-modified C/C composite," *J Eur Ceram Soc*, vol. 40, no. 3, pp. 642–650, Mar. 2020, doi: 10.1016/j.jeurceramsoc.2019.10.025.

- [136] G. Liu, L. Change, K. Li, Z. Chen, X. Xiong, and X. Luan, "Damage behavior of atomic oxygen on zirconium carbide coating modified carbon/carbon composite," *Ceram Int*, vol. 45, pp. 3324–3331, Oct. 2020.
- [137] X. Luan, G. Liu, M. Tian, Z. Chen, and L. Cheng, "Damage behavior of atomic oxygen on a hafnium carbide-modified C/SiC composite," *Composites Part B*, vol. 2019, Apr. 2021.
- [138] J. Belle and M. W. Mallett, "Kinetics of the High Temperature Oxidation of Zirconium," *J. Electrochem. Soc.*, vol. 101, pp. 339–342, Jul. 1954.
- [139] E. A. Gulbransen and K. F. Andrew, "Oxidation of zirconium between 400° and 800°C," *JOM*, vol. 9, no. 4, pp. 394–400, 1957, doi: 10.1007/bf03397885.
- [140] F. N. Rhines and R. G. Connell Jr., "Role of Grain Growth in the Oxidation of Nickel," *J. Electrochem. Soc.*, vol. 121, pp. 1122–1128, Jul. 1977.
- [141] G. P. Sabol and S. B. Dalgaard, "The Origin of the Cubic Rate Law in Zirconium Alloy Oxidation," *J. Electrochem. Soc.*, vol. 122, pp. 316–317, Feb. 1975.
- [142] H. E. Evans, D. J. Norfolk, and T. Swan, "Perturbation of Parabolic Kinetics Resulting from the Accumulation of Stress in Protective Oxide Layers," *J. Electrochem. Soc.*, vol. 128, no. 7, pp. 1180–1185, Jul. 1978.
- [143] P. Kofstad, *Nonstoichiometry, Diffusion, and Electrical Conductivity In Binary Metal Oxides*. 1972.
- [144] B. Oberländer, P. Kofstad, and I. Kvernes, "On Oxygen Diffusion in tetragonal zirconia," *Materwiss Werksttech*, vol. 19, no. 6, pp. 190–193, 1988, doi: 10.1002/mawe.19880190604.
- [145] P. Kofstad and D. J. Ruzicka, "On the Defect Structure of ZrO₂ and HfO₂," *J Electrochem Soc*, 1963.
- [146] R. Chosson, A. F. Gourgues-Lorenzon, V. Vandenberghe, J. C. Brachet, and J. Crépin, "Creep flow and fracture behavior of the oxygen-enriched alpha phase in zirconium alloys," *Scr Mater*, vol. 117, pp. 20–23, May 2016, doi: 10.1016/j.scriptamat.2016.02.021.
- [147] Z. Hózer, C. Gyori, L. Matus, and M. Horváth, "Ductile-to-brittle transition of oxidised Zircaloy-4 and E110 claddings," *Journal of Nuclear Materials*, vol. 373, no. 1–3, pp. 415–423, Feb. 2008, doi: 10.1016/j.jnucmat.2007.07.002.
- [148] T. Furuta, S. Kawasaki, M. Hashimoto, and T. Otomo, "Oxygen embrittlement for zircaloy cladding," *J Nucl Sci Technol*, vol. 15, no. 2, pp. 152–155, 1978, doi: 10.1080/18811248.1978.9735503.
- [149] J. Stringer, "The Oxidation of Titanium in Oxygen at High Temperatures," *Acta. Met.*, vol. 8, pp. 758–766, 1960.